

SHEWANELLA ONEIDENSIS MR-1 AS AN AVENUE FOR GREEN NANOPARTICLE BIOSYNTHESIS AND NEXT-GENERATION BIOSENSING

Dylan Rees

Submitted in Partial Fulfillment of the Requirements
for the Degree of

DOCTOR OF PHILOSOPHY

Approved by:

Dr. Shayla Sawyer, Chair
Dr. Yuri Gorby
Dr. Partha Dutta
Dr. Agung Julius



Department of Electrical and Computer Systems Engineering
Rensselaer Polytechnic Institute
Troy, New York

[May 2019]
Submitted April 2019

CONTENTS

LIST OF TABLES.....	v
LIST OF FIGURES	vi
ACKNOWLEDGEMENT.....	ix
ABSTRACT.....	xii
1. INTRODUCTION	1
1.1 Background	1
1.1.1 Reduction-Oxidation Chemistry.....	1
1.1.2 Microbiology and the Electron Transport Chain.....	3
1.1.3 Bacterial Nanowires	4
1.1.4 Bacterial Production of Nanomaterials	6
1.1.5 The Physics and Chemistry of Nanomaterials	11
1.1.6 Bacterial Biofilms and their Environmental Interactions	15
1.2 Motivation	17
1.2.1 Advantages of Bacterial Nanoparticle Synthesis	17
1.2.2 Bioremediation	18
1.2.3 Electrochemically and Photonically Active Living Sensors.....	19
1.3 Methods	21
1.3.1 Cultivation and Incubation	21
1.3.2 Scanning Electron Microscopy	21
1.3.3 Energy-dispersive X-ray Spectroscopy.....	22
1.3.4 Transmission Electron Microscopy.....	24
1.3.5 X-ray Powder Diffraction	25
1.3.6 Cyclic Voltammetry	26
1.3.7 UV-Vis Absorption Spectroscopy	28
1.3.8 Raman Spectroscopy	29
1.4 Thesis Organization.....	32
2. LEAD SULFIDE BIOSYNTHESIS	33
2.1 Introduction.....	33
2.2 Incubation.....	35
2.3 Characterization	37

2.3.1 Scanning Electron Microscopy / X-ray Energy Dispersive Spectrometry	37
2.3.2 X-ray Diffraction	40
2.4 Conclusions.....	42
3. CADMIUM SULFIDE BIOSYNTHESIS.....	43
3.1 Introduction.....	43
3.2 Experiment 1: Controlled Thiosulfate Concentration	44
3.2.1 Incubation	44
3.2.2 Characterization Using SEM/EDS	45
3.2.3 Characterization Using XRD	47
3.2.4 Characterization Using Absorption Spectroscopy.....	49
3.3 Experiment 2: Controlled Inoculation Methods.....	51
3.3.1 Incubation	51
3.3.2 Characterization Using SEM/EDS	52
3.4 Conclusions.....	58
4. MOLYBDENUM DISULFIDE BIOSYNTHESIS.....	60
4.1 Introduction.....	60
4.2 Experiment 1: Controlled Thiosulfate Concentration	62
4.2.1 Incubation	62
4.2.2 Characterization Using SEM/EDS	63
4.2.3 Characterization Using TEM	65
4.2.4 Characterization Using Absorption Spectroscopy.....	68
4.2.5 Characterization Using XRD	70
4.2.6 Characterization Using Raman Spectroscopy	73
4.3 Experiment 2: Controlled Molybdenum Concentration	75
4.3.1 Incubation	75
4.3.2 Characterization Using Absorption Spectroscopy.....	76
4.4 Conclusions.....	78
5. SURFACES AND ELECTROCHEMISTRY	80
5.1 Characterization of <i>Shewanella</i> Interactions with Surfaces.....	80
5.1.1 Silicon	80
5.1.2 Reduced Graphene Oxide.....	82
5.1.3 Microporous Alumina	85
5.2 Electrochemical Characterization of Aqueous <i>Shewanella</i> Systems.....	90

5.2.1 Measurement of Current During Cultivation.....	90
5.2.2 Three-Electrode Zinc System with Two Jars	91
5.2.3 Three-Electrode Zinc System with Three Jars.....	94
5.3 Conclusions.....	99
6. CONCLUSIONS AND FUTURE WORK.....	100
6.1 Summary.....	100
6.2 Lessons and Future Work.....	103
REFERENCES	106
APPENDIX.....	116
A.1 Standard Medium for Cultivation of <i>S. oneidensis</i> MR-1.....	116
A.2 Mineral Solution, 100x stock.....	117
A.3 Vitamin Solution, 100x stock	118
A.4 Amino Acid Solution, 100x stock	118

LIST OF TABLES

Table 1: A Comparison of biological and non-biological nanoparticle synthesis.	18
Table 2: Bottle groups for varied thiosulfate PbS synthesis experiment.	35
Table 3: Bottle groups for controlled thiosulfate cadmium sulfide synthesis experiment.	44
Table 4: Bottle groups for varied inoculum CdS synthesis experiment.	51
Table 5: Bottle groups for the controlled thiosulfate MoS ₂ synthesis experiment.	62
Table 6: Bottle groups for the controlled molybdenum MoS ₂ synthesis experiment.	75
Table 7: Limitations in current work and lessons for future work.	103

LIST OF FIGURES

Figure 1: A multi-input biosensor containing DMRB.	20
Figure 2: Gamry Reference 3000 potentiostat with attached electrode leads.	27
Figure 3: Development of PbS precipitates (top) and settling (bottom).	36
Figure 4: Precipitates in the inoculated 20mM thiosulfate batch.	38
Figure 5: EDS area analysis of biofilm structure.	39
Figure 6: Precipitates in the sterile 20mM thiosulfate batch.	40
Figure 7: XRD diffractogram for the PbS nanoparticles generated.	41
Figure 8: Development of CdS precipitate (top) and settling (bottom).	45
Figure 9: A Shewanella bacterium surrounded by nanomaterials.	46
Figure 10: A Shewanella bacterium surrounded by nanomaterials.	47
Figure 11: XRD diffractogram indicating CdS diffraction planes and NaCl peaks.	48
Figure 12: Comparative absorption spectroscopy for CdS samples.	49
Figure 13: Development of yellow color in inoculated cadmium bottles.	52
Figure 14: SEM micrograph of the precipitate-containing Group A batch.	53
Figure 15: Group A batch without yellow precipitate.	53
Figure 16: SEM micrograph depicting nanomaterials in the Group C batch.	54
Figure 17: Low-magnification image of cadmium-oxygen-carbon microstructures.	55
Figure 18: Closeup of several cadmium-oxygen-carbon microstructures.	55
Figure 19: Broken Cd-O-C microstructure with bacterial biofilm inside.	56
Figure 20: Partially intact Cd-O-C microstructure with biofilm growing on the interior.	57
Figure 21: Partially intact Cd-O-C microstructure with bacteria growing on the exterior.	57
Figure 22: The development of orange color in the inoculated bottles.	63
Figure 23: Biofilm development in Group B.	63

Figure 24: Biofilm development in Group B.....	64
Figure 25: Site of EDS point analysis, showing biofilm growth.	64
Figure 26: SEM micrograph of the Group D batch reveals organic deposits.....	65
Figure 27: Nanoparticles in the Group B molybdenum sample.....	66
Figure 28: Presumed organic material (left) and its diffraction pattern (right).....	67
Figure 29: A polycrystal (left) and its diffraction pattern (right).....	67
Figure 30: A single crystal (left) and its diffraction pattern (right).	68
Figure 31: Absorbance peaks for the molybdenum batches.	69
Figure 32: Comparative XRD diffractogram of molybdenum samples.	70
Figure 33: Comparison of the diffractogram peaks from 10-15°.	72
Figure 34: Comparison of the diffractogram peaks from 30-35°.	73
Figure 35: Raman spectrograph of the black biofilm harvested from the Group B batch.	74
Figure 36: The development of blue color in the inoculated bottles.	75
Figure 37: Absorbance spectroscopy for various molybdenum batches.	76
Figure 38: Shewanella nanowire formation in the presence of cadmium.	81
Figure 39: Shewanella nanowire formation in the presence of molybdenum.	82
Figure 40: SEM micrograph of reduced graphene oxide. [113].....	83
Figure 41: Shewanella growing in the micropores of reduced graphene oxide.	84
Figure 42: A cluster of Shewanella bacteria growing on reduced graphene oxide.	84
Figure 43: Bare microporous alumina, with a bacterium for scale (center).	86
Figure 44: Surface of SmartPor working electrode after crystal growth.	87
Figure 45: Shewanella growing on microporous alumina.	88
Figure 46: Point EDS analysis of surface nanocrystals.	89
Figure 47: Current fluctuation during Shewanella incubation.....	91
Figure 48: Visual difference between inoculated (right) and sterile (left) jar batches.	92
Figure 49: Cyclic voltammetry scan of the jars at 10mV/sec.....	93

Figure 50: Cyclic voltammetry scan of the jars at 50mV/sec.....	94
Figure 51: Incubation jars for the Shewanella three-jar incubation experiment.....	95
Figure 52: Comparison of the CV curves of the three jars at 50mV/sec scan rate.	96
Figure 53: Cyclic voltammetry graph of the 10mM thiosulfate sterile jar.	96
Figure 54: Cyclic voltammetry graph of the 10 mM thiosulfate inoculated jar.....	97
Figure 55: Longitudinal study of the 10mM thiosulfate inoculated jar at 50mV/s scan.	98

ACKNOWLEDGEMENT

For me, the completion of a PhD at RPI has been a highly nonlinear journey. After entering my program I worked on several different research projects in my field before discovering the work that became my dissertation project. Due to its interdisciplinary nature, embarking on this project entailed a leap of faith on my part as well as, I believe, the part of my advisors. However, I believe that all of us saw the promise of the project, and the excitement that came with executing it sustained me through the most difficult parts of research. I owe a debt of gratitude to a large number of mentors, supporters and collaborators that helped me move the project forward.

I want to first thank my advisor in the Department of Environmental Engineering, Prof. Yuri Gorby, whose remarkable body of research was the catalyst for, and has been the driving force behind, this research. Yuri has not only taught me how to do microbiological work but also influenced me with his remarkably creative and ethically-driven approach to research. It has been an honor to stand on the shoulders of one of the giants of electromicrobiology. In addition, I benefited from some excellent equipment assistance and technical insights from some of Yuri's graduate students, in particular Lucas Lis, John Hayes, and Catalina Alvarado.

I also want to thank my advisor in the Department of Electrical, Computer and Systems Engineering, Prof. Shayla Sawyer, for her superb guidance in this project. Prof. Sawyer has been not only an outstanding technical advisor in the research but also a source of mentorship and inspiration in all aspects of my career development. Her approach to leading a research group has made the research experience both rewarding and fun for me, helping me to preserve the passion for research that lead me into this field. I also want to thank several of Prof. Sawyer's current and former graduate students for their technical assistance and support; in particular Prachi Sharma, Amelia Peterson, Lauren Brady, and James Davis.

I am grateful to the other two members of my doctoral committee, Prof. Partha Dutta and Prof. Agung Julius, for their role in reviewing and giving feedback on this dissertation, as well as

excellent feedback during my doctoral candidacy that positively impacted the end product of the research. Several other professors and administrators in my department also merit mentioning due to their strong support and helpful advice as I pursued my degree; in particular Priscilla Magilligan, Ronnie Rowe, Gary Saulnier, and Ken Connor.

Due to the multidisciplinary nature of this project, I relied on the support and guidance of researchers and technicians in a number of departments and centers on campus. In the Department of Materials Science, these include Ray Dove, Rob Planty, Dustin Anderson, Brent Engler, Prof. Robert Hull, Genevieve Kane, and Anne Hynes. In the departments of Biological Sciences and Earth and Environmental Sciences, they include Prof. Rick Relyea, Prof. Karyn Rogers, and Gina Oliver. In the Department of Physics: Prof. Kim Lewis and Mike Giordano. In the Department of Mechanical, Nuclear and Aerospace Engineering: Prof. Nikhil Koratkar and Tushar Gupta. Finally, in the Center for Biotechnology and Interdisciplinary Studies and the Microfabrication Clean Room: David Frey, Bryant Colwill, and Sergey Pryshchep.

I want to thank the RPI Department of Humanities, Arts and Social Sciences, and in particular the Department of Science and Technology Studies, for its contributions to my academic experience. Members of this department provided me with opportunities for funded teaching and research at during a period in which finding funding for my work was a challenge. In addition, conversations I had and literature was exposed to via my contact with this department helped me situate my research in a broader social context and consider how to be the most socially responsible engineer I could possibly be. I would in particular like to thank Prof. Nancy Campbell, Prof. Atsushi Akera, Prof. Ron Eglash, Brian Callahan, Brandon Costelloe-Kuehn, and Prof. Kathy High.

I want to express love and gratitude to my Mom, Dad, Grandma Rees and Grandma Clark, who nurtured my interest science at an early age and were unwavering in their love and support through this process, and without whom I could not have completed a PhD. My Grandmas were

unable to live to see me complete my degree, but I feel their presence in spirit as I complete my program.

Finally I want to express my gratitude for the friends who provided me with moral support and helped me find community in the city of Troy and the greater Capital District - friends too numerous to list here. In addition to relying on my local community, I relied on other dear friends from afar - friends in places like Seattle, Ithaca, Cleveland, Pittsburgh, Vancouver, and Boston. Those friends will know who they are, and if they haven't received my thanks in person, I intend that they will.

ABSTRACT

As global resource consumption grows and the pressures of industrialization and climate change place stress on Earth's natural sources of freshwater, the preservation of these water systems has become a matter of increasing urgency. Accomplishing this task will require many strategies and technologies, such as engineering non-polluting renewable energy systems, remediation techniques for polluted bodies of water, and most recently, arrays of smart sensors, which can collect detailed data of lake dynamics and these complex systems to be modeled.

As microbiologists and engineers have recently discovered, organisms living in or near these water systems may help provide a solution to these engineering problems. A class of bacteria known as dissimilatory metal-reducing bacteria, or DMRB, have adapted to metal-rich waters by reducing ions of metals such as manganese, arsenic, and iron as part of their metabolic processes. In the process, DMRB often trigger the precipitation of various insoluble or minimally-soluble minerals consisting of reduced metals. DMRB can adapt well to healthy freshwater environments as well as contaminated or extreme environments such as hydrothermal vents or acid mine drainage sites.

In this work I describe the cultivation of a dissimilatory metal-reducing bacterium, *Shewanella oneidensis* MR-1, in controlled environments, demonstrating novel methods of synthesis for several types of metal sulfide nanoparticles with semiconductor properties and applications in semiconductor device and sensor engineering. *Shewanella* is an obligate anaerobe that can grow either aerobically or anaerobically but performs metal or sulfur reduction in anaerobic environments.

Three types of semiconductor nanoparticles - lead sulfide, cadmium sulfide and molybdenum disulfide - were synthesized in the first known controlled studies using the metal and sulfur-reducing capabilities of *Shewanella oneidensis* MR-1 to produce these materials. Batches of *Shewanella* were cultivated anaerobically with sodium thiosulfate

supplied as an electron acceptor. Metal ions were added to the media through the addition of dissolved salts, and the batches were incubated for several days. In all trials, precipitates formed in inoculated batches that did not exist in sterile batches of the same liquid medium. Scanning electron microscopy and energy dispersive X-ray spectroscopy revealed substantial biofilm growth that was associated with concentrated levels of metals from the supplied metal salts along with sulfur, suggesting the formation of metal sulfides at the biofilm sites. Using a combination of X-ray diffraction and Raman spectroscopy, we were then able to confirm the presence of the targeted nanoparticulate materials.

In addition to performing controlled nanoparticle synthesis with *Shewanella*, I investigated the interactions of the bacteria with a range of solid substrates in an aqueous growth medium. I was able to successfully observe the interactions of *Shewanella* biofilms with substrates of silicon, microporous alumina, and reduced graphene oxide. Furthermore, I performed cyclic voltammetry on a three-electrode system containing *Shewanella* culture, a steel working electrode, a titanium counter electrode and a Gamry Ag/AgCl reference electrode. The cyclic voltammetric measurements revealed reduction-oxidation activity that corresponded to visible changes in the culture, such as the evolution of a biofilm coating and the corrosion of iron.

The results of this work offer new insights into the potential for biologically-assisted creation of electronic devices. Semiconductor nanoparticles have a wide range of industry applications ranging from photonic sensors to transistors to photovoltaic arrays. Compared to existing chemical methods, biological synthesis of semiconductor nanoparticles requires substantially less heat input as well as no added chemical surfactants or stabilizers. Meanwhile, my studies of electron transfer between bacterial biofilms and solid electrodes contribute to existing knowledge of electro-biochemical sensing, which may offer substantial cost advantages over existing aqueous chemical sensors by allowing direct sensing of microbial metabolic activity and its by-products.

1. INTRODUCTION

1.1 Background

1.1.1 Reduction-Oxidation Chemistry

When a piece of metal is immersed in an electrolyte, a series of electrochemical interactions occur. First, the metal will release some of its atoms into the water as charged ions. Second, some of the dissolved ions from the electrolyte will deposit themselves onto the solid metal. The equilibrium position for this reaction will vary greatly depending on which metals and which electrolytes are present. If reactivity of the metal with the water is greater than that of the electrolyte ions with the metal, the release of positively-charged metal ions into the water will dominate the reaction, causing the water to develop a positive charge and the metal a negative charge. If the electrolyte reactivity is higher than the metal reactivity, the opposite will occur: the water will develop a negative charge while the metal develops a positive charge. In electrochemistry terms, we may refer to the resulting system as a half-cell [1].

If two different half-cell systems come into electrical contact with one another, the differing equilibria of the two systems will lead to a so-called liquid junction potential between them. This can be understood in analogy with the p-n junctions of semiconductor devices: in the same manner in which an electronic potential develops between two metals of different Fermi levels, an electrochemical potential develops between two electrochemical systems of different diffusions.

The reaction that governs such an electrochemical cell such is known more broadly by another name: the reduction-oxidation reaction or redox reaction. In a redox reaction, one or more electrons transfer from one species to another, or, in chemical terms, one species experiences

an increase in its oxidation state while another experiences a corresponding decrease. Common oxidation reactions include the formation of iron oxide from elemental iron in the presence of air:



In the reaction above, free iron goes from an oxidation state of 0 to an oxidation state of +3 and can therefore be said to have been oxidized. Meanwhile, the oxygen goes from a state of 0 in its gaseous form to -2 in the product, and can be said to have been reduced.

Fundamentally, electrochemical cells convert electrical energy to chemical energy, and vice versa. This idea can be operationalized using a formula called the Nernst equation. Consider a given chemical equation:



We then define a reaction quotient that corresponds to the reaction proceeding from one side of the chemical equation to the other. Below we show a reaction quotient for the rightward reaction (with products on top and reactants on the bottom):

$$Q_r = \frac{\{C^\gamma\}\{D^\delta\}}{\{A^\alpha\}\{B^\beta\}} \quad (3)$$

Each term enclosed in brackets represents the activity coefficient for that reactant or product. The Nernst equation is then as follows:

$$E = E_0 - \frac{RT}{nF} \ln Q_r \quad (4)$$

In the equation above, E is the electrical potential of the cell, E_0 is the standard half-cell reduction potential, Q_r is the reaction quotient as defined above, R is the universal gas constant, T is the temperature in Kelvin, n is the number of moles of electrons transferred in the given redox

reaction, and F is the Faraday constant. Armed with the Nernst equation, we can calculate the electric potential for a given cell [1].

Above all it is important to understand that via electrochemistry, chemical reactions and electricity are fundamentally coupled with one another. This means that chemical reactions can influence the development of current and voltage and that the inverse is also true [1]. As discussed in the following sections, this fact is a fundamental tenet of biology, and because of it, electricity provides us with both a means of sensing microbiological activity and a means of influencing it.

1.1.2 Microbiology and the Electron Transport Chain

Biology, at its core, is a phenomenon of structured electrochemistry in which chemical energy flows through a cell via a series of reduction-oxidation reactions. First, a cell derives electrons via the oxidation of molecules called electron donors. Next, these electrons transfer to another site in the cell via a reduction-oxidation reaction, which in turn triggers other reduction-oxidation reactions in a cascading process. In the final step, the cell loses electrons by reducing molecules called electron acceptors. Together, the reduction-oxidation steps that occur within the cell during its respiration are referred to as the electron transport chain.

This electron transport chain allows cells to extract chemical energy from nutrients in their environment in order to power their metabolic processes. Within living cells, we see electrochemical gradients that, in their fundamental principles, mimic those of lab-created chemical batteries. Rather than using electrodes and containers of electrolyte, living cells achieve an electrochemical potential across their cell membrane through transporting electrons through a chain of enzymes or proteins while also concentrating H^+ ions on one side of the cell via either diffusion or active transport. Rather than providing power to an electrical circuit, the cell provides power for the synthesis of adenosine triphosphate (ATP), the “energy shuttle” molecule common to all cells. ATP travels throughout the cell to the enzymes and proteins that carry out the cell’s metabolic processes, where it releases chemical energy by breaking into adenosine diphosphate

(ADP) and a phosphate group. This process is virtually the same in any cell whether the electrons in the transport chain originate from photosynthesis, fermentation, or some other source [2]. For instance, fermentation reactions, which break sugar down into alcohols and gases, commonly use organic molecules as both electron donors and electron acceptors.

Cells achieve electron transport via several types of carrier molecules that utilize redox reactions in order to shuttle electrons from one place to another. One of the more notable structures with this capability is the cytochrome. Cytochromes are proteins that contain a heme (iron) group that acts as a redox site. Since iron commonly exists in both the Fe^{2+} and Fe^{3+} oxidation states, a cytochrome can utilize this transition between states in order to pick up, and then offload, an electron in the cell. Structurally, cytochromes often form chains, passing electrons from one redox site to another. However, their specific deployment within a cell will vary, and a large number of different cytochromes, with many different structures, exist across the domains of life [3].

1.1.3 Bacterial Nanowires

A particularly remarkable extracellular structure within biofilms, of increasing interest to scientists and engineers, is the so-called bacterial nanowire. Certain bacteria have been observed extruding wire-like extensions from their outer cell membranes that make contact with nearby materials and assist with the transfer of electrons to these materials, as well as the intercellular transfer of electrons [4]. Bacterial nanowires contain chains of specialized cytochrome proteins, called multiheme c-type cytochromes, that span the nanowires' length and facilitate electron transfer between the organelles of the bacteria and the electron acceptors in their environment. They appear to be remarkably efficient in their ability to target specific electron acceptor materials and network them electrochemically to larger biofilm structures with minimal electron loss. [5]

The internal mechanics of bacterial nanowires are not yet fully understood. Some scientists have attempted measurements of the nanowires' conductivity. Leung et al. showed that

nanowires of *Shewanella oneidensis* MR-1 exhibited ohmic current-voltage behavior when sandwiched between a gold substrate (work function ~5.4eV) and a platinum AFM tip (work function ~5.6eV) but exhibited nonlinear behavior on an HOPG substrate (work function ~4.6eV). The current-voltage measurements suggested that the nanowires formed a defined energy barrier at the nanowire-HOPG interface and also that they were effectively behaving as p-type semiconductors with a hole mobility of 10^{-1} cm²/(Vs), comparable to some well-known organic semiconductors [6][7]. Other species of bacteria also appear to produce nanowires; they have been directly observed in *Geobacter sulfurreducens* and genes coding for the requisite multiheme c-type cytochromes have been found in multiple species of metal-reducing bacteria, such as *Thermincola ferriacetica*, *Desulfuromonas soudanensis* and *Geothrix fermentans*, among others [6], [8].

Attempts to understand the fundamental biophysics of nanowires began with the assumption that their dynamics were not unlike organic semiconductor materials already in use, with stacked π -orbitals that facilitated coherent electron tunneling along molecular chains. [8] However, this model proved to be flawed [6]. The band conduction model specifies a minimum carrier mobility defined by the following equation (where e is the fundamental charge and r is the distance between electron tunneling sites):

$$\mu >> er^2/2\hbar \quad (5)$$

An examination of the distance between heme group sites in *Shewanella oneidensis* MR-1 nanowires, combined with the carrier mobility measurement described above, suggested that *Shewanella* nanowires do not meet the mobility requirements for coherent electron tunneling. Instead, the current theory of nanowire conduction revolves around kinetic electron hopping between heme sites in the nanowire; in other words, their conduction appears to be dominated by a form of hot-carrier injection [6], [9].

A growing body of evidence points to another remarkable property of bacterial nanowires. It appears that, much like an electric circuit, bacterial nanowires will move electrons to and from

a material with relative agnosticism to the identity of that material, provided that the relevant electrochemical and electronic barriers are overcome. *Shewanella oneidensis* MR-1 has been observed reducing a wide range of metal ions, and researchers have been able to move beyond purely chemical interactions and observe *Shewanella* biofilms transferring electrons directly to solid electrodes under a potential difference, allowing the creation of an interface between the bacteria and an external electric circuit. This phenomenon has already been utilized in order to create microbial fuel cells that generate electricity from microbial metabolic processes, although such systems remain relatively impractical for industrial use due to low current levels [10], [11]. Furthermore, some recent evidence suggests that the connection that a bacterial biofilm forms with an electrode via nanowires may support current flow in either direction. This would mean that when a biofilm-laden electrode is supplied with an appropriate positive potential, current can flow from an external electrical system into the bacteria in order to power their cell processes [12]. It is clear that the potential to create such systems could offer wide-ranging possibilities for the control of living microbial communities.

In summary, it appears that the primary purpose of bacterial nanowires is to allow the bacteria that produce them to connect to and access electron acceptor materials in order to complete their cellular metabolism. Through the process of dissimilatory metal reduction, these bacteria often fundamentally transform their immediate environment, sometimes forming new minerals in the process. This process will be described in more detail in the next section.

1.1.4 Bacterial Production of Nanomaterials

The process by which bacteria (and other organisms) produce nanomaterials is called biomineralization. It is not a single process but instead a term that describes many different biochemical processes, and it can be observed across vast domains of life and at many different scales. At larger scales, it is responsible for the formation of structures such as bones, shells, and teeth in animals. At smaller scales it can form micro- and nanoscale crystals inside, on the surface

of, or in the vicinity of single-celled organisms [13]. This work will focus on biomineralization as it occurs in bacteria.

1.1.4.1 Mechanisms of Production

There are several mechanisms by which bacteria can cause mineralization to occur. First, bacteria can cause chemical reactions whose by-products, independent of the bacteria themselves, cause further reactions in the environment. A well-studied example of this phenomenon is that of sulfate-reducing bacteria in sewer systems. These bacteria produce significant quantities of hydrogen sulfide gas as part of their metabolism. The gas can then react with iron to form an iron sulfide precipitate anywhere in the system where both iron and hydrogen sulfide gas is present [14], [15].

There are also many situations in which the bacteria themselves interact directly with materials in their environment to produce biominerals. This includes several cases in which bacteria appear to respond to high concentrations of toxic heavy metal ions by forming minerals with those ions, thereby removing them from solution. Jalali and Baldwin demonstrated that a mixed culture of sulfur-reducing bacteria will produce greater amounts of extracellular polymeric substance (EPS) in the presence of higher copper concentrations, and that the secreted EPS becomes associated with the formation of copper sulfide nanoparticles. The study concluded that the bacteria were using proteins in their EPS to strategically accumulate copper and selectively catalyze the precipitation reaction already favored due to the presence of hydrogen sulfide, also produced by the same bacteria [16]. Other researchers, also working with sulfate-reducing bacteria have observed certain species performing similar tasks with a range of other heavy metals [17]. The phenomenon has also been observed in bacteria that do not reduce sulfate such as *Pseudomonas stutzeri*, which can produce silver nanoparticles using a similar mechanism [18].

Although the above examples of biomineralization involve the generation of nanoparticles on the surface of bacteria and the surface of their secretions, other bacteria produce minerals

intracellularly. Magnetotactic bacteria, for instance, form intracellular magnetite particles as part of a strategy to align themselves with, and navigate via, magnetic field lines [19]. In *E. coli*, incubation with cadmium chloride and sodium sulfide has been shown to lead to the formation of intracellular CdS nanoparticles [20]. In other bacteria, this intracellular bioaccumulation and biominerization effect can include metal reduction, as in the case of *Rhodobacter capsulatus* which produces gold nanoparticles from gold salts [21].

Bacteria that perform dissimilatory metal reduction generally also catalyze the production of biominerals, but this process is distinct in several ways from the other processes described above. Unlike bacteria that biominerize as a defensive mechanism or passively through hydrogen sulfide production, DMRB actively benefit from the presence of certain heavy metal ions and have evolved strategies to make contact with such ions. This means that the addition of these materials facilitates additional cell growth, and increased biomineral production capacity, rather than interfering with it [22].

Unlike species that reduce or precipitate minerals intracellularly, DMRB do so on the exterior of the cell wall and their bacterial nanowires, allowing the generated nanomaterials to be recovered without rupturing cell walls [23]. Furthermore, dissimilatory metal reduction offers several advantages over the non-reductive precipitation process observed in other species. Unlike non-reducing species, DMRB can produce the ions that become the precursors for the nanomaterials they generate; for instance, *Shewanella putrifaciens*, when provided with dissolved ferric iron (Fe_{3+}) and thiosulfate ($\text{S}_2\text{O}_3^{2-}$), could reduce these to ferrous iron (Fe^{2+}) and sulfide (S^{2-}), then precipitate iron sulfide (FeS) [24]. In many cases, the products generated may not have been electrochemically favored to form in a given system, and can only be produced using the active electron transport mechanisms that DMRB possess [25].

Finally, as alluded to in section 1.1.3, the use of DMRB is a highly versatile process involving an open electrochemical channel between the bacteria and their external environment. From the perspective of an engineer, this offers the potential for greatly enhanced control over

the synthesis process. In the following sections, we will discuss the various methods of control in greater detail.

1.1.4.2 Shape and Size Control

In biogenic nanoparticles, as in other crystals, shape and size control are fundamentally tied to the kinetics of crystal growth - under what circumstances a crystal is favored to form, and in what direction it is favored to grow. Once a crystal has nucleated and a lattice of a particular material has begun to form, atoms that come in contact with the lattice and have a site to which to adhere will tend to do so as governed by the surface free energy of the crystal. As time passes, crystals will tend to grow until they reach an equilibrium size, and smaller crystals will tend to redissolve and incorporate into larger ones in an effect known as Ostwald ripening. This means that additional incubation time will tend to produce larger crystals until the equilibrium size is reached [27]. Because temperature also interacts with the kinetics of chemical reactions, there is some evidence the temperature can either increase or decrease nanoparticle size as well, although a simple relationship that applies to all cases has not been observed [28].

One limiting factor on this growth, however, is the effect of capping agents; that is, materials of different composition than the crystal that coat the crystal surface and alter the free surface energy. In both biological and nonbiological systems, evidence suggests that capping agents can limit crystal growth size. Furthermore, capping agents may bind preferentially to one crystal face or another, causing preferential growth in specific directions and affecting the crystal shape. Experiments with non-biological nanoparticle synthesis have used organic molecules such as mercaptoethanol to accomplish this effect. [26] In biological systems such as the bacterial ones in this work, the same effect can be achieved via the tendency for bacteria to coat the nanoparticles with EPS or other proteins. Different species may affect nanoparticle shape and size in different ways depending on how these proteins interact with crystal surfaces, or genetic

engineering may allow this effect to be tuned, as has been previously demonstrated in some species of magnetotactic bacteria [29].

1.1.4.3 Effect of Electron Donor and Acceptor Concentrations

Since electron donors and electron acceptors drive cell metabolism, changing their concentrations will significantly affect bacterially-synthesized nanoparticle production. The concentration of electron donors and acceptors is critical in determining how much bacterial growth can occur and whether the growth is ultimately electron donor-limited or electron acceptor-limited. As we have discussed before, some metal-reducing bacteria produce nanoparticles specifically in response to electron acceptor limitation [5], [30]. Furthermore, since multiple types of electron donor and acceptor materials may be present, the relative concentration of these may have an impact on synthesis in a system in which more than one is present. Bacteria may tend to preferentially utilize one electron acceptor and generate one type of nanoparticle as a result, but switch to a different electron acceptor, and synthesize a different material, when the preferred material is absent [31].

1.1.4.4 Effect of pH/Eh

Since biomineralization is an electrochemical process, it responds to both the pH and the voltage (Eh) of a system. This effect unfolds in several ways. First, each strain of bacteria is adapted for a certain optimal range of pH conditions, and a pH outside of the ideal range will negatively influence growth rates, while also changing the solubility of ions in solution and altering their tendency to precipitate [31].

Bacteria also often respond to an applied voltage. For instance, Friman et. al cultivated *Pseudomonas putida* F1 in a chemically-defined medium inside a biochemical cell and applied various voltages to the culture, finding that higher positive voltages led to additional cell growth. This effect is presumably due to the ability of a positively-biased working electrode to act as an

electron acceptor for the bacteria, as discussed earlier in this section. The other significant effect of changes in Eh or pH is the direct effect on the system's mineral stability. The stability of different minerals in solution is influenced by both Eh and pH and can be visualized using a Pourbaix diagram. The voltage and pH of a given system will define which minerals are electrochemically favored to form, and bacteria may trigger the precipitation on these minerals. If the bacteria perform dissimilatory metal reduction, they may succeed in producing minerals that would not normally be electrochemically favored in a given system. If so, the stability can be predicted as that of the underlying system plus a "correction" effect along the vertical axis of the Pourbaix diagram, representing dissimilatory metal reduction [32], [33], [34].

In summary, incubation time, temperature, pH, Eh, and electron donor and acceptor concentration can all have significant impacts on the minerals that form in a system containing bacteria and nutrients, forcing us to control many variables to get reliable synthesis but also giving many potential ways to influence the system. In the next section, we will talk about the properties of the nanoparticles themselves in greater depth.

1.1.5 The Physics and Chemistry of Nanomaterials

In the previous sections, we examined the biological processes by which bacterial metabolic processes can produce semiconductor nanoparticles through biomineralization. Now we will examine the physical phenomena that give semiconductor nanoparticles their properties.

1.1.5.1 Traditional Synthesis Methods

Despite the great interest in the synthesis of semiconductor nanoparticles for electronic and biomedical device applications, a substantial amount of work remains in understanding the physical and chemical processes that underlie their formation and growth. As discussed in the previous section, the formation of larger crystals is energetically more favorable due to such crystals' smaller surface energy. Several standard methods of nanoparticle synthesis exist, all of

which must somehow halt crystallization at small size ranges. One common method is to utilize a precipitation reaction involving reactants that form an insoluble product from aqueous solution, generally at or near room temperature. Other liquid-phase synthesis methods exist that rely on a heat-induced reaction rather than precipitation, and this may be aqueous or require a solvent such as toluene. In the liquid-phase, these reactions often include stabilizer ingredients which coat the nanoparticles as they form, covering the potential growth sites at the surface of the crystals and halting their size in the nanoscale range. Finally, in addition to these methods, there exist gas-phase deposition methods for nanoparticle production. While these methods allow excellent process control and do not require the chemical additives used in the liquid-phase methods, gas-phase deposition requires very high temperatures, and the elements to be deposited must be first prepared in pure form prior to evaporation [35].

1.1.5.2 Size Effects

In bulk semiconductor materials, electronic band gap behavior arises primarily from the lattice - the geometry, the size between atoms, and lattice composition. The periodic potential arising from the lattice is the primary effect on the wavefunction of the electrons, forcing it to deviate to various degrees from the behavior of a free electron. However, some crystals are so small that the actual extent of the quantum dot is on the same length scale as an electron's de Broglie wavelength. In such cases, the electron begins to exhibit the behavior of being confined in a potential well, and this behavior becomes increasingly dominant as the size of the crystal decreases. This phenomenon is known as quantum confinement, and it causes the gap between the electron's energy levels to grow larger as the crystal becomes smaller. This means that quantum dots with a direct band gap in the energy range of the visible light spectrum will shift toward responding to shorter, and more blue, wavelengths of light as they become smaller. Quantum dots are of interest to semiconductor device engineers because their properties can be "tuned" by changing their size, even while their composition remains constant [35].

1.1.5.3 Compositional Effects

Beyond the distinctions in lattice type, semiconductor properties are heavily influenced by dopants - additive atoms that act as either electron donors or electron acceptors within the crystal. Such dopants can improve the characteristics of semiconductors by improving carrier concentration, but adding a sufficient number can also damage carrier mobility because the dopant atoms differ from the composition of the surrounding crystal and therefore have different lattice constants than surrounding atoms, progressively deforming the crystal as their numbers grow [36].

The effect of dopants in semiconductor nanoparticles is significant, as is the case in their bulk counterpart materials. The mathematical models used to understand the impact of dopants in a bulk material rely on the statistical interpretation of a large number of dopant atoms in a volume many orders of magnitude larger than a single unit cell of the lattice. However, since semiconductor nanoparticles are often only tens or hundreds of unit cells in diameter, the statistical models used to understand bulk materials are insufficient, and individual dopant atoms can have measurable effects on the properties of the entire nanocrystal. For instance, Sahu et al. showed that adding Cu impurities to CdSe/CdS quantum dots diminished their fluorescence by a factor of 100, but adding Ag impurities to CdSe crystals improved their fluorescence by a factor of 10 [37]. In the same manner, individual molecules of organic material, or other impurities or defects, may significantly alter the behavior of the nanomaterial, with some researchers reporting that differences in behavior can arise not only from the number of defects but also from their location in the nanocrystal [38].

1.1.5.4 Shape Effects

Nanoparticles can form in a variety of different shapes. Not only do spherical nanoparticles exist; there are also cubic and octahedral nanoparticles, nanorods, nanoplates, teardrop-shaped nanoparticles, and many more. As a result, a single measurement of diameter is insufficient to

talk about the dynamics of many nanoparticles - instead, knowledge of the nanoparticles' shape is required.

In some cases, quantum confinement effects can be anisotropic if the dimensions of a material are small enough to produce quantum confinement effects along one or more axes but not along others. Particles that exhibit quantum confinement lengths along every axis exhibit "three-dimensional" quantum confinement and are referred to as quantum dots. At the same time, a bulk solid would be said to exhibit "zero-dimensional" confinement - no quantum confinement effects at all. Between these two extremes are solids exhibiting two-dimensional confinement (quantum wires), and one-dimensional confinement (quantum wells). [39]. It is worth noting on the other hand that quantum wires, though they produce less quantum confinement, have the structural advantage of being longer and therefore able to stretch between key contact points in electronic devices, as was demonstrated by McFarlane et al [40].

Beyond the issue of confinement dimensions, shape has other effects on the electronic dynamics of crystals. In conductive materials, oscillations called plasmons occur in the cloud of free electrons at the materials' surfaces. In nanoparticles of metallic or semiconductive material, these effects become a significant factor in the particles' response to light due to the large surface-area-to-volume ratio of such particles. The shape and dimensions of a nanoparticle can give rise to specific plasmon resonance modes, which then create light absorption and scattering peaks for wavelengths of light that correspond to the resonance modes. [41] This effect can be significant enough to dramatically affect the photonic behavior of the particles, as in the case of silver nanoparticles, which have been observed to emit red, green or blue wavelengths, as well as others, depending on their shapes [42]. For nanoparticles of certain shapes, surface plasmon resonance can even result in the emission of polarized light, as in the case of CdSe quantum dots, which have been shown to emit light that is linearly polarized along the axis of their longest dimension [43].

1.1.5.5 Effects of Coatings

In earlier sections, we addressed the methods of nanoparticle synthesis, which include adding stabilizing agents which adhere to the surface of the nanoparticles. However, such coatings do more than impact the crystal growth. Once the nanoparticle has formed, these coatings also impact the electronic behavior, and as such, coatings are sometimes added specifically for this purpose.

One valuable effect of coating nanoparticles is that of passivating their surface states. At the edges of each nanocrystal, the discontinuation of the lattice, and the resulting dangling bonds will create trap states with electronic behavior different from that of the lattice. Such trap states may engage in photoemission or other behaviors similar to that of the lattice portion of the nanocrystal, but their behavior will generally be less unpredictable and less responsive to the “tuning” effects commonly employed with nanoparticles, such as changes in size. A coating that binds strongly to the surface of the nanocrystal will eliminate these trap states, which can enhance emission and improve the regularity of their response. One research group, for instance, found that CdS nanocrystals that typically exhibited an orange light emission band could be induced to instead emit blue light if their trap states were passivated with a coating of cysteine ester [35]. Finally, any coatings that are used will significantly affect the surface plasmon resonance, possibly shifting or eliminated measured surface plasmon resonance peaks [41].

1.1.6 Bacterial Biofilms and their Environmental Interactions

A final aspect of microbiology worth considering is that of biofilms, which are higher-order systems that can contain all the phenomena described in the previous sections. A scanning electron microscope image of a bacterial colony will sometimes show individual, isolated cell bodies, but often what is visible is a more complex, aggregated structure consisting of many bacteria, often bound together by extracellular polysaccharides or other secretions. In a biofilm, bacteria may form gradients of oxygen concentration or pH such that the interior of the biofilm is

more suitable for bacterial growth than the exterior. Nanowires may extend between bacteria in the biofilm to form long conductive channels through which electrons can be shared over a range of many microns. If biomineralization occurs, it may occur differently in different parts of the biofilm. In some cases, multiple species may even inhabit different parts of a biofilm in a symbiotic relationship. Although not understood until well into the 20th century, biofilms are now known to be essential to bacterial life [44].

As a biofilm forms, some bacteria will maintain contact with the environment while others will become buried inside, and over time, this triggers changes in bacterial gene expression in different parts of the biofilm. Bacteria will begin to functionally differentiate, with some focusing on metabolic activity and others focusing on tasks such as quorum sensing (chemically detecting the number of local bacteria to prevent overpopulation) or the release of chemicals that assist free-floating bacteria in overcoming antimicrobial agents. Throughout the biofilm, a communication network shuttles biochemical signals between bacteria and allows the entire biofilm to sense the various conditions of its surroundings and internal processes and respond accordingly [45].

Understanding biofilms is vital in order to give us a picture of how colonies of bacteria interact with the environment they inhabit, including artificially-produced substrates or biosensors. In the following sections we will consider how dissimilatory metal-reducing bacteria, their biomineralized products, and their biofilms might play a role in future avenues for nanotechnology, sensors, and electronics.

1.2 Motivation

The use of bacteria in the creation of semiconductor nanoparticles and sensors offers the potential to improve upon existing technologies in several respects. This section will explore these potential contributions in greater detail. The bacterium *Shewanella oneidensis* MR-1 was selected as the target organism for this work for several reasons. First, *Shewanella* is a dissimilatory metal-reducing bacterium with a highly versatile metabolism, able to extracellularly reduce thiosulfate, sulfite, and a range of metal ions [46]. Second, as discussed earlier in this work, studies of *Shewanella* provide robust evidence of the formation of conductive bacterial nanowires under conditions of electron acceptor limitation. This offers opportunities to look for the formation of these structures as evidence of biomineral formation, and also provides opportunities to study the bacteria-substrate interface. Third, *Shewanella* is metabolically versatile; it is a facultative anaerobe, able to grow either in the presence or absence of oxygen. This simplifies the cultivation and incubation process. Strict anaerobes like *Desulfovibrio vulgaris* require a carefully-controlled anaerobic growth environment and their cultivation generally employs chemical reducing agents and an anaerobic glovebox. For these organisms, any oxygen contamination present in the growth medium will adversely impact the bacteria and the production of nanoparticles. By comparison, *Shewanella oneidensis* MR-1 will readily enter an anaerobic metabolic state and produce nanoparticles in a growth medium that has had dissolved oxygen removed through a simple nitrogen bubbling procedure, and will continue to produce nanoparticles even if a small amount of oxygen is present. [47].

1.2.1 Advantages of Bacterial Nanoparticle Synthesis

Section 1.1.5 of this work described the traditional chemical processes for synthesizing semiconductor nanoparticles, which include both aqueous and gas-phase methods. As discussed in earlier sections, it is commonplace for such methods to require the input of heat and chemical

surfactants in order to produce nanoparticles of the desired size and composition. Bacteria, on the other hand, can cause comparable synthesis to occur at room temperature with no chemical surfactants added. This is due to two factors. One factor, previously discussed in section 1.1.4, is the ability of such bacteria to act as a catalyst for the reactions that produce nanoparticles, allowing the reactions to become thermodynamically favorable at lower temperatures. Another factor is the ability of bacterial secretions to act as a capping agent, performing a function in nanoparticle synthesis that must otherwise be performed by a chemical additive [48]. In the chart below, several previously-reported instances of bacterial nanoparticle synthesis are compared to non-biological methods.

Table 1: A Comparison of biological and non-biological nanoparticle synthesis.

Nanoparticulate Material	Bacterium Capable of Synthesizing	Nonbiological synthesis method requires heat or organic solvents?
CdTe	<i>E. coli</i> [25]	Yes [25]
CdS	<i>Shewanella oneidensis</i> MR-1 [49]	Yes [50]
PbS	<i>Rhodobacter sphaeroides</i> . [51]	Yes [52]
As ₂ S ₃	<i>Shewanella oneidensis</i> MR- 1 [53]	Yes [54]
CdSe	<i>Pseudomonas sp. strain RB</i> [55]	Yes [56]
UO ₂	<i>Shewanella oneidensis</i> MR-1 [57]	Yes [58]
ZnO	<i>Lactobacillus sporogenes</i> [59]	Yes [60]

1.2.2 Bioremediation

Applications for biosynthesized nanoparticle synthesis exist beyond semiconductor device fabrication. As dissolved ions precipitate out of a solution, their concentration in the solution

decreases. In many cases - as in the case of dissolved lead, cadmium, and selenium ions - the presence of dissolved metals can present a health risk to humans as well as other animals, and consequently, processes that effectively remove these ions from the water may have potential as bioremediation methods. If semiconductor nanoparticle biosynthesis can be implemented on an industrial scale, it may allow the creation of a system in which contaminated wastewater is fed into a bioreactor, metal-reducing bacteria trigger a precipitation reaction, a separation step is performed, and two outputs are recovered: semiconductor nanoparticles and water with fewer dissolved toxins [61].

1.2.3 Electrochemically and Photonically Active Living Sensors

Earlier background sections have established the myriad uses for bacterially-synthesized nanoparticles, from the harvesting of these nanoparticles for electronics and photonics applications to the use of the biosynthesis process for bioremediation. However, additional applications exist when living biofilms are incorporated into engineered platforms capable of interacting with them.

Prior experiments have explored the use of such systems for so-called "microbial fuel cells" in which biofilm metabolic activity on a solid electrode produces a measurable current that can then transfer to an external system. The current density in such systems as designed thus far has proven to be low, hampering the possibilities for substantial renewable power generation using these systems [11]. However, because microbial fuel cells are a living system, their current production is responsive to all variables that affect bacterial metabolism, such as pH [62], dissolved organic matter [63], and temperature [64], raising the possibility that a microbial fuel cell can be utilized as a biosensor for the detection for several environmental variables simultaneously.

Additional considerations arise from the fact that if a microbial fuel cell exists under conditions that also facilitate biomineralization, the result will be a solid system in an aqueous

medium consisting of an electrode, living bacteria, and nanoparticles that may produce photocurrent when stimulated with light. Prior studies indicate that films on semiconductor nanocrystals on an electrode can be characterized using cyclic voltammetry in the same manner as living biofilms can be characterized in a microbial fuel cell [65]. Hence, a living biosensor system that contains semiconductor nanoparticles may be responsive to still more environmental perturbations via the electrochemical and photocatalytic properties of these particles.

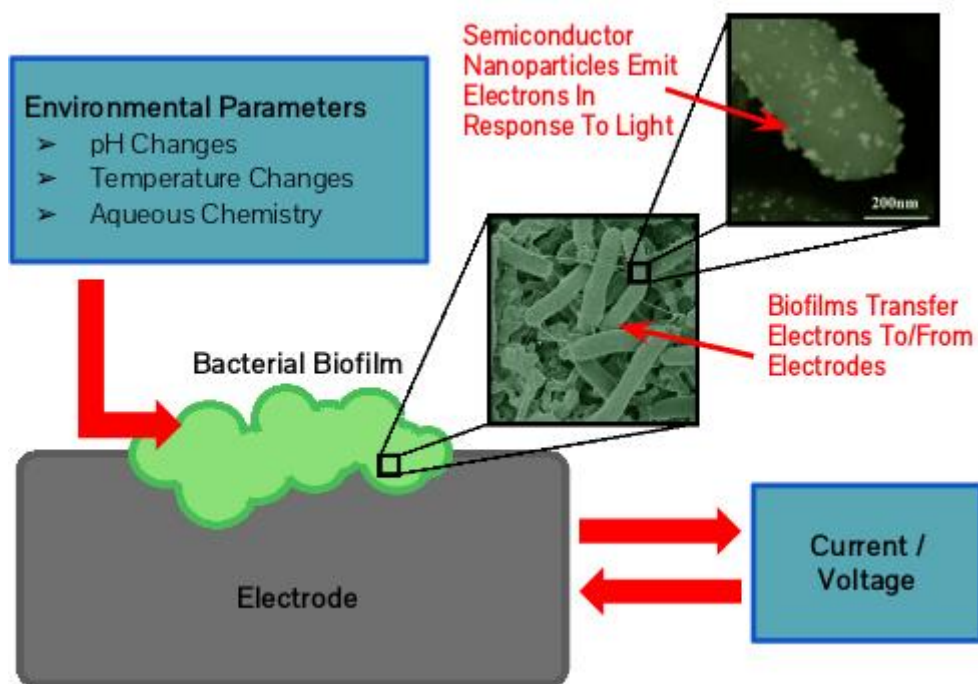


Figure 1: A multi-input biosensor containing DMRB.

1.3 Methods

1.3.1 Cultivation and Incubation

Previously-frozen *Shewanella oneidensis* MR-1 glycerol stock cultures were obtained from the American Type Culture Collection (ATCC) and warmed to room temperature. Starter cultures were prepared by injecting the glycerol stock cultures (approximately 1 mL each) into a 50 mL volume of sterile chemically-defined media prepared according to the recipe described in the Appendix. These starter cultures were allowed to grow aerobically in bottles at room temperature in a sterile hood until visual inspection revealed increased solution opacity or a biofilm at the liquid's surface, indicating *Shewanella* growth.

Once stock cultures were verified to be growing, an incubation medium was prepared according to the same standard recipe but making modifications as needed for individual experiments as described in the corresponding results sections. The incubation medium was also separated into 50 mL batches and bubbled for 30 minutes to remove dissolved oxygen, then autoclaved at 121°C to 45 minutes to fully sterilize the media. Inoculum from the culture bottles described above was injected into the bottles in a volume equal to 5% of the incubation medium. For the biomineral synthesis experiments described in sections 2, 3 and 4, potassium phosphate monobasic, a buffer salt included in the standard *Shewanella* medium, was excluded due to an observed tendency for *Shewanella* batches containing this salt to form phosphate precipitates that interfered with the observation of biofilms and nanoparticles in SEM imaging. This phenomenon will be described in greater detail in Chapter 5.

1.3.2 Scanning Electron Microscopy

Scanning Electron Microscopy (SEM) is one of the most versatile techniques for the topographical imaging of both biominerals and bacteria. In SEM, a high-energy electron beam

(generally in the range of 5-40 keV) is focused on the sample and scanned across the surface in a series of scanned lines. This process excites the emission of electrons from the surface of the sample in a manner that is dependent on various properties of the sample at the site currently under the beam. Once the electrons are generated, they are collected by a detector and the resulting data is processed into an image. The resolution of this technique is generally on the order of a few nanometers if the SEM is properly calibrated [66].

While SEM is very effective for generating images of bacteria, nanowires and nanocrystals, it usually cannot be used to precisely identify the chemical formulae for most materials, such as the nanocrystals that the proposed work seeks to generate. For chemical identification, other techniques will be employed as discussed below.

Images in this work were generated with either a Carl Zeiss 55 Supra FESEM. For the SEM/EDS biomineral analysis performed in chapters 2, 3 and 4, material was harvested from the cultivation bottles using a sterile needle and applied to a clean silicon slab. The samples were first placed in a nitrogen-bubbled anaerobic solution of standard *Shewanella oneidensis* MR-1 media (as described in the Appendix) combined with 2.5% glutaraldehyde and allowed to fix overnight in a fume hood. Next, the samples were dehydrated via submersion in a mixture of deionized water and increasing concentrations of ethanol - first 10% ethanol by volume, then 25%, 50%, 75%, and finally 100% ethanol. The samples were left refrigerated in ethanol overnight, then on the following day were dried using either an Autosamdry critical point dryer or via submersion in a mixture of ethanol and hexamethyldisilazane (HMDS). First 33%, then 66%, and finally 100% HMDS were used. Samples were allowed to air dry in a fume hood overnight. A Denton Desk VI sputter coater was used to deposit approximately 5 nm of platinum onto the sample to reduce sample charging during SEM imaging.

1.3.3 Energy-dispersive X-ray Spectroscopy

Energy-dispersive X-ray spectroscopy, or EDS, is a method for performing analysis of the

elements present in a sample. The method works by exciting the atoms of a sample using an X-ray source. If one of the sample atoms' inner-shell electrons is excited, it may be ejected from the sample. An electron in an excited state can then drop into the hole vacated by the original electron, emitting an X-ray. These X-rays' energies are characteristic of the element they came from and also of the transition level. Thus, they can be used to identify the element.

This technology has several limitations. Due to the mechanism of X-ray emission from the excited atoms, only atoms of sufficient atomic number can be imaged this way - specifically, the elements must have a higher atomic number than Beryllium. The detection limit in terms of elemental concentration is around 1000-3000 parts per million. The energy band resolution is generally around 130 eV, which may under some circumstances lead to difficulty in distinguishing two transition bands. The spatial resolution is on the order of microns, which is sufficient to image bacteria or many types of small crystals or particles but insufficient for the imaging of objects on the size scale of quantum dots.

EDS is generally combined with SEM, which complements it by providing a topographical reference image. Once a point or region is selected for elemental analysis, a spectrum is generated. Peak heights in the spectrum can be compared in order to allow quantitative elemental analysis, which will tell the users what percentage of each element is present in the sample by weight or atom count [67]. Given that semiconductor nanoparticles will tend to comprise a relatively small percentage of the matter in a given interaction volume during EDS analysis, the exact concentrations of elements in the samples, and therefore absolute confirmation of nanoparticles present, will be difficult to ascertain using EDS techniques. However, using SEM in conjunction with EDS will allow the qualitative mapping of the presence of certain elements to topographical features in bacterial biofilms to infer which nanoparticles may be present and what relationship they may have with the biofilms. Additional analysis methods, described in the following sections, may then be used for confirmation of nanoparticle composition.

All SEM and EDS work was performed using a Carl Zeiss 55 Supra FESEM with an Oxford

EDS system attached. The microscope was operated at a 4e^{-6} torr high vacuum.

1.3.4 Transmission Electron Microscopy

Transmission electron microscopy is a technique involving the passage of very high-energy electrons (100 keV or more) through a sample. Its advantages include very high magnification (200,000x) and extremely high resolution, able to resolve features on the atomic scale. Due to its reliance on transmission, TEM requires the preparation of a very thin sample, ideally less than 50 nanometers in thickness. The excellent elemental and thickness contrast, along with the aforementioned high resolution, make TEM an excellent technique for imaging bacteria and the semiconductor nanoparticles synthesized by bacteria [68].

TEM has two main modes: imaging mode and diffraction mode. These two modes produce different images and reveal different information about the sample being imaged. In imaging mode, the TEM generates a high-magnification image of a sample. Because the brightness or darkness of the image at a given point depends on the electron transmission through the sample at that point, this image reveals some of the sample's physical attributes. For instance, thickness contrast occurs - thicker parts of the sample will appear darker due to the presence of more matter to halt electrons in the beam. An atomic number contrast also exists, whereby heavier elements with more charge in their nuclei deflect passing electrons more effectively and cause the regions with heavier elements to appear darker. A third effect is diffraction contrast, in which patterns of light and dark can appear in crystalline areas of the sample as electrons deflecting at certain angles satisfy the Bragg condition:

$$n\lambda = 2d \sin \theta \quad (5)$$

In the equation above, λ represents the de Broglie wavelength of the electron, n represents the diffraction order, d represents the spacing (often called d-spacing) between planes and θ represents the angle of incidence [68].

The other common TEM mode - diffraction mode - utilizes this effect more directly, focusing the beam on a small region of the sample (often only a few hundred nanometers in diameter) and displaying the area's diffraction pattern. [68]. Since different atoms experience slightly different attractive and repulsive forces toward one another based on their atomic mass, orbital structure, and other internal factors, the d-spacings will be characteristic of the elements present in the crystal and the diffraction pattern generated by X-rays in the crystal can be used to uniquely identify the composition of the crystal. For monocrystalline samples, this leads to a spot diffraction pattern which can be compared to the pattern generated by known crystal structures to confirm the crystal structure. For polycrystalline, amorphous or structurally-flawed materials, the patterns will tend to be more complex; they may exhibit overlaid diffraction patterns, the diffraction patterns may be weak, or no diffraction at all may be visible [68].

The TEM work presented in this thesis was completed using a JEM 2010 TEM operating at 200kV.

1.3.5 X-ray Powder Diffraction

X-ray powder diffraction (XRD) is a material analysis technique that involves bombarding a sample of crystalline particles with electrons and recording the resulting diffraction patterns. These patterns are not produced by the electrons directly. Instead, the electrons, which strike the sample at high energies from a cathode ray tube, produce excitations in the sample material that result in the emission of X-rays. Like the X-rays produced in the EDS imaging technique described in 1.3.3, these X-rays have energies that are characteristic of the elements from which they were emitted. Much like the electron beam used in TEM, the X-rays produced in XRD also satisfy, and produce diffraction patterns according to, the Bragg condition. The XRD detector then records the intensity of the diffracted X-rays across a range of angles. This means that XRD is an effective technique for both chemical and structural analysis of a sample. XRD also boasts relatively simple

sample preparation; just a few hundred milligrams of material in powder form is sufficient for analysis [69].

Once data is retrieved from the sample, the peak angles measured can be compared to recorded crystallographic measurements from a database or mathematical calculations based on the expected composition and morphology of the sample. There are a number of secondary effects that may alter the shape and location of the peaks generated. Firstly, XRD can give an indication of the degree of a sample's crystallinity; highly crystalline materials will generally produce strong, sharp peaks while more disordered materials will produce much broader peaks or no peaks at all. If the crystals are strained or contain dopants, the resulting changes to the crystals' lattice constants can produce a shift in the peaks generated. (If the strain or dopant effects are non-uniform throughout the sample, this will likely manifest as peak broadening [69].)

In this work, all XRD measurements were performed using a PANalytical X'Pert PRO XRD system using a copper X-ray source.

1.3.6 Cyclic Voltammetry

In cyclic voltammetry, a DC voltage is applied into an electrochemical system. This voltage is defined between a working electrode and a reference electrode, and the current is measured between the working electrode and a third electrode, called the counter electrode. The voltage difference between the two electrodes is swept upward from 0V until it reaches a terminal value, then swept downwards to a complementary negative value before being swept to 0V again.

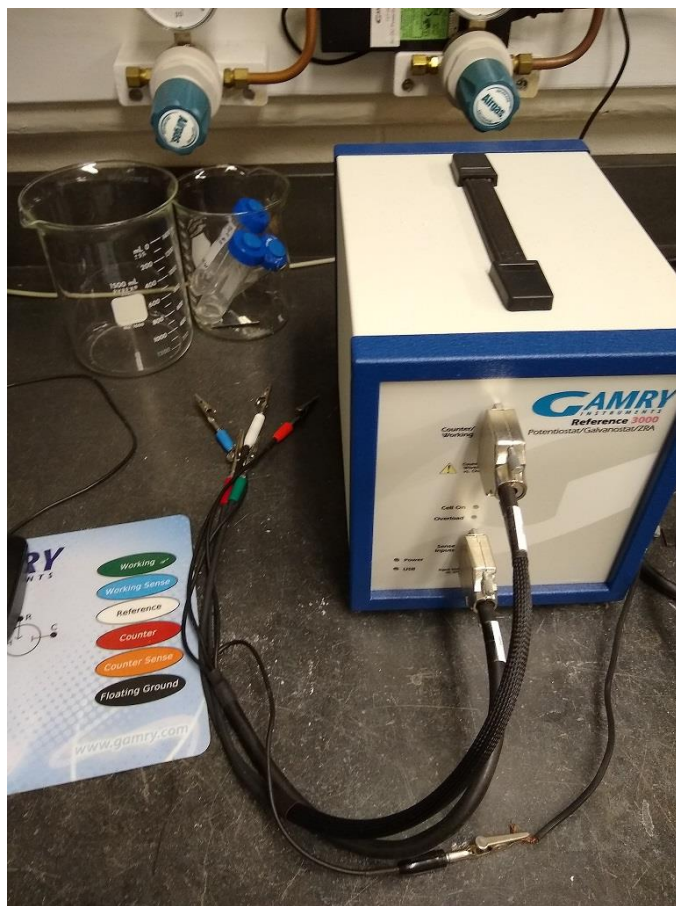


Figure 2: Gamry Reference 3000 potentiostat with attached electrode leads.

Consider a simple electrochemical system in which a relatively uniform material exists that undergoes reduction or oxidation at well-defined potentials. As this potential increases, the working electrode can cause reduction to occur and positive cathodic current to flow. In the negative potential direction, it becomes an anode, causes negative anodic current to flow, and triggers oxidation. This oxidation peaks visibly as the potential hits the peak potential necessary to trigger the redox reaction before falling off gradually as the material available to be reduced or oxidized is depleted [70], [71].

Several features of the CV curve offer valuable information about electrochemical phenomena within the system. First, the locations of forward and reverse redox peaks provide information about what voltages are required to trigger the system's redox reactions. Second, if the redox reactions occurring during the cycle are reversible, the forward and reverse currents

should be equal in magnitude. There are also several features of interests that are dependent on scan rate. The peak current observed in a redox event is governed by the Randles-Sevcik equation:

$$i_p = 0.4463nFAC \sqrt{\frac{nFvD}{RT}} \quad (6)$$

In the equation above n represents the number of electrons transferred in the reaction, F is the Faraday constant, A is the electrode area in square centimeters, C is the reactant concentration in moles per cubic centimeter, v is the scan rate in volts per second. D is the diffusion coefficient of the reaction in square centimeters per second, R is the gas constant, and T is the temperature.

From the Randles-Sevcik equation we see that if a reaction is indeed invariant with scan rate, the height of its redox peak should increase as the square root of scan rate. If this does not occur, it implies another scan rate-dependent behavior, such as change in the diffusion coefficient with increasing scan rate [72].

Real electrochemical systems, especially biological ones, will often exhibit curves with more complex features. In this work such features will be discussed in the accompanying data sections. All cyclic voltammetry work in this thesis was performed using a Gamry Reference 3000 potentiostat, a Gamry Ag/AgCl reference electrode, and a titanium wire counter electrode. Reference electrodes were tailored to each experiment and will be discussed in the relevant sections.

1.3.7 UV-Vis Absorption Spectroscopy

Absorption spectrometry is a method of optical characterization of a sample by quantifying its absorption of light across a range of wavelengths. A lamp is used to pass light through a sample, then the amount of light that is transmitted through the sample is measured by a detector

on the other side and a spectrum is created. At a given wavelength, two quantities define this absorption. One is the transmittance, which is the ratio of radiant flux into the sample versus radiant flux out of the sample. The other quantity is absorbance, a dimensionless quantity that represents the probability of an incident photon being absorbed by a sample molecule while traveling a given distance through the sample. Because this absorption is probabilistic, the transmittance tends to decrease exponentially at a given absorbance as the path length through the sample increases. Thus, transmittance is an *extensive* property while absorbance is an *intensive* property, and is the most useful for qualitatively describing the sample's material properties. The relationship between transmittance and absorbance is related by the Beer-Lambert Law:

$$\log_{10}T = \epsilon lc \quad (7)$$

where ϵ is a constant, c is the solution concentration, T is the transmittance, and l is the distance through which the light passes in the solution [73].

For the purpose of our analysis, the wavelengths of interests are either in the visible light range (wavelengths of 400-700 nm) or in the low ultraviolet range; hence we refer to this method as UV-Vis absorption spectroscopy. In this work we employ a Shimadzu UV-Vis 2550 spectrophotometer with a dual deuterium lamp and halogen lamps. The halogen lamp is used for wavelengths 280 nm-1100 nm and the deuterium lamp is employed for 190-390 nm. A switch between the two lamps occurs at 330 nm.

1.3.8 Raman Spectroscopy

Raman spectroscopy is a method of using a laser to characterize the chemical composition of a sample based on Raman scattering. When a beam of light passes into a material, a certain amount of that light is scattered by bound electrons in the sample that absorb a photon, enter an excited state, and then emit a photon as they leave the excited state. The majority of

these electrons fall back to the same energy level as before and emit a photon of with the same energy as the one they absorbed. This process is known as Rayleigh scattering. However, in a minority (approximately 1%) of cases, the electron will drop to a final energy level different from its initial energy level, emitting a photon with a different wavelength than the incident photon. This process is called Raman scattering, and it is used to construct a Raman spectrum showing the amount of light emitted from the sample at a range of wavelength in response to stimulation of the sample with light of a single wavelength. Because the allowed energy levels of an electron in the sample are characteristic of the atoms present as well as the chemical bonds between them, the “Raman peaks” that appear in a Raman spectrograph provide detailed chemical information, as well as some structural information, about the sample being studied. Furthermore, Raman spectroscopy offers the benefit of versatile analysis - the sample can be in bulk solid, liquid, or powder form, and can be studied at a range of temperatures [74].

Although Raman spectroscopy can analyze samples in a range of different states, it is important to be aware of how the state of the sample can shift or otherwise alter the Raman peaks. While crystalline solids tend to have strong, clear peaks, liquids or amorphous solids have broader peaks due to the larger number of vibrational modes available in their molecules. Increased sample temperature can lead to peak broadening as the increase in energy leads to a large number of accessible rotational states in each molecule. Changes in temperature can also lead either an upward or downward shift in Raman peaks due to the temperature’s effect on molecular bond lengths, which will vary depending on the molecule. Stress and strain effects can also alter bond lengths and therefore induce a Raman peak shift [75]. For nanoscale crystals (especially below 30 nm), studies have found a tendency for the Raman peaks of a material to shift downward and broaden as the nanoparticles decrease in size. Several physical mechanisms have been proposed to explain this, including phonon confinement. [76]

There are a few effects that may add additional peaks to the sample other than Raman peaks from the material of interest. First, the sample purity has an obvious effect; any material

present will exhibit Raman peaks in proportion to its concentration in the sample. The mounting of the sample may also introduce peaks characteristic of the mounting material; for instance, if the sample is suspended in solution or spread on a glass slide, the spectra of the solution or mounting material will appear in the data.

There are also several physical phenomena that can cause the material of interest to generate additional peaks. If the sample is in highly crystalline form, the lattice can exhibit vibrational modes of its own that create “lattice peaks” in the data. Furthermore, if the material becomes fluorescent in response to the laser excitation, a broad fluorescence peak will likely appear in the data. Methods exist for reducing fluorescence effects, such as illuminating the sample with a short series of short laser pulses rather than a single long pulse [74].

The Raman spectroscopy data in this work was collected using a Renishaw Ramascope Raman spectrometer and Leica DMLM optical microscope. Samples were prepared on clear glass microscope slides, and analysis was performed using a 514 nm laser.

1.4 Thesis Organization

This chapter has described the basic physical, chemical, and biological background theory necessary to understand how semiconductor nanoparticles can be synthesized by dissimilatory metal-reducing bacteria, what their physical properties are, and how the properties of these materials can be characterized. It also describes the potential applications for live DMRB in biosensing systems and the motivations for using such bacteria in a range of biotechnological applications.

Chapters 2, 3 and 4 present methods of using *Shewanella* bacteria for the synthesis of lead sulfide, cadmium sulfide and molybdenum disulfide, respectively. These chapters describe how a standard *Shewanella oneidensis* MR-1 growth medium is altered through the addition of metal salts to produce these three nanoparticulate materials, and describe the cultivation, incubation and characterization methods used to generate and study the materials generated. Finally, each section proposes the mechanism by which nanoparticle synthesis was achieved.

Chapter 5 describes several investigations of *Shewanella oneidensis* MR-1 interacting with solid materials in their growth medium. This includes topographical observations of how *Shewanella* grows in or on a series of substrates of value for electrical engineering applications. It also includes electrochemical characterizations of *Shewanella*'s interaction with solid electrodes using cyclic voltammetry. These electrochemical measurements provide preliminary evidence that *Shewanella*'s response to several environmental variables can be measured as a current response.

Chapter 6 summarizes the work of this thesis, discusses several lessons that arose from this work, and provides a preliminary road map for future work.

2. LEAD SULFIDE BIOSYNTHESIS

2.1 Introduction

In this chapter, I describe a method of using *Shewanella oneidensis* MR-1 to synthesize lead sulfide nanoparticles at room temperature. Lead (II) sulfide, or PbS, also known as galena, is a semiconductor with a direct band gap of 0.37eV, making it photoconductive in the infrared range [77]. It most commonly exhibits a face-centered cubic structure, although under high pressure it can form into an orthorhombic structure [78]. As a semiconductor, lead sulfide may be p-type, n-type or intrinsic, with extra lead atoms in the lattice acting as n-type dopants and additional sulfur atoms acting as p-type dopants. Due to lead sulfide nanoparticles' excellent infrared absorption properties, they have been investigated extensively for use in infrared photodetectors [79]. They have also been examined as a potential material for solar cells [80]. Biomineralization of lead sulfide via metal reduction has been reported using *Bacillus sp.* KK1 [81] and *Rhodobacter sphaeroides* [51]. Lead sulfide nanoparticles have also been synthesized using a room-temperature chemical synthesis method; however, this method required the addition of the hydrocarbon surfactant $C_{18}H_{37}O(CH_2CH_2O)_{10}H$, as well as the addition of the sulfide salt Na_2S [82]. To the best of our knowledge, this work represents the first controlled synthesis of PbS nanoparticles using *Shewanella oneidensis* MR-1 using the reduction of thiosulfate to sulfide and the first controlled synthesis in which bacterial nanowires have been shown associated with the precipitates *in situ*.

The biosynthesis of lead sulfide also offers significant potential environmental benefits, which serve as part of the motivation for targeting this material for synthesis. Lead (II) sulfide It is one of the least soluble natural lead compounds and therefore one of the least toxic to humans and other animals [83]. As a result, a microbial process that involves the production of lead sulfide from dissolved lead ions, such as those that occur in some aging plumbing systems [84], can be

a form of bioremediation with applications in areas where dissolved lead contamination has negative impacts on human health.

2.2 Incubation

In this experiment, eight batches of *Shewanella* culture were prepared as described in section 1.3.1, but with no monopotassium phosphate. These batches were cultivated in 150mL culture bottles with 50mL of liquid in each bottle and nitrogen in the remaining headspace. Sodium thiosulfate added to the medium as an electron acceptor. The media was bubbled with nitrogen for 20 minutes to remove dissolved oxygen and then were autoclaved for 45 minutes at 121°C to achieve sterilization. These bottles consisted of four distinct groups with two identical bottles in each group, as follows:

Table 2: Bottle groups for varied thiosulfate PbS synthesis experiment.

Group A	Added lead acetate to 10mM, sodium thiosulfate to 10mM, and 1 mL inoculum
Group B	Added lead acetate to 10mM, sodium thiosulfate to 20mM, and 1 mL inoculum
Group C	Added lead acetate to 10mM, sodium thiosulfate to 10mM, and no inoculum
Group D	Added lead acetate to 10mM, sodium thiosulfate to 20mM, and no inoculum

Once the bottles had returned to room temperature after autoclaving, the Group A and Group B bottles were injected with 1mL of live *Shewanella* culture prepared in the medium described in Appendix A, then were placed in an incubator and heated to a temperature of 30°C while also being agitated at 100 rpm. After 24 hours, lead acetate was added in the form of 0.5mL sterile 1.0M lead acetate solution. Both of the bottles in Group A and Group B instantaneously began to develop the dark color characteristic of precipitated lead sulfide, with group B, the group with the highest sodium thiosulfate concentration, exhibiting the most pronounced dark coloration. The bottles were re-inspected after 14 days. In the three bottles that had developed the coloration, black precipitates had now settled to the bottom of the bottles. The media in the other bottles remained transparent with no evidence of precipitates.



Figure 3: Development of PbS precipitates (top) and settling (bottom).

2.3 Characterization

2.3.1 Scanning Electron Microscopy / X-ray Energy Dispersive Spectrometry

Black precipitates were harvested from the cultivation bottles using a sterile needle and applied to a clean silicon slab, then dehydrated and dried using the alcohol / HMDS protocol. SEM imaging was then performing using the Supra 55 FESEM.

SEM imaging revealed substantial *Shewanella* biofilm growth. In the vicinity of the bacteria, a substance consisting of sub-micron grains could be seen. EDS analysis revealed that this substance consisted of primarily carbon and oxygen with a substantial amount of lead and sulfur present as well, suggesting that the substance consisted of *Shewanella*-secreted extracellular polysaccharides on which lead sulfide nanoparticles had begun to form. Some spherical deposits, as well as crystals several microns in length, could also be seen; these consisted primarily of carbon, oxygen and sodium and were presumably salt crystals resulting from the precipitation of the chemicals in the medium. In Figure 4, the green circles indicate bacteria, the yellow circles indicate extracellular polysaccharides and the red circles indicate spherical precipitates. Figure 5 shows an area EDS analysis revealing 68.92% carbon, 10.08% oxygen, 3% silicon, 11.15% sulfur, and 6.85% lead by atomic percentage.

Meanwhile, SEM performed on the sterile batches from this experiment revealed spherical and crystalline deposits similar to those observed in the inoculated batches, but with no bacteria or extracellular polysaccharides present. EDS area analysis performed on the sterile batches suggested the deposits in the sterile batch contained significantly less lead and sulfur than the inoculated batches. Figure 6 shows the area in which EDS analysis was performed; measurements here revealed 58.36% carbon, 9.11% oxygen, 29.43% silicon, 0.58% phosphorous 1.54% sulfur and 0.98% lead.

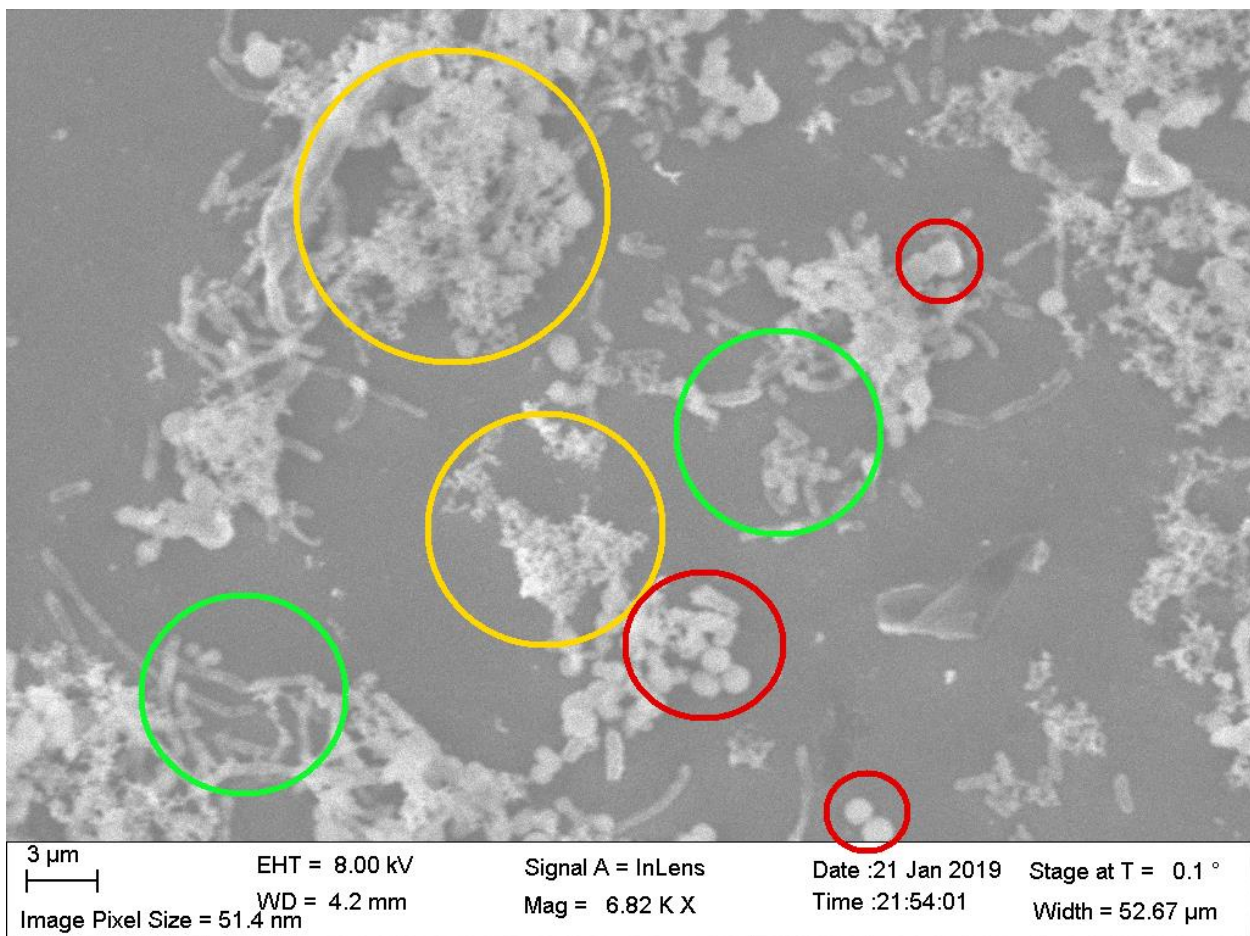


Figure 4: Precipitates in the inoculated 20mM thiosulfate batch.

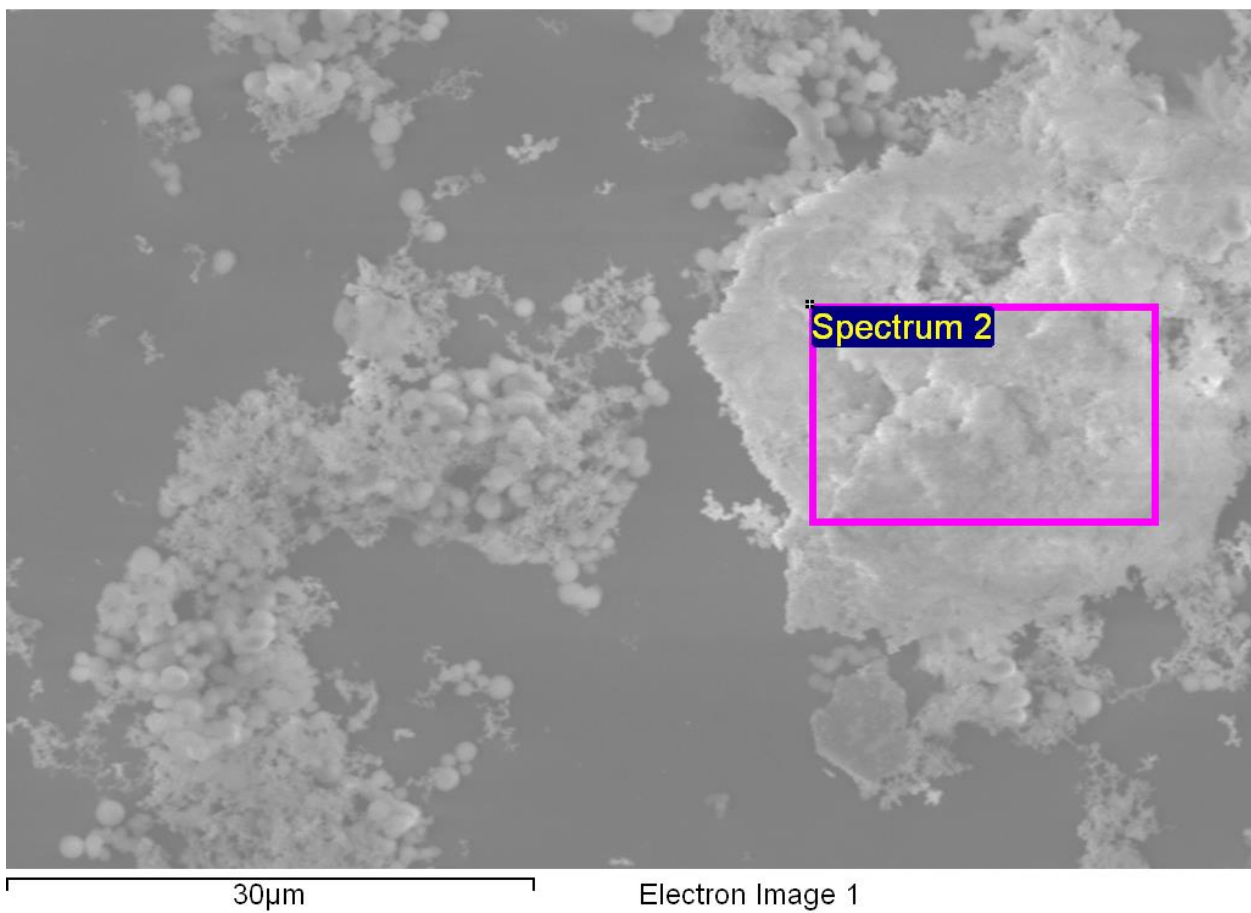


Figure 5: EDS area analysis of biofilm structure.

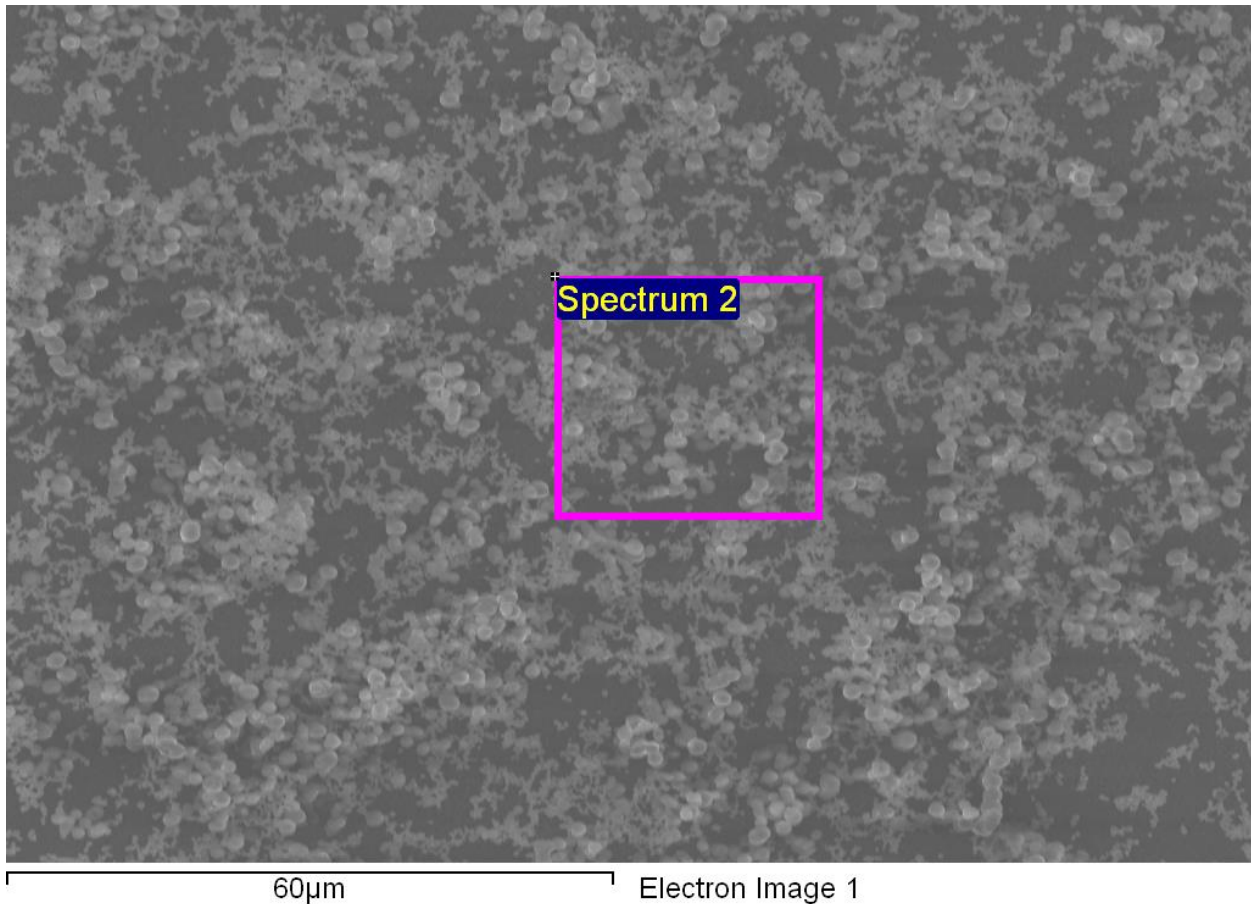


Figure 6: Precipitates in the sterile 20mM thiosulfate batch.

2.3.2 X-ray Diffraction

Contents of the Group B batches described in the previous section were placed in plastic tubes and centrifuged at 2000 rpm for 30 minutes. The supernatant was discarded and replaced with ethanol, then the bottles were shaken until the pellet was re-dispersed in the ethanol. Then the material was placed in a beaker and dried in a heater at 100°C overnight. The following day, the remaining material was ground into a powder and imaged using the XRD system described in section 1.3.5.

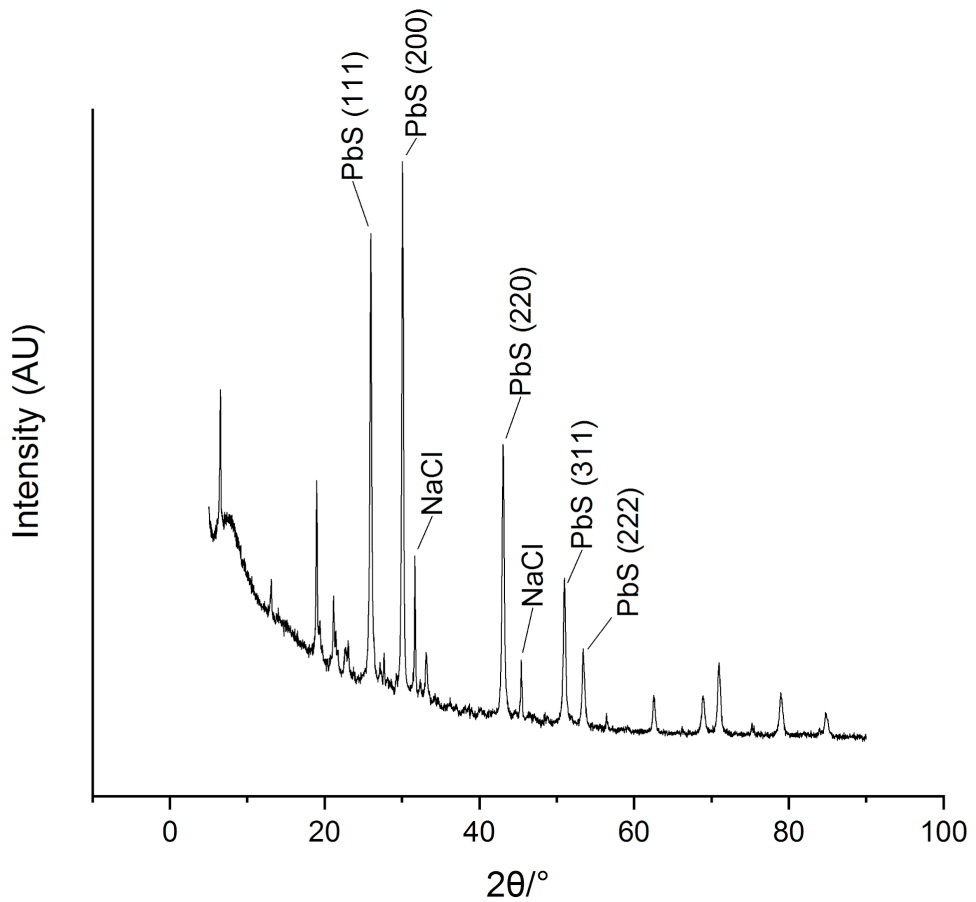
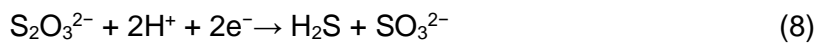


Figure 7: XRD diffractogram for the PbS nanoparticles generated.

The JCPDS data for lead sulfide diffraction lists the main peaks as 26.05° for the (1 1 1) plane, 30.16° for the (2 0 0) plane, 43.12° for the (2 2 0) plan and 51.06° for the (3 1 1) plane and 53.50° for the (2 2 2) plane [85]. In the image above, peaks in the XRD data are labeled with the corresponding reference peak. Each of these peaks differed by less than one half of one degree from the reference values. Peaks characteristic of NaCl were also visible and have been labeled [86], as well as several smaller peaks that could not be identified. These peaks are presumed to result from salt impurities remaining from the growth medium.

2.4 Conclusions

In conclusion, I have successfully synthesized PbS nanoparticles using *Shewanella oneidensis* MR-1. The results of SEM/EDS analysis, combined with the immediate formation of a black precipitate when lead acetate is added and the thiosulfate-dependent absorbance peak in the liquid growth medium, support the theory that *Shewanella* forms hydrogen sulfide gas in solution through thiosulfate reduction, then facilitates a PbS precipitation reaction at the biofilm surface:



Additional work will be required to determine the size and precise morphology of the PbS nanoparticles generated, but XRD results suggest that the nanoparticles possess a highly crystalline structure.

3. CADMIUM SULFIDE BIOSYNTHESIS

3.1 Introduction

In this section we describe the biosynthesis of cadmium sulfide nanoparticles using *Shewanella oneidensis* MR-1. Bulk cadmium sulfide is a semiconductor with a direct band gap of 2.42eV, and is therefore most photosensitive to light with a wavelength around 500 nm, around the middle of the visible light band. In nanoparticulate cadmium sulfide, a larger band gap may appear if quantum confinement effects are present [87]. Due to their photocatalytic properties, cadmium sulfide nanoparticles have a wide range of potential applications, ranging from solar cells [88] to photodetectors, thin-film transistors and biosensors [89]. In addition to its electronic properties, cadmium sulfide is a compound whose production can have environmental benefits since cadmium is a common environmental pollutant in mine sites and some drinking water sources and the formation of CdS causes cadmium to precipitate out of solution and allows it to be removed from the source water [90], [91].

Prior chemical synthesis of CdS nanoparticles has involved a range of chemical methods generally involving the input of heat or electromagnetic radiation [92]. More recent studies have begun to examine the benefits of using bacteria to synthesize CdS nanoparticles, including a study that reported positive results using *Shewanella oneidensis* MR-1. However, this study investigated biosynthesis under only one set of cultivation conditions and did not employ the metal or sulfur-reducing capabilities of *Shewanella* as a part of the synthesis method. Furthermore, the prior study did not attempt to investigate the mechanisms of CdS production or characterize the bacterial biofilms that formed in the growth medium [49].

3.2 Experiment 1: Controlled Thiosulfate Concentration

In this experiment, parallel batch cultures of *Shewanella oneidensis* MR-1 were grown with controlled amounts of thiosulfate. The goal of this experiment was to confirm the formation of cadmium sulfide in the *Shewanella* batch cultures while also observing the effect of varying concentrations of thiosulfate.

3.2.1 Incubation

In this experiment, eight batches of *Shewanella* culture were prepared as described in section 1.3.1, in a phosphate-free medium. The batches were cultivated in 150mL culture bottles with 50mL of liquid in each bottle and nitrogen in the remaining headspace. Sodium thiosulfate added to the medium as an electron acceptor. The media was bubbled with nitrogen for 20 minutes to remove dissolved oxygen and then was autoclaved for 45 minutes at 121°C to achieve sterilization. These bottles consisted of four distinct groups with two identical bottles in each group, as follows:

Table 3: Bottle groups for controlled thiosulfate cadmium sulfide synthesis experiment.

Group A	Added cadmium sulfate to 10mM, sodium thiosulfate to 10mM, and 1 mL inoculum
Group B	Added cadmium sulfate to 10mM, sodium thiosulfate to 20mM, and 1 mL inoculum
Group C	Added cadmium sulfate to 10mM, sodium thiosulfate to 10mM, and no inoculum
Group D	Added cadmium sulfate to 10mM, sodium thiosulfate to 20mM, and no inoculum

Once the bottles had returned to room temperature after autoclaving, the Group A and Group B bottles were injected with 1mL of live *Shewanella* culture prepared in the medium described in Appendix A, then were placed in an incubator and heated to a temperature of 30°C

while also being agitated at 100 rpm. After 24 hours, the cadmium sulfate was added in the form of 0.5mL sterile 1.0M cadmium sulfate solution. Both of the bottles in Group B and one of the bottles in Group A instantaneously began to develop the yellow color characteristic of precipitated cadmium sulfide. The bottles were re-inspected after 14 days. In the three bottles that had developed the yellow coloration, yellow precipitates had now settled to the bottom of the bottles. The other bottles remained transparent with no evidence of CdS precipitates.

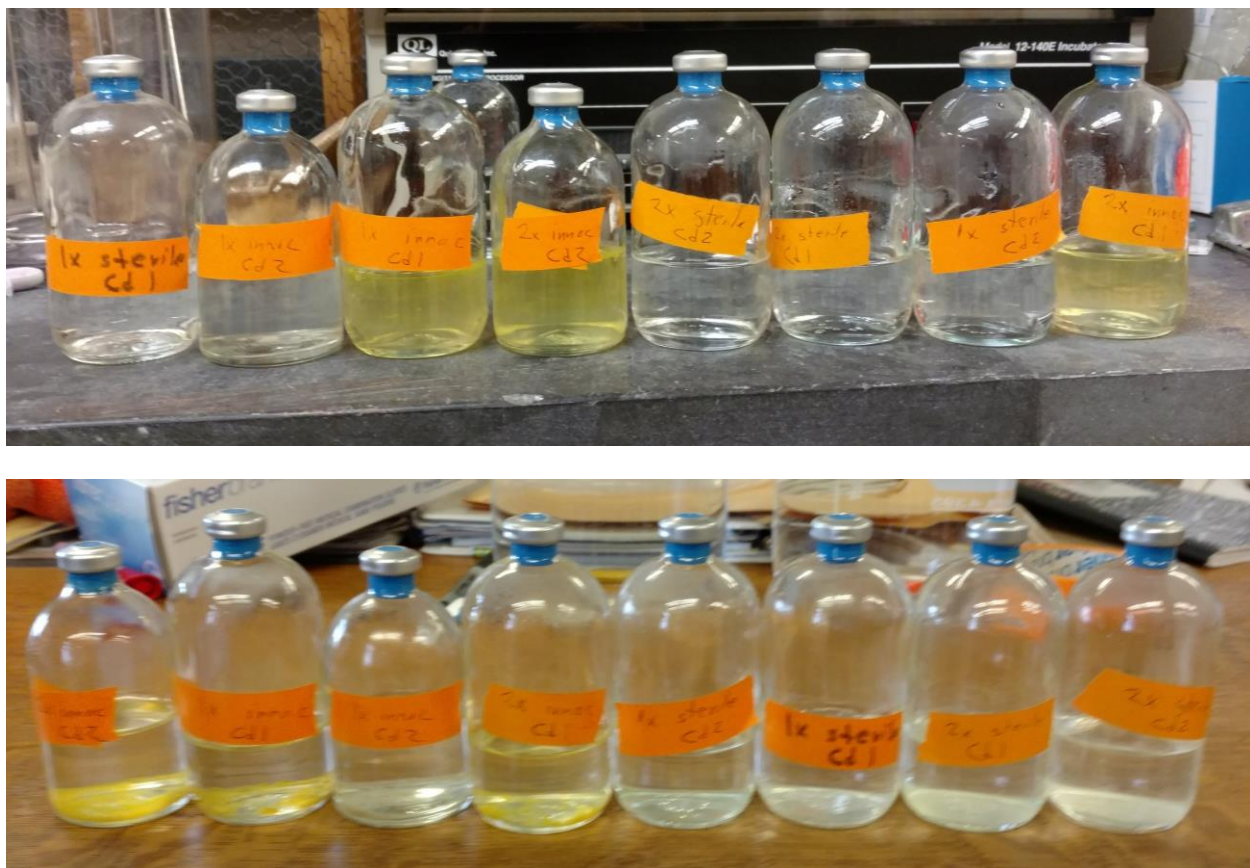


Figure 8: Development of CdS precipitate (top) and settling (bottom).

3.2.2 Characterization Using SEM/EDS

Yellow precipitates were harvested from the cultivation bottles using a sterile needle and applied to a clean silicon slab. SEM images revealed features similar to those seen in the lead-enhanced batches described in Chapter 2, including bacteria, extracellular polysaccharide, and

salt deposits (see Figure 9). Point EDS analysis, shown in Figure 10, revealed 68.20% carbon, 4.93% oxygen, 1.81% sulfur, and 1.44% cadmium by atomic percentage. Meanwhile, SEM performed on the sterile batches from this experiment revealed carbon and oxygen-containing deposits but did not reveal cadmium or sulfur.

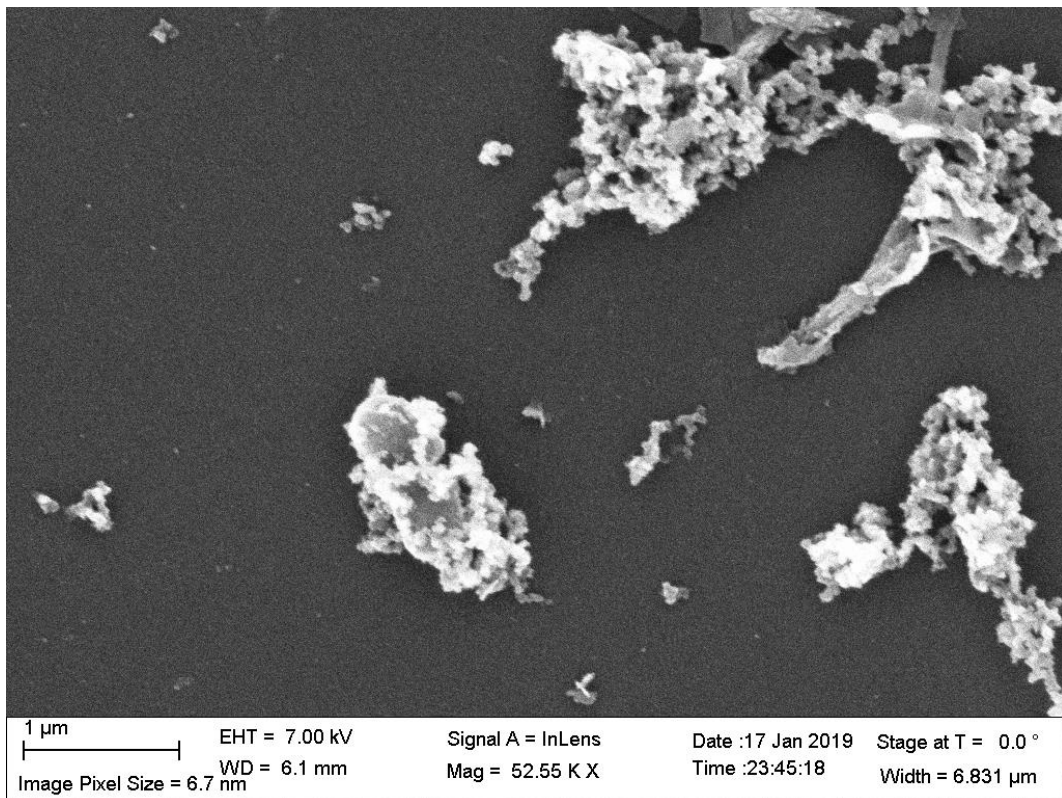


Figure 9: A *Shewanella* bacterium surrounded by nanomaterials.

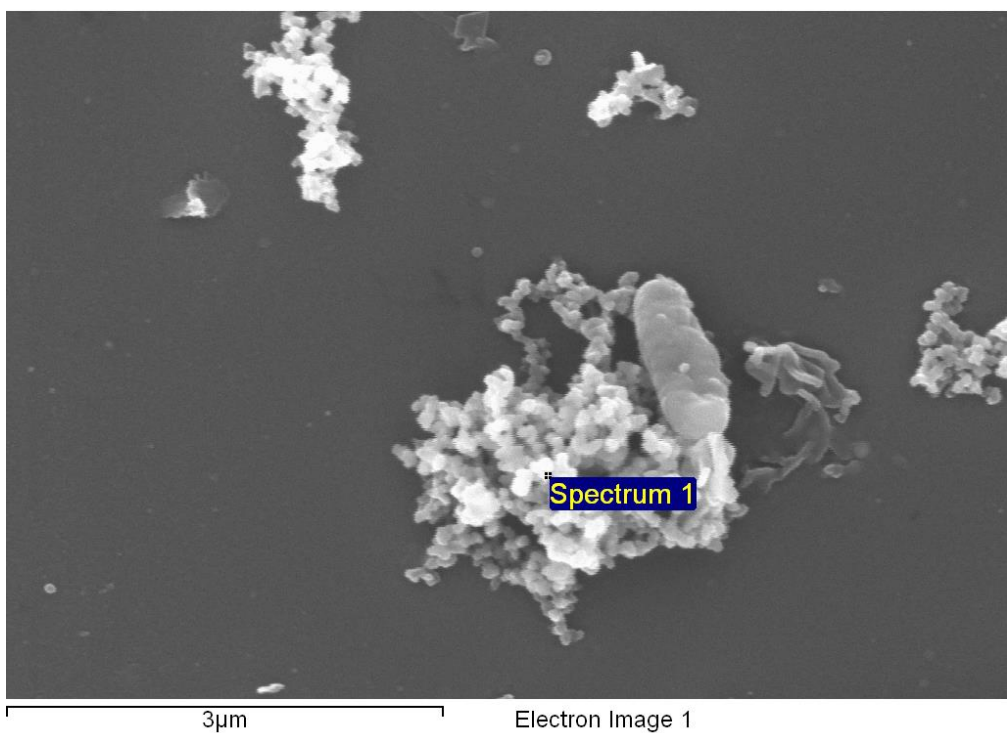


Figure 10: A *Shewanella* bacterium surrounded by nanomaterials.

3.2.3 Characterization Using XRD

Contents of the Group A batches were placed in plastic tubes and centrifuged at 2000 rpm for 30 minutes. The supernatant was discarded and replaced with ethanol. Then the material was placed in a beaker and dried in a 100°C heater overnight. The remaining material was ground into a powder and imaged using the XRD system described in section 1.3.5.

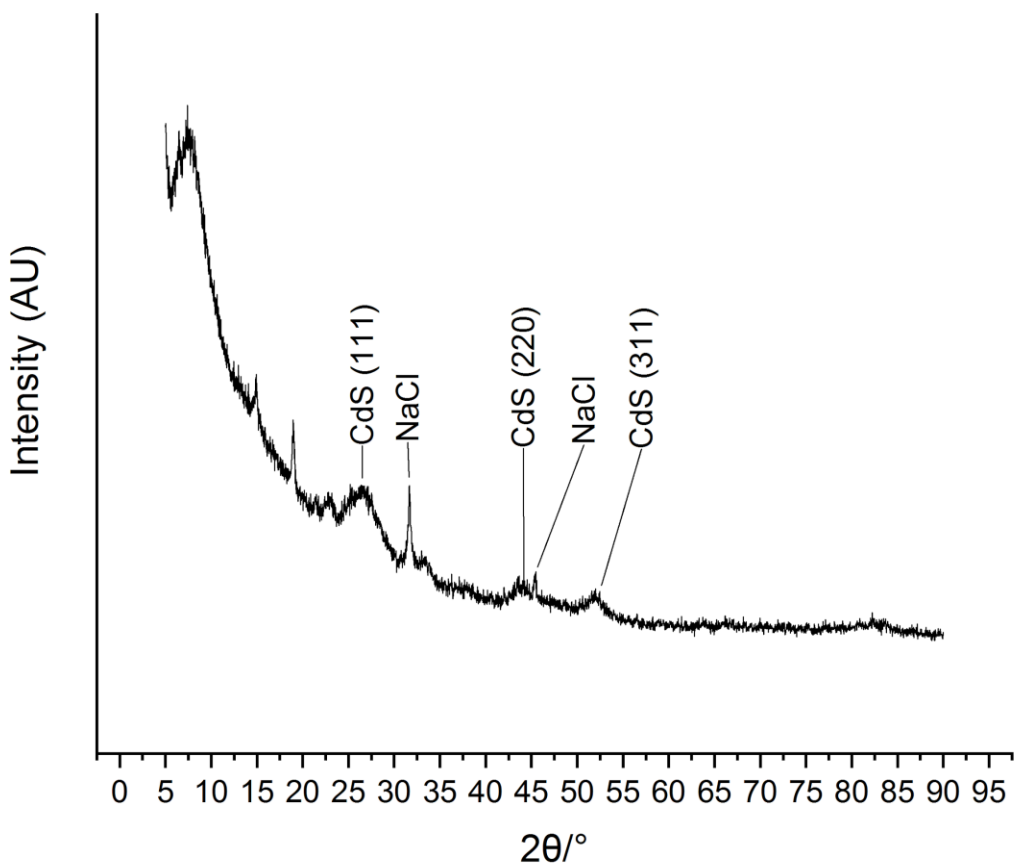


Figure 11: XRD diffractogram indicating CdS diffraction planes and NaCl peaks.

The JCPDS data for cubic cadmium sulfide lists the main XRD diffraction peaks as 26.58° for the (1 1 1) plane, 44.16° for the (2 2 0) plan and 52.39° for the (3 1 1) plane. In the image above, peaks in the XRD data are labeled with the corresponding reference peak and show strong agreement with the reference values [93]. However, the peaks differ from those in the reference data in that they are weaker and broader, a phenomenon that can be likely be attributed to crystal defects or impurities. Peaks characteristic of NaCl were also visible and are labeled in Figure 11 [86]. As in the PbS samples described in Chapter 2, these are presumed to be salt impurities in the growth medium.

3.2.4 Characterization Using Absorption Spectroscopy

Liquid from each of the four cultivation groups A through D was characterized using the UV-Vis absorption spectrometer described in section 1.3.7. First, an empty plastic cuvette containing only air was used as a blank. Next, several milliliters of sample from one of the Group A bottles, the Group B bottle that exhibited CdS precipitation, and one of each of the Group C and Group D bottles were placed in plastic cuvettes and their absorbance was measured compared to that of the plastic cuvette. Bottles were manually agitated prior to removal of liquid in order to re-suspend precipitates that had descended to the bottom of the bottles.

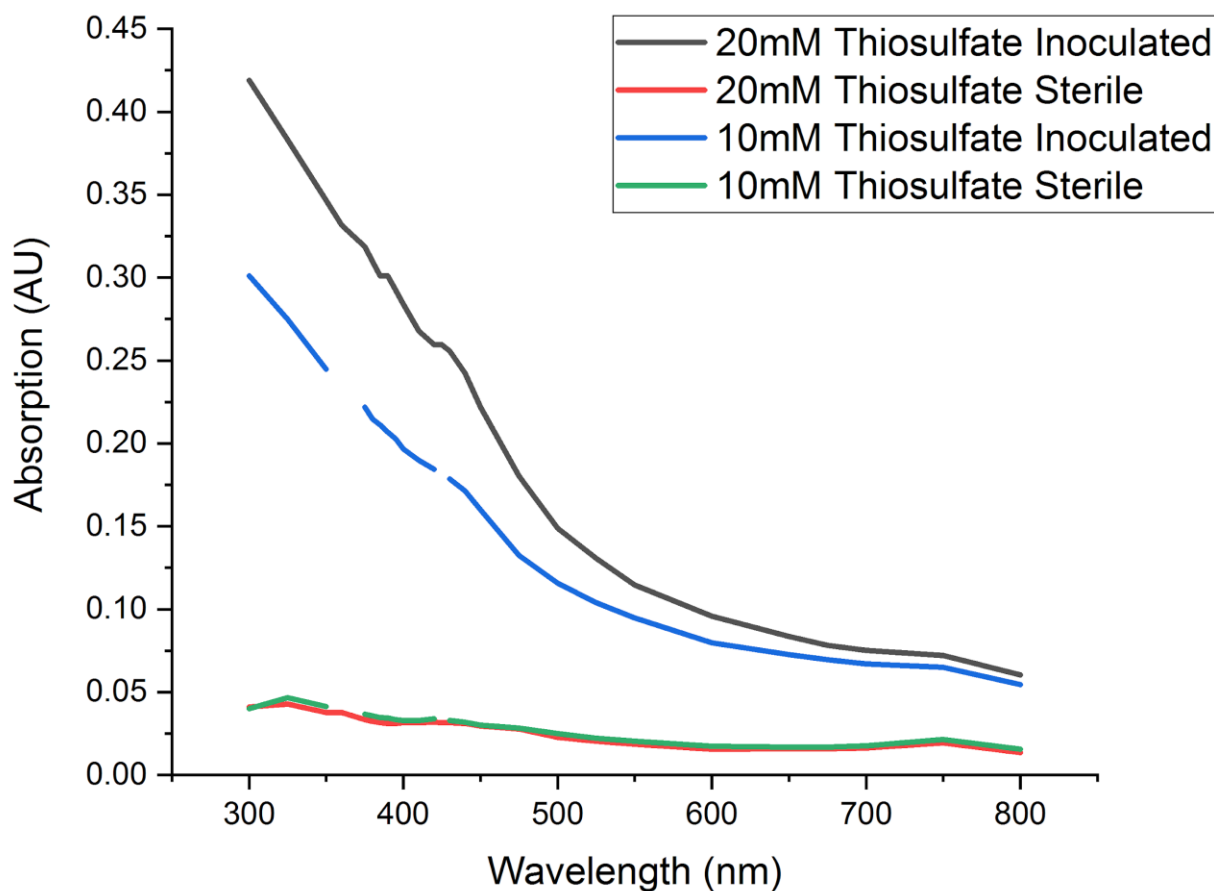


Figure 12: Comparative absorption spectroscopy for CdS samples.

In the inoculated batches, the absorbance appears to increase as the concentration of sodium thiosulfate increases. There is a trend of increasing absorbance at smaller wavelengths

with the steepest increase beginning at approximately 500 nm with a slight absorbance peak at approximately 425-450 nm. This is in agreement with previously reported results with colloidal cadmium sulfide nanoparticles [94]. In the sterile batches, the sodium thiosulfate concentration does not appear to affect the solution absorbance.

3.3 Experiment 2: Controlled Inoculation Methods

In this experiment, parallel batch cultures of *Shewanella oneidensis* MR-1 were grown while varying the state of the *Shewanella* culture in the bottles. The goal of this experiment was to observe how the presence of live or dead *Shewanella* cultures and their metabolic by-products affected the production of cadmium sulfide nanoparticles.

3.3.1 Incubation

Eight batches of 50mL sterile anaerobic *Shewanella* culture were prepared in a phosphate-free medium. Sodium thiosulfate added to the medium as an electron acceptor. The media was bubbled with nitrogen for 20 minutes to remove dissolved oxygen, then were autoclaved for 45 minutes at 121°C to achieve sterilization. These bottles consisted of four distinct groups with two identical bottles in each group, as follows:

Table 4: Bottle groups for varied inoculum CdS synthesis experiment.

Group A	Added 1 mL live inoculum.
Group B	Added 1 mL autoclaved (dead) inoculum.
Group C	Added 1 mL live inoculum, allowed bacteria to grow in medium for 4 days, then autoclaved.
Group D	Added no inoculum.

Once the bottles had returned to room temperature after autoclaving, the Group A, B and C bottles were injected with 1 milliliter of *Shewanella* culture, then were placed in an incubator and heated to a temperature of 30°C while also being agitated at 100 rpm. In the case of Groups A and C, the culture used was still in an active metabolic state. In the case of Group B, the culture had been heat-killed via autoclave prior to injection.



Figure 13: Development of yellow color in inoculated cadmium bottles.

5 days after the inoculation, cadmium sulfate was added to all bottles in the form of 0.5mL 1.0M cadmium sulfate solution. As soon as cadmium sulfate was added, one of the bottles in Group A developed the yellow color characteristic of precipitated cadmium sulfide. One of the bottles in Group C also developed a faint yellow color. The remaining bottles remained transparent with no evidence of CdS precipitates.

3.3.2 Characterization Using SEM/EDS

Yellow precipitates were harvested from the cultivation bottles using a sterile needle and applied to a clean silicon slab, then dehydrated and dried using the same ethanol and HMDS-based method as used in Section 3.3.1. As in the prior cadmium-enhanced medium experiment, SEM images of the bottle that contained visible yellow precipitate revealed bacteria, extracellular polysaccharides, and salt deposits. Point EDS analysis, shown in Figure 14, identified 5.16% cadmium, 4.44% sulfur, 6.87% oxygen and 56.57% carbon by atomic percentage. The bacteria were most obviously present in the Group A bottle with obvious precipitates. In the Group A batch that did not contain visible yellow precipitate, SEM revealed primarily amorphous organic material, presumed to be extracellular polysaccharides or bacterial remnants. For this batch, EDS point analysis showed 3.37% cadmium, 3.30% sulfur, 2.68% oxygen and 14.32% carbon (see Figure 15). Compared to the other bottle in Group A, relatively few intact bacteria were visible. A similar result, with organic material present but relatively few bacteria, appeared in the Group C bottle.

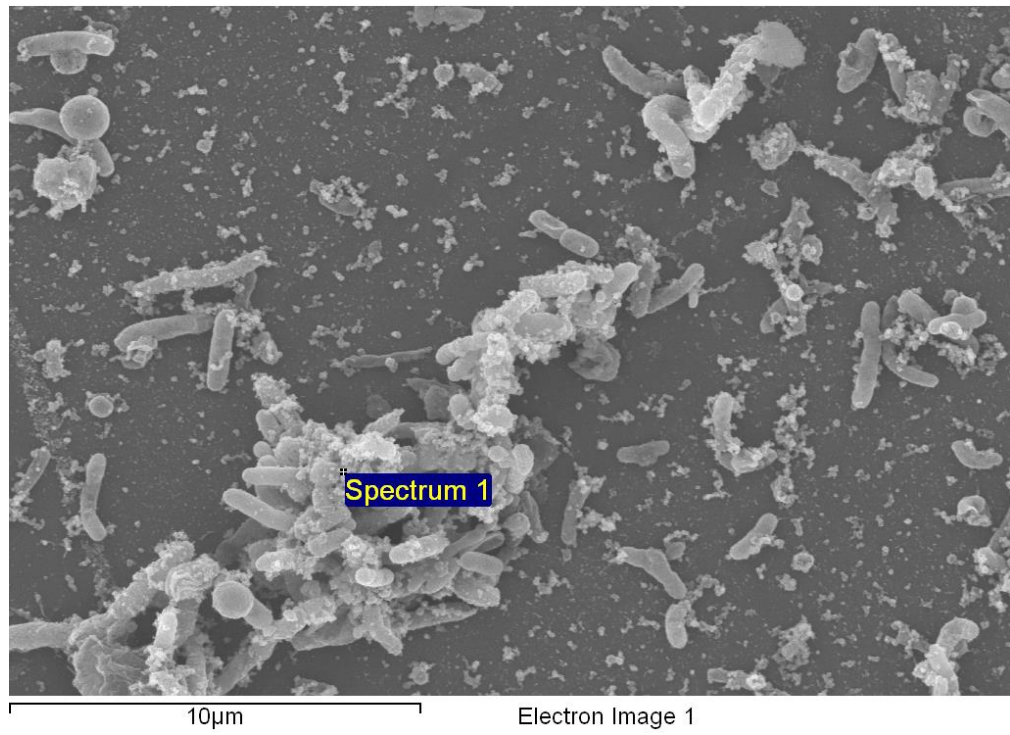


Figure 14: SEM micrograph of the precipitate-containing Group A batch.

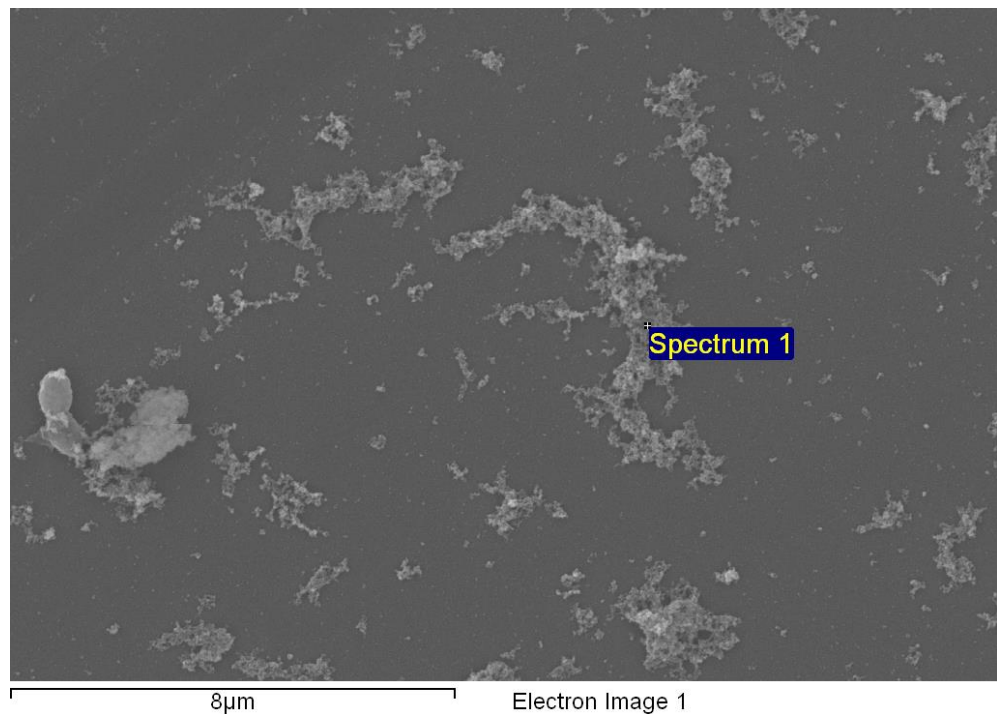


Figure 15: Group A batch without yellow precipitate.

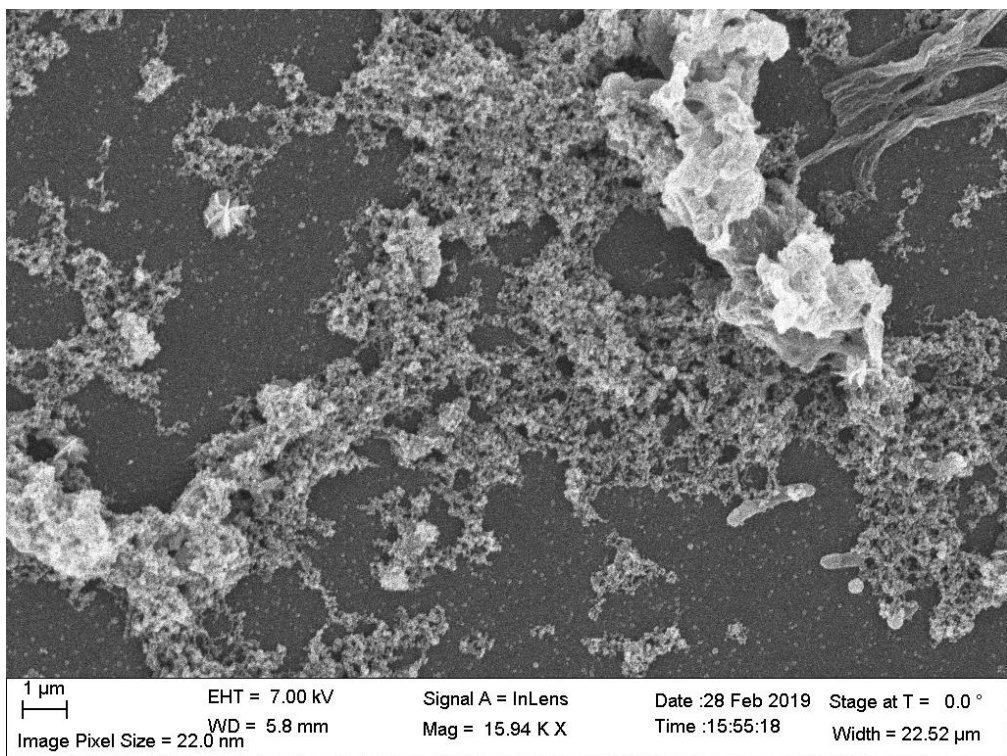


Figure 16: SEM micrograph depicting nanomaterials in the Group C batch.

In addition to evidence of cadmium sulfide precipitation on the bacterial biofilms, the Group A sample with precipitates contained an unanticipated feature that was not seen in any other batch. This sample contained a large number of crystalline spherical microstructures approximately 10 to 30 microns in diameter that appeared to consist primarily of cadmium and oxygen with some carbon present as well. EDS point analysis on one of these structures (see Figure 18) revealed 30.49% cadmium, 3.16% sulfur, 47.97% oxygen and 16.19% carbon by atomic percentage.

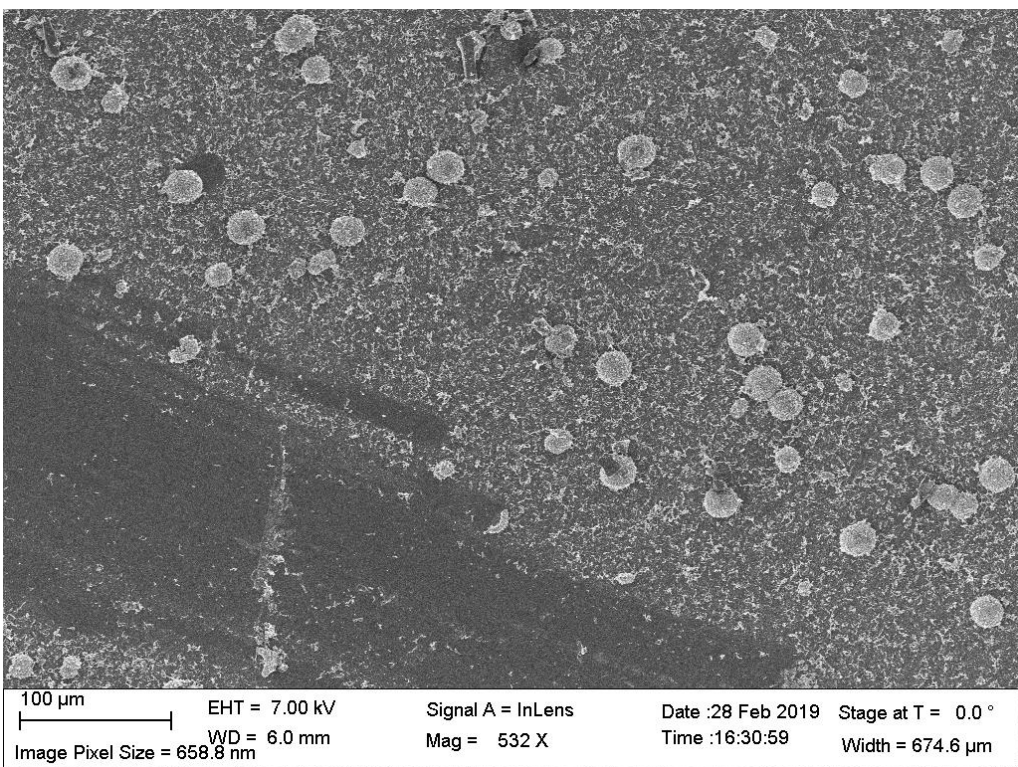


Figure 17: Low-magnification image of cadmium-oxygen-carbon microstructures.

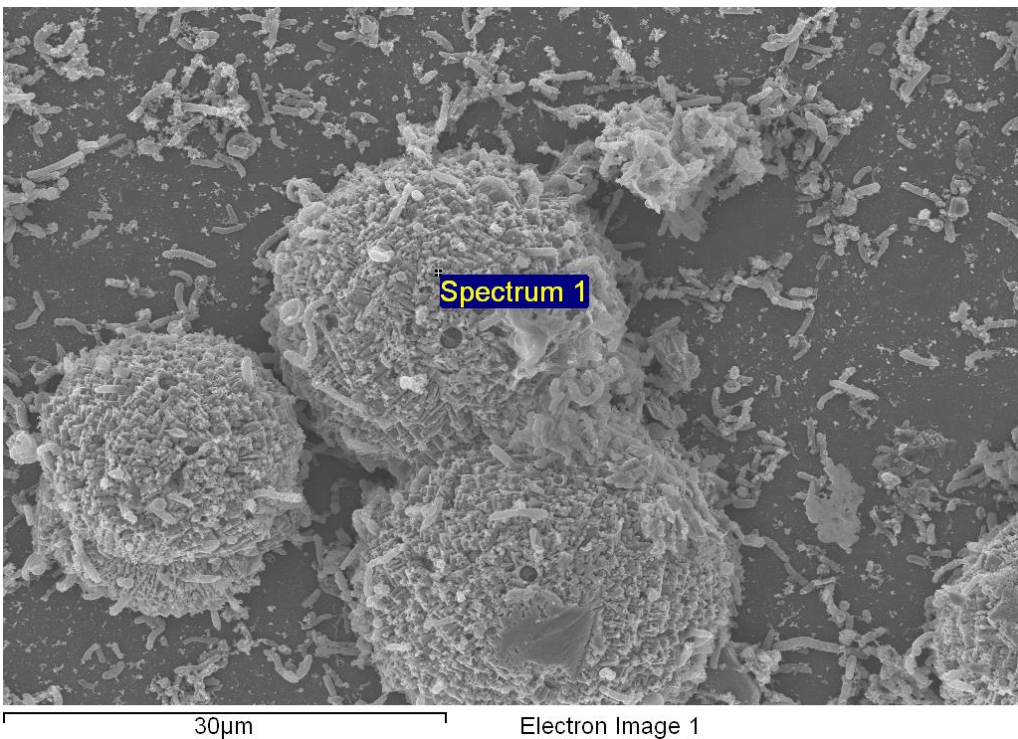


Figure 18: Closeup of several cadmium-oxygen-carbon microstructures.

In several areas of the sample, the microstructures were damaged or degraded, causing their internal structure to become visible to SEM imaging. Images revealed that the

microstructures were hollow and composed of crystal grains generally a few microns in length. The microstructures whose interiors were visible appeared to contain *Shewanella* bacteria with extensive extracellular polysaccharide and nanowire development. In many cases, fibers of organic material extended from the bacteria and coated the interior of the microstructures.

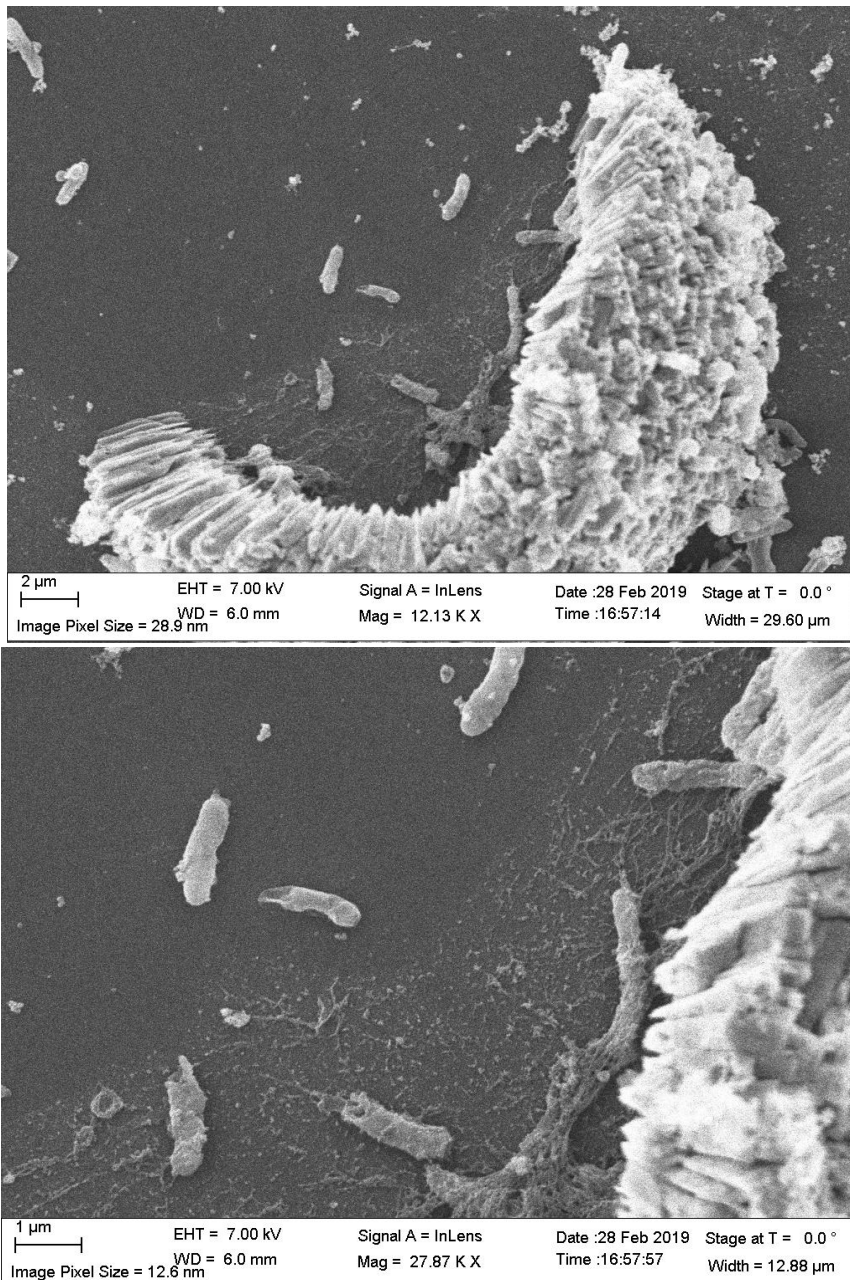


Figure 19: Broken Cd-O-C microstructure with bacterial biofilm inside.

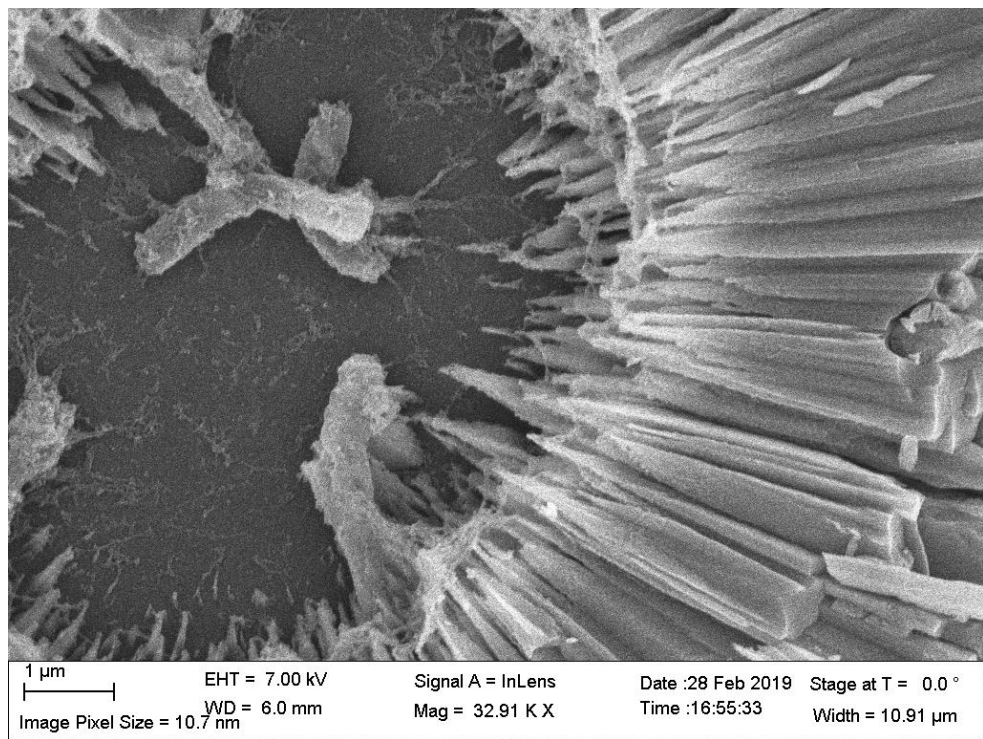


Figure 20: Partially intact Cd-O-C microstructure with biofilm growing on the interior.

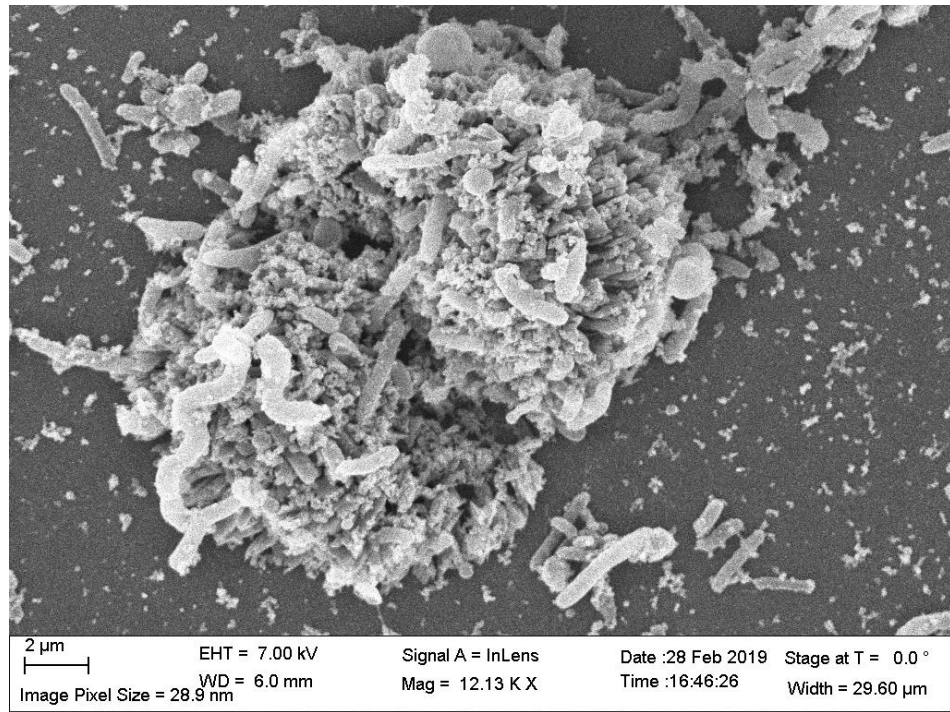


Figure 21: Partially intact Cd-O-C microstructure with bacteria growing on the exterior.

3.4 Conclusions

In the studies described above, I have successfully synthesized CdS nanoparticles using *Shewanella oneidensis* MR-1. The results of SEM/EDS analysis, combined with the immediate formation of yellow precipitate when cadmium sulfate is added and the thiosulfate-dependent absorbance peak of the liquid growth medium, support the theory that *Shewanella* forms hydrogen sulfide gas in solution through thiosulfate reduction, then facilitates a CdS precipitation reaction at the biofilm surface:



Furthermore, the comparative study of *Shewanella* CdS precipitation using varied inoculum states indicates that live *Shewanella* bacteria are required in order for the room-temperature synthesis of CdS to occur in the selected growth medium. XRD results indicated that the material has broad XRD peaks, possibly indicating poor crystallinity or the presence of impurities in the crystals.

Additionally, results from SEM analysis of the CdS precipitate samples also indicate the formation of novel composite microstructures approximately 10 to 30 microns in diameter. These structures appear to be both crystalline and hollow and appear to have formed around colonies of *Shewanella* bacteria. Elemental EDS analysis indicates that the microstructures are composed primarily of cadmium, oxygen and carbon. Furthermore, the topography of bacterial biofilms inside these structures differs visually from the topography outside them, suggesting that they contain a micro-environment in which the aqueous chemistry differs from that outside the structures.

Additional work will be required to establish the conditions under which such structures form, the electronic and compositional attributes of the structures, and the mechanisms under which the bacteria and chemistry of the medium trigger the structures' formation.

4. MOLYBDENUM DISULFIDE BIOSYNTHESIS

4.1 Introduction

Molybdenum disulfide is a transition metal dichalcogenide, meaning that each molecule contains two sulfur atoms. It occurs naturally as molybdenite, which is the most common naturally-occurring ore of molybdenum. Unlike the materials synthesized in earlier chapters, molybdenum disulfide is commonly found in several different morphologies. The most stable and common of these is the hexagonal form; however, there also exist others such as the rhombohedral [95] and trigonal [96] and these different structures also exhibit differences in their electronic band gaps.

The tendency of the common forms of this material is to form layers that bind weakly to one another via van der Walls forces. This weak bonding between layers makes the material soft, slippery, and effective as a dry lubricant. It also leads to additional electronic properties. Molybdenum disulfide is comparable to graphene in its surface functionalizability, and unlike graphene possesses a well-defined band gap, making it more useful than graphene for many switching applications [97],[98].

In their nanoparticulate form, molybdenum disulfide nanoflakes, like other semiconductor nanoparticles, offer tunable electronic properties. However, in molybdenum disulfide, these effects are further complemented by the ability to functionalize the material's surface, or cause it to form bonds with other materials. This functionalization provides a simple method of changing the molybdenum disulfide's surface reactivity, adding additional electrons or holes, or creating a direct interface between the material and a number of redox-active compounds. This greatly extends the ability of molybdenum disulfide to be used in electrochemical or bioactive sensing technologies [99] Preparing molybdenum disulfide in its commonly-used forms usually involves a chemical synthesis route. This is most often done using molybdenum compounds and hydrogen sulfide gas at high temperatures [100].

Some prior work has been published on the production of MoS₂ compounds using bacteria. In one study, synthesis of MoS₂ using bacteria of the *Desulfovibrio* genus, which appeared to reduce Mo(VI) to Mo(IV) in solution [101]. A range of other bacteria are also reportedly capable to reducing Mo(VI) to Mo(V), though the study reporting this funding did not detect the formation of Mo(IV) or MoS₂ [102].

4.2 Experiment 1: Controlled Thiosulfate Concentration

4.2.1 Incubation

In this experiment, eight bottles containing 50 mL of media each were prepared using the standard *Shewanella* medium and sodium thiosulfate added to the medium as an electron acceptor. These bottles consisted for four distinct groups with two identical bottles in each group, as follows:

Table 5: Bottle groups for the controlled thiosulfate MoS₂ synthesis experiment.

Group A	Added molybdenum trioxide to 10mM, sodium thiosulfate to 10 mM, and 1 mL inoculum
Group B	Added molybdenum trioxide to 10mM, sodium thiosulfate to 20 mM, and 1 mL inoculum
Group C	Added molybdenum trioxide to 10mM, sodium thiosulfate to 10 mM, and no inoculum
Group D	Added molybdenum trioxide to 10mM, sodium thiosulfate to 20 mM, and no inoculum

Once the bottles had returned to room temperature after autoclaving, the Group A and Group B bottles were injected with 1mL of live *Shewanella* culture. Molybdenum trioxide (MoO₃), which is minimally soluble in water at room temperature, was prepared as a suspension of approximately 25% molybdenum trioxide powder and 75% ultrapure water by volume. 0.5 milliliters of this suspension were then added to each bottle. The bottles were then allowed to incubate for 14 days. At the end of 14 days, the added molybdenum oxide had dissolved, and the inoculated bottles had developed an orange-red coloration that did not visibly settle to the bottom of the bottles as precipitate. A gelatinous black material, presumed to be nanomaterial-laden *Shewanella* biofilm, could also be seen in the bottom of the inoculated bottles. The sterile bottles remained transparent with no evidence of precipitates or coloration.



Figure 22: The development of orange color in the inoculated bottles.

4.2.2 Characterization Using SEM/EDS

Samples were prepared for SEM imaging using the ethanol/HMDS dehydration and drying method. SEM images revealed bacteria surrounded by clusters of nanomaterials much less than 1 μm in diameter, as well as dense bacterial nanowire networks. EDS analysis of the Group B batch nanomaterials (Figure 26) revealed 81.49% carbon, 11.21% oxygen, 2.41% sulfur and 1.01% molybdenum by atomic percentage. Meanwhile, SEM performed on the sterile batches from this experiment revealed clusters of material on the length scale of several microns.

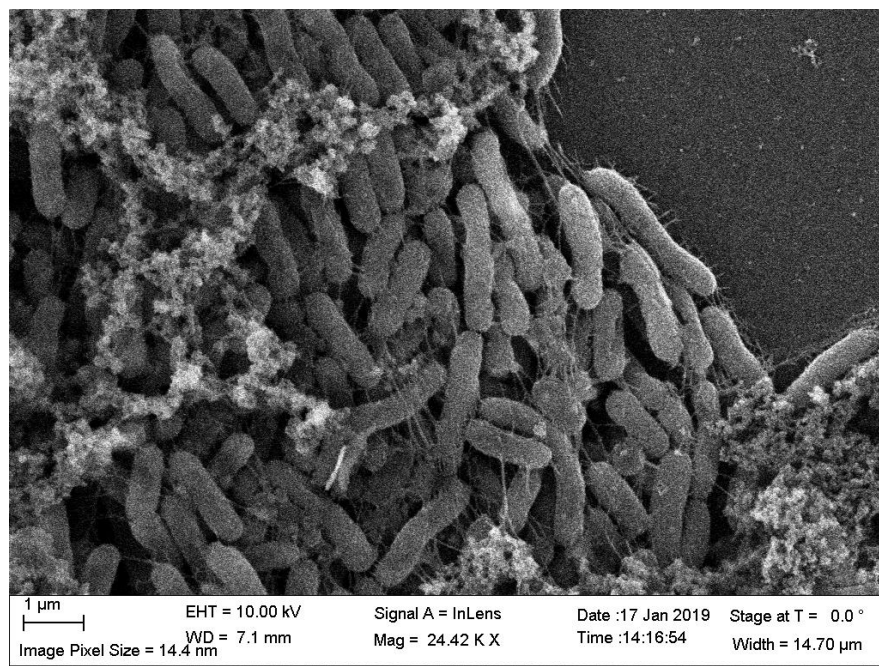


Figure 23: Biofilm development in Group B.

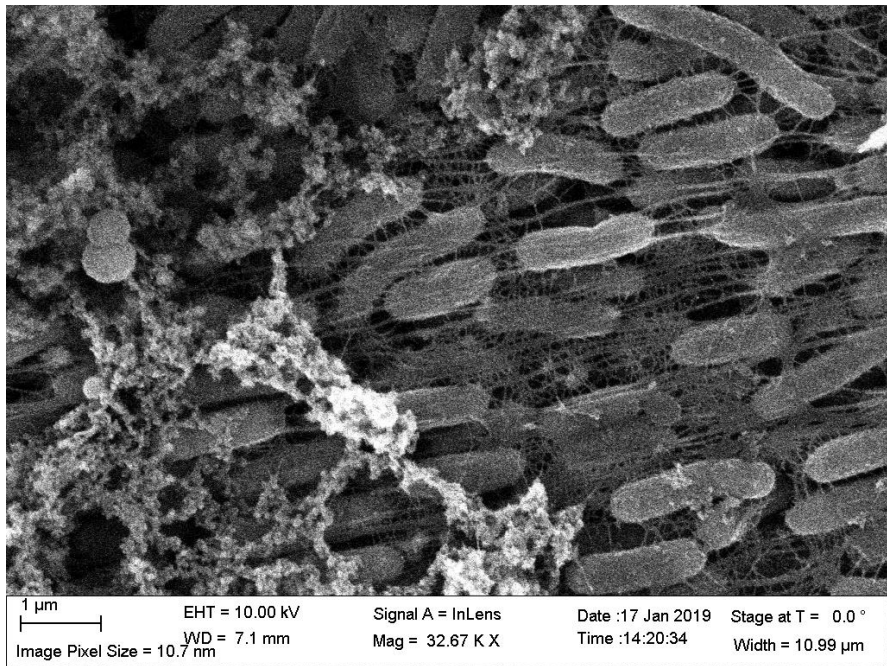


Figure 24: Biofilm development in Group B.

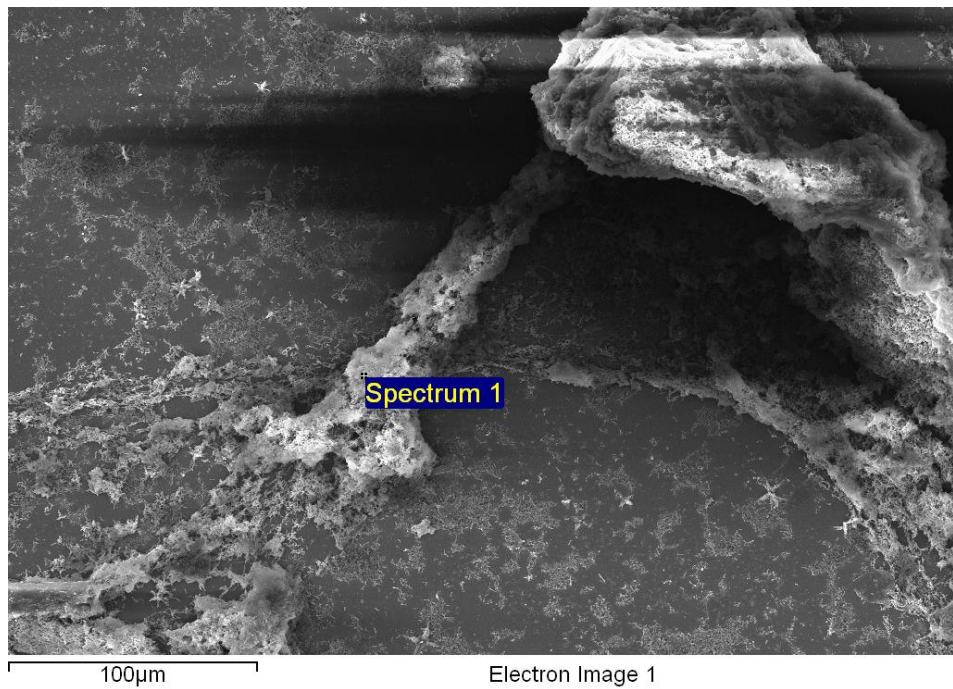


Figure 25: Site of EDS point analysis, showing biofilm growth.

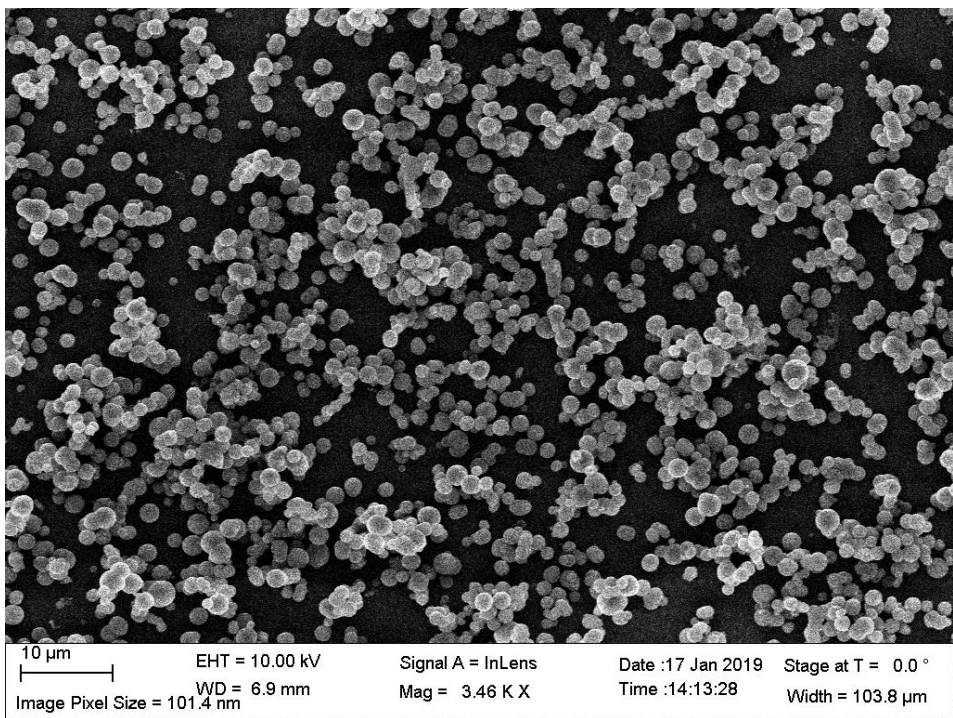


Figure 26: SEM micrograph of the Group D batch reveals organic deposits.

4.2.3 Characterization Using TEM

While the samples were being prepared for SEM analysis, a nanomaterial-laden solution of 33% ethanol and 66% HMDS was flushed from the sample holders and replaced with 100% HMDS, then the solution was set aside. Ted Pella lacey carbon TEM grids were procured and submerged in the solution from Group B. The grid was then imaged using the TEM described in section 1.3.4.

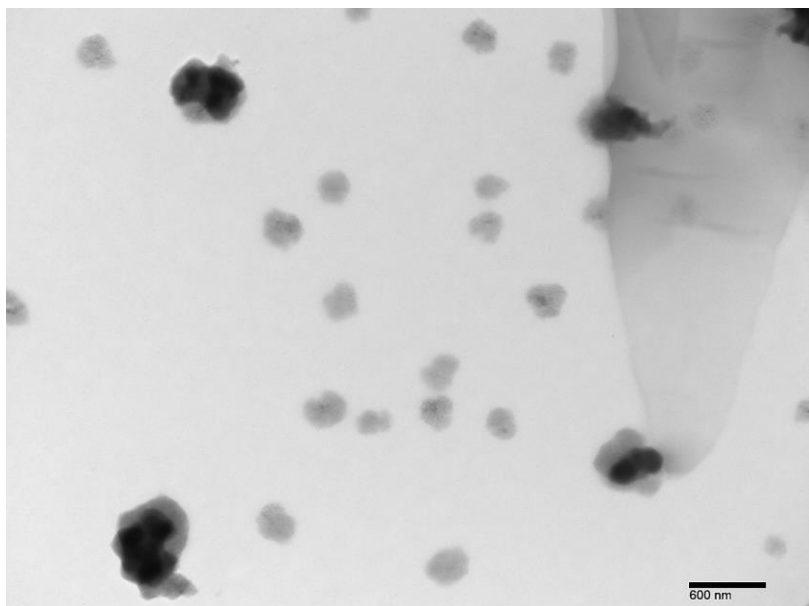


Figure 27: Nanoparticles in the Group B molybdenum sample.

Images generated using TEM imaging mode revealed nanoparticles on a length scale of approximately 50-200 nm. These included both individual crystals and aggregates that appeared to consist of several crystals. Aside from nanoparticles, several other structures were seen, including angular crystalline micron-scale structures (presumed to be salt precipitates from the growth medium) and elongated transparent structures presumed to be of biological origin due to their permeability to the TEM beam.

Diffraction analysis of the nanoparticles revealed that they had a well-defined diffraction pattern, indicating a crystalline nature. This contrasted with the elongated transparent structures described above, which lacked a diffraction pattern. Although calibration issues with the instrument prevented precise analysis of the observed diffraction patterns, a comparison of an individual crystal and a crystal aggregate showed differing patterns, with the polycrystalline aggregate exhibiting a more complex diffraction pattern characteristic of multiple overlaid

diffraction patterns. These results further support the characterization of the aggregates as polycrystalline.

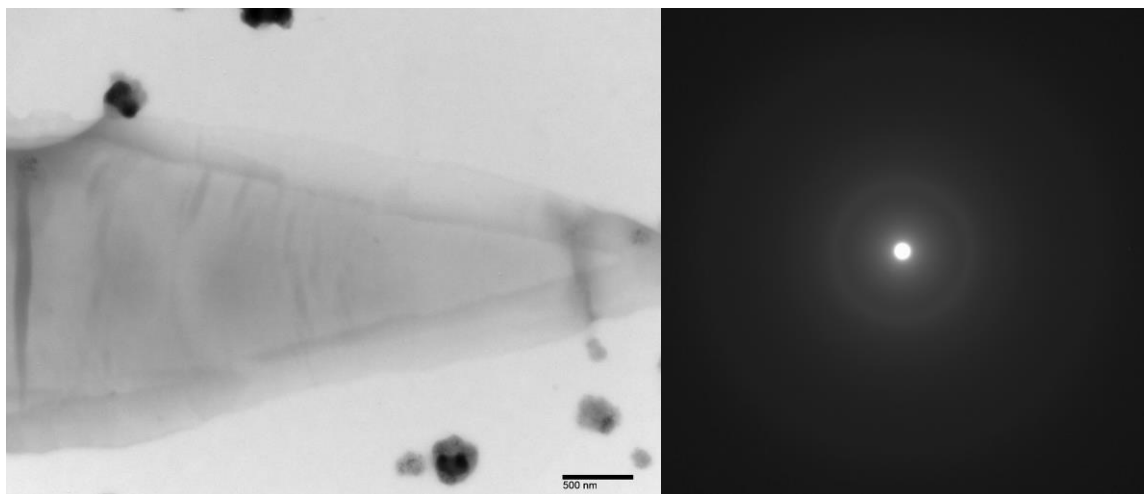


Figure 28: Presumed organic material (left) and its diffraction pattern (right).

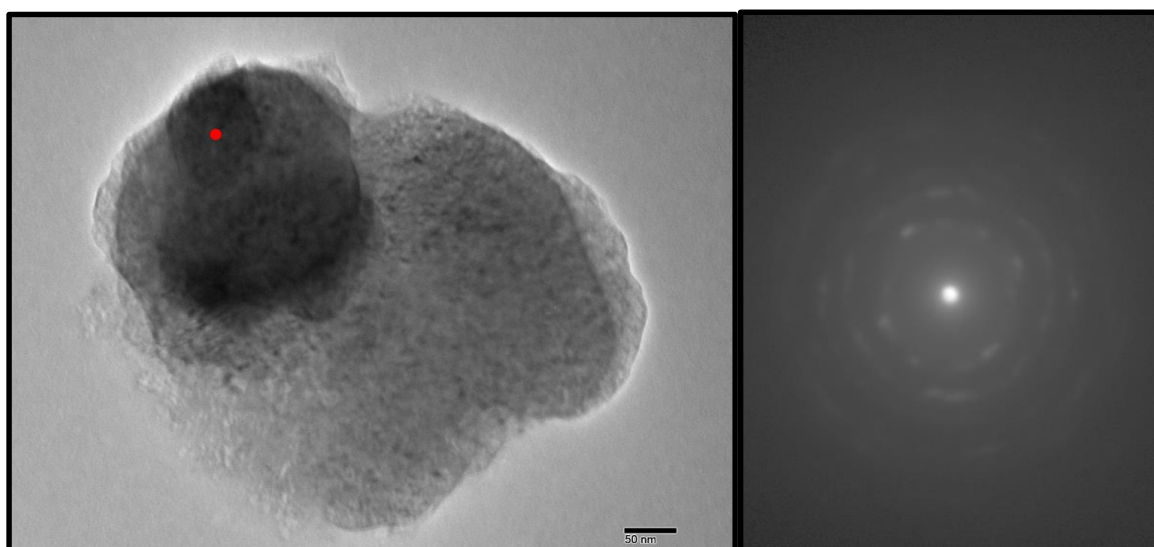


Figure 29: A polycrystal (left) and its diffraction pattern (right).

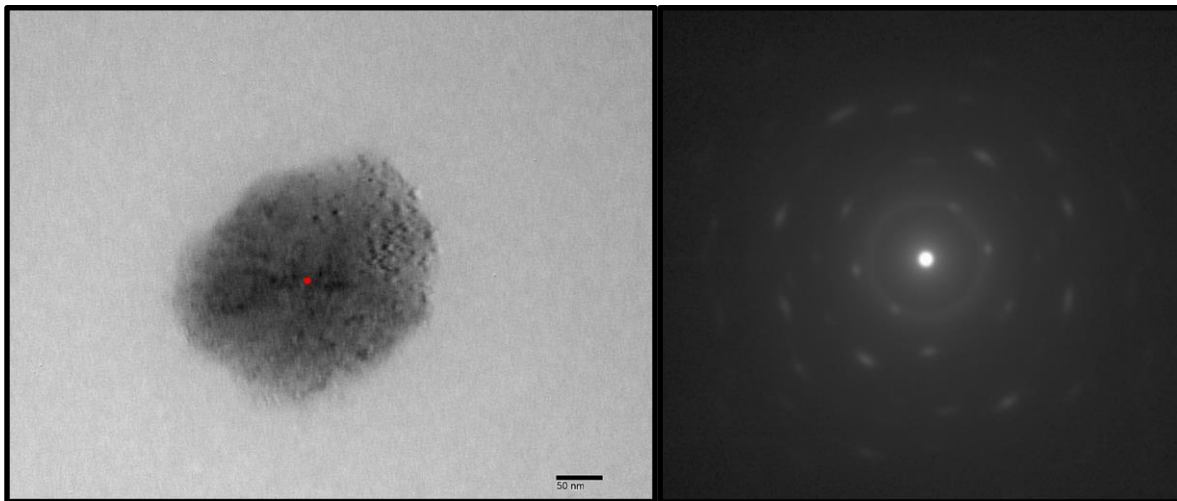


Figure 30: A single crystal (left) and its diffraction pattern (right).

4.2.4 Characterization Using Absorption Spectroscopy

Samples were characterized using the UV-Vis absorption spectrometer described in section 1.3.8. First, an empty plastic cuvette containing only air was used as a blank. Next, several milliliters of sample from each bottle group were placed in plastic cuvettes and their absorbance was measured compared to that of the plastic cuvette.

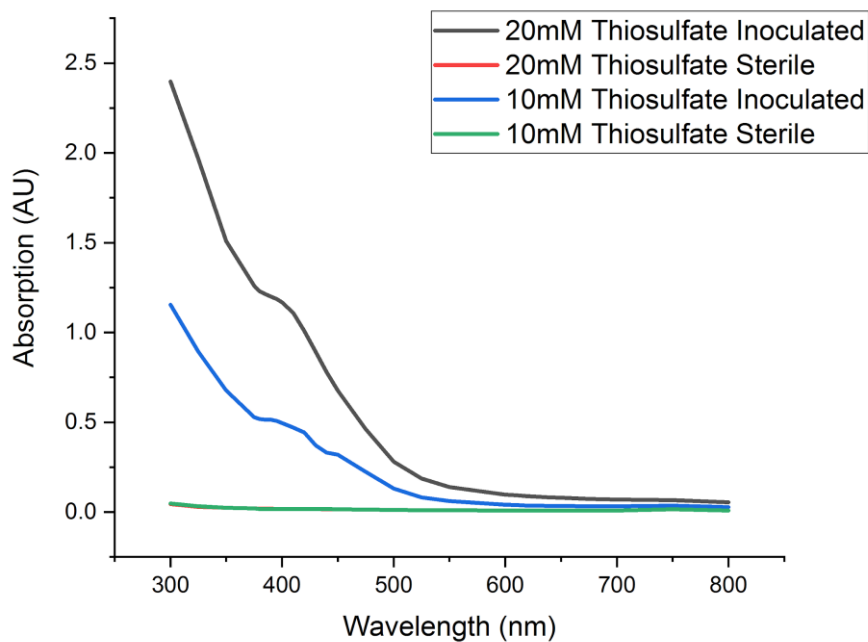


Figure 31: Absorbance peaks for the molybdenum batches.

The figure above shows the absorbance data for all four samples. The inoculated batches exhibited high absorbance at lower wavelengths (beginning at approximately 500 nm) and very low absorbance at higher wavelengths, with a faint absorbance peak at approximately 425 nm. This is in agreement with prior reported absorbance peaks for randomly-stacked colloidal molybdenum sulfide nanoflakes [103]. In the inoculated batches, the absorbance coefficient appeared to depend on the concentration of sodium thiosulfate added to the batch, with the Group B (20 mM) batches exhibiting approximately twice as much absorbance as the Group A (10 mM) batches. Meanwhile, the sterile batches had little to no absorbance and no thiosulfate-dependent behavior.

4.2.5 Characterization Using XRD

Samples from Group A and Group B centrifuged at 2000 rpm for 30 minutes in order to isolate nanoparticles from the supernatant, but centrifugation did not produce a visible change in the sample, suggesting the possibility that the orange color in the solution was the result of suspended nanoparticles too small to be separated via centrifugation. All molybdenum samples were then dried without discarding any supernatant. Liquid from each of the bottles selected for testing was placed in a beaker and heated overnight in a 100°C furnace. The dry material remaining after heating was then ground into powder and analyzed using XRD.

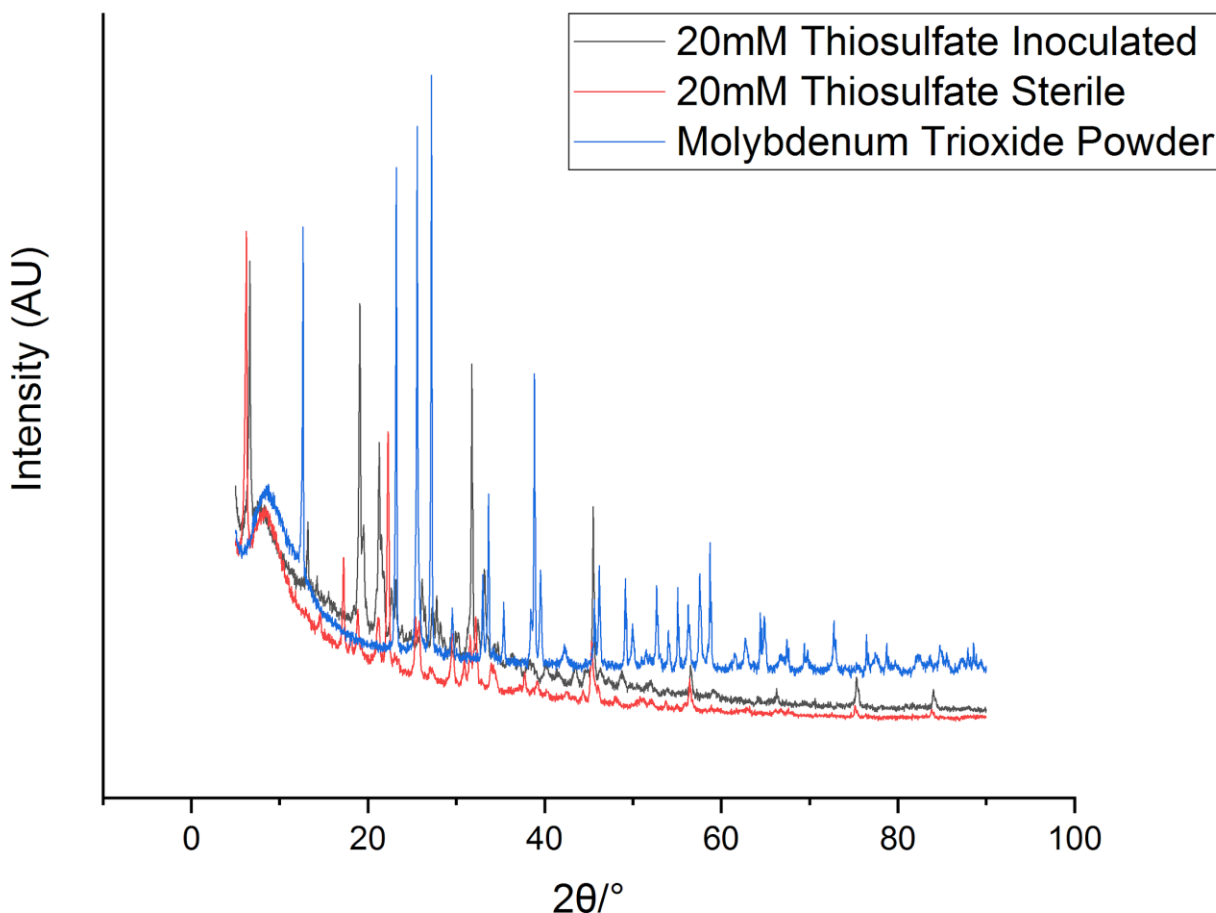


Figure 32: Comparative XRD diffractogram of molybdenum samples.

The figure above compares three XRD diffractograms: those of the Group B inoculated and Group D sterile batches and dry molybdenum oxide powder identical to the powder added to the incubation media. Because the samples were dried without removing supernatant, the diffractogram contained a large number of peaks, many of which likely correspond to buffer salts or other materials added to the media. Since the experimentally-generated diffractograms could not be compared to the diffractograms of individual reference compounds due to the peak density, individual sections of the diffractograms have been examined using literature values for molybdenum disulfide diffraction peaks as a reference. In prior literature describing the crystallography of molybdenum disulfide, more than one crystal structure is noted, giving rise to more than one characteristic XRD pattern.

The most common crystal structure for molybdenum disulfide is the hexagonal structure, and the JCPDS database describes several key peaks for MoS₂ with this structure - one at 14.4° (0 0 2), and another at 33.3° (1 0 0) [104]. Krishan et. al. cite their study of the synthesis of nanocrystalline MoS₂ in the rhombohedral form, finding peaks of 13.69° (0 0 2) peak, 32.85° (1 0 1), 35.61° (0 1 2) and 57.55° (1 1 0) [105]. Li et al. described nanoparticles with hexagonal crystal structure and randomly-stacked layers, which exhibited the (0 0 2), (1 0 0) and (1 1 0) peaks of bulk hexagonal molybdenum disulfide but had broader peaks as compared with the bulk material [103].

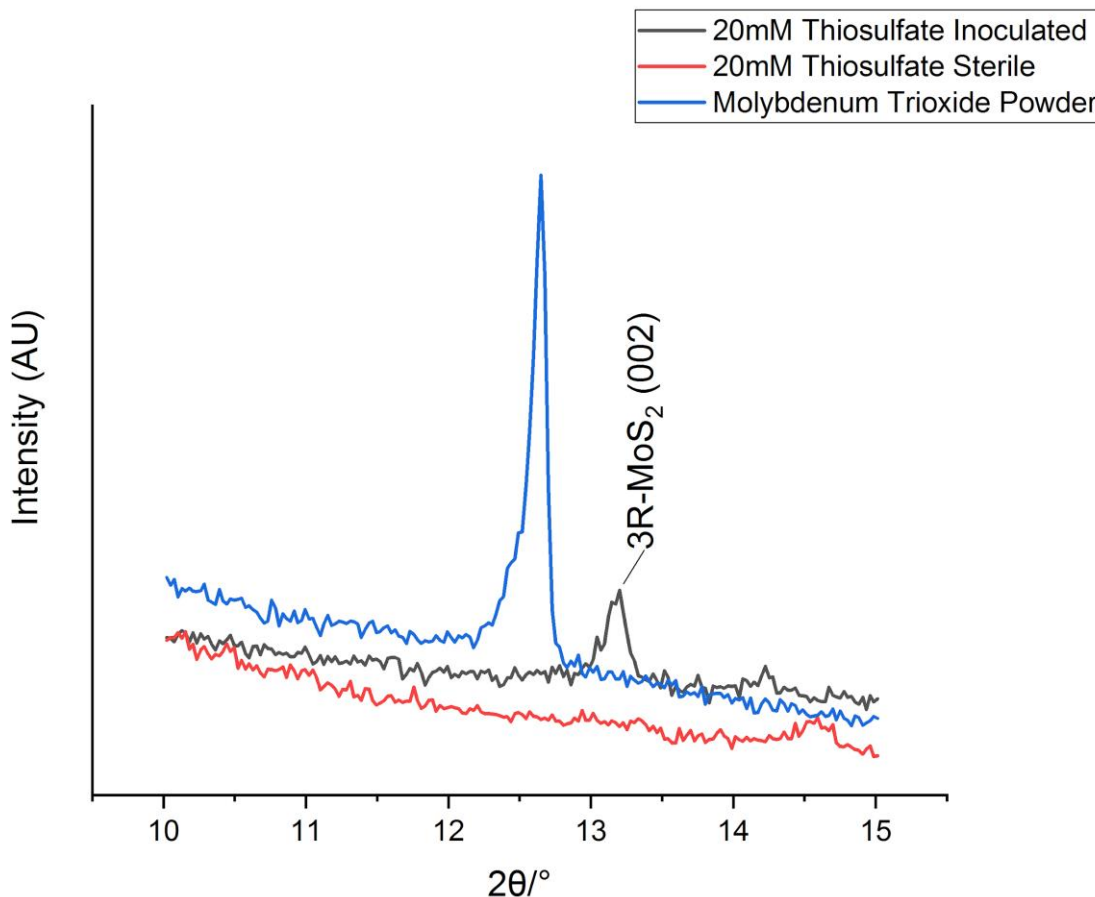


Figure 33: Comparison of the diffractogram peaks from 10-15°.

In the figure above, the diffractogram of the inoculated bottle exhibited a peak at 13.2° that was not visible in the sterile batch or molybdenum trioxide powder. This peak is consistent with the (0 0 2) peak for rhombohedral molybdenum disulfide [104].

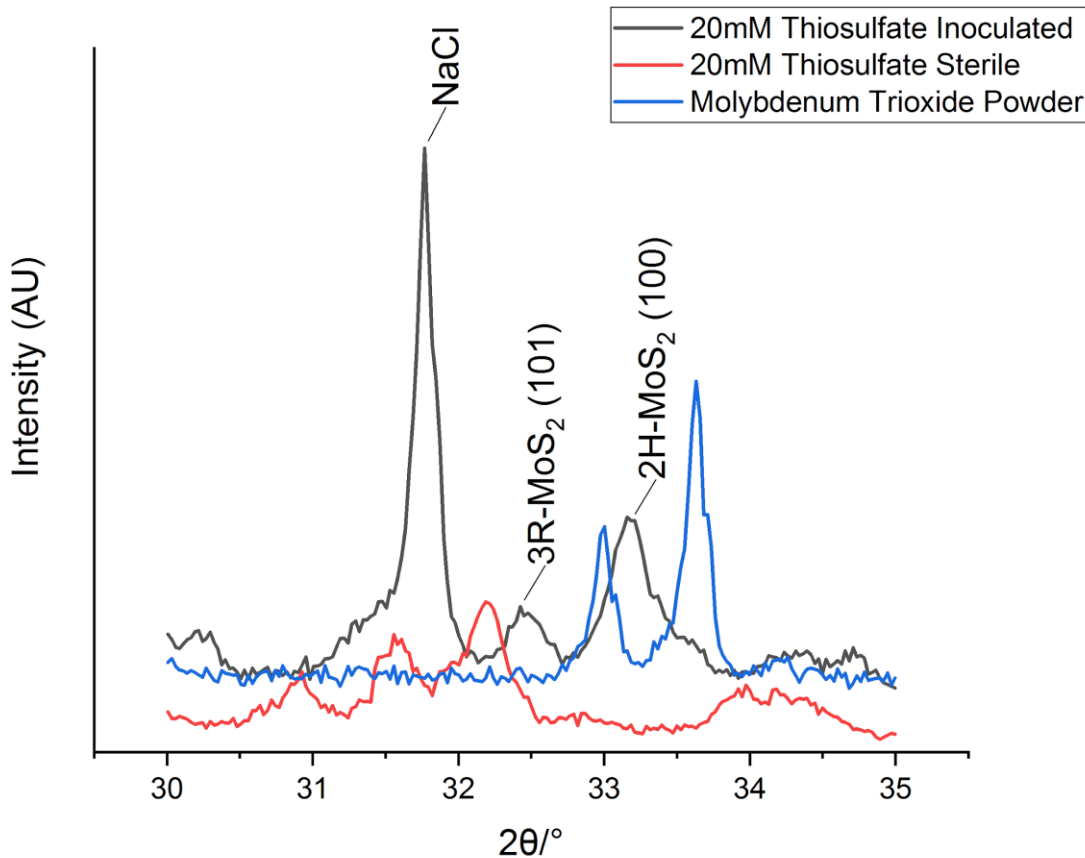


Figure 34: Comparison of the diffractogram peaks from 30-35°.

The inoculated bottle diffractogram also exhibited peaks at 32.5° and 33.2° consistent with the MoS₂ rhombohedral (1 0 1) peak and hexagonal (1 0 0) peak, respectively [104], [105]. The sterile batch and molybdenum trioxide reference sample did not exhibit the same peaks. The peak located between 31° and 32° is consistent with sodium chloride [86].

4.2.6 Characterization Using Raman Spectroscopy

Three different preparations from the inoculated molybdenum batches were analyzed using the Raman spectrometer described in section 1.3.8. First, the same dry powder sample used for SEM analysis in section 4.2.5 was analyzed. Second, liquid from Group B was analyzed after being extracted from the incubation medium using a sterile needle and placed in a cuvette.

Both samples exhibited no discernible Raman peaks aside from those generated by the sample holders.

Next, the black biofilm at the bottom of the Group B cultivation bottle was extracted using a sterile needle and allowed to dry on a glass microscope slide overnight. Raman analysis of this sample was performed using a series of 10 averaged laser pulses, each with a 100 second exposure time. Analysis revealed Raman peaks at 375 cm^{-1} and 400 cm^{-1} , in good agreement with reference values for molybdenum disulfide [106].

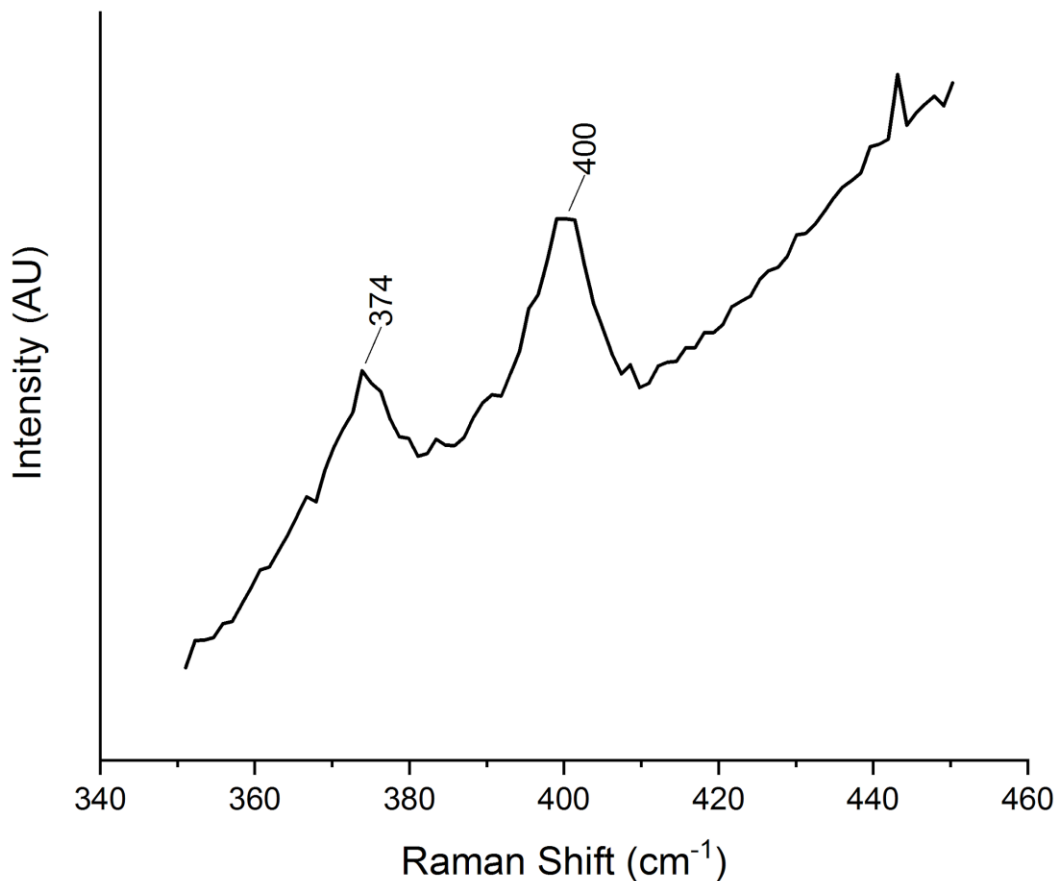


Figure 35: Raman spectrograph of the black biofilm harvested from the Group B batch.

4.3 Experiment 2: Controlled Molybdenum Concentration

4.3.1 Incubation

In this experiment, eight bottles containing 50 mL of media each were prepared as described above, but with the addition of sodium thiosulfate added to the medium as an electron acceptor. These bottles consisted of four distinct groups with two identical bottles in each group, as follows:



Figure 36: The development of blue color in the inoculated bottles.

Table 6: Bottle groups for the controlled molybdenum MoS₂ synthesis experiment.

Group A	1mL molybdenum trioxide suspension added and 1 mL inoculum
Bottle B	0.5 mL molybdenum trioxide suspension added and 1 mL inoculum
Bottle C	1 mL molybdenum trioxide suspension added and no inoculum
Bottle D	0.5 mL molybdenum trioxide suspension added and no inoculum

Once the bottles had returned to room temperature after autoclaving, the Group A and Group B bottles were injected with 1 mL of live *Shewanella* culture prepared in the medium described in Appendix A. Molybdenum trioxide, which is minimally soluble in water at room temperature, was prepared as a suspension of approximately 25% molybdenum trioxide powder and 75% ultrapure water by volume. 1 mL of this suspension was then added to the Group A and

C bottles while 0.5 mL of the suspension was added to the Group B and D bottles. Within one day, the inoculated Group A and B bottles had developed a deep blue coloration. A fainter blue color had also developed in the Group C bottle.

4.3.2 Characterization Using Absorption Spectroscopy

Samples were characterized using the UV-Vis absorption spectrometry. First, an empty plastic cuvette containing only air was used as a blank. Next, several milliliters of sample from each bottle group were placed in plastic cuvettes and their absorbance was measured compared to that of the plastic cuvette.

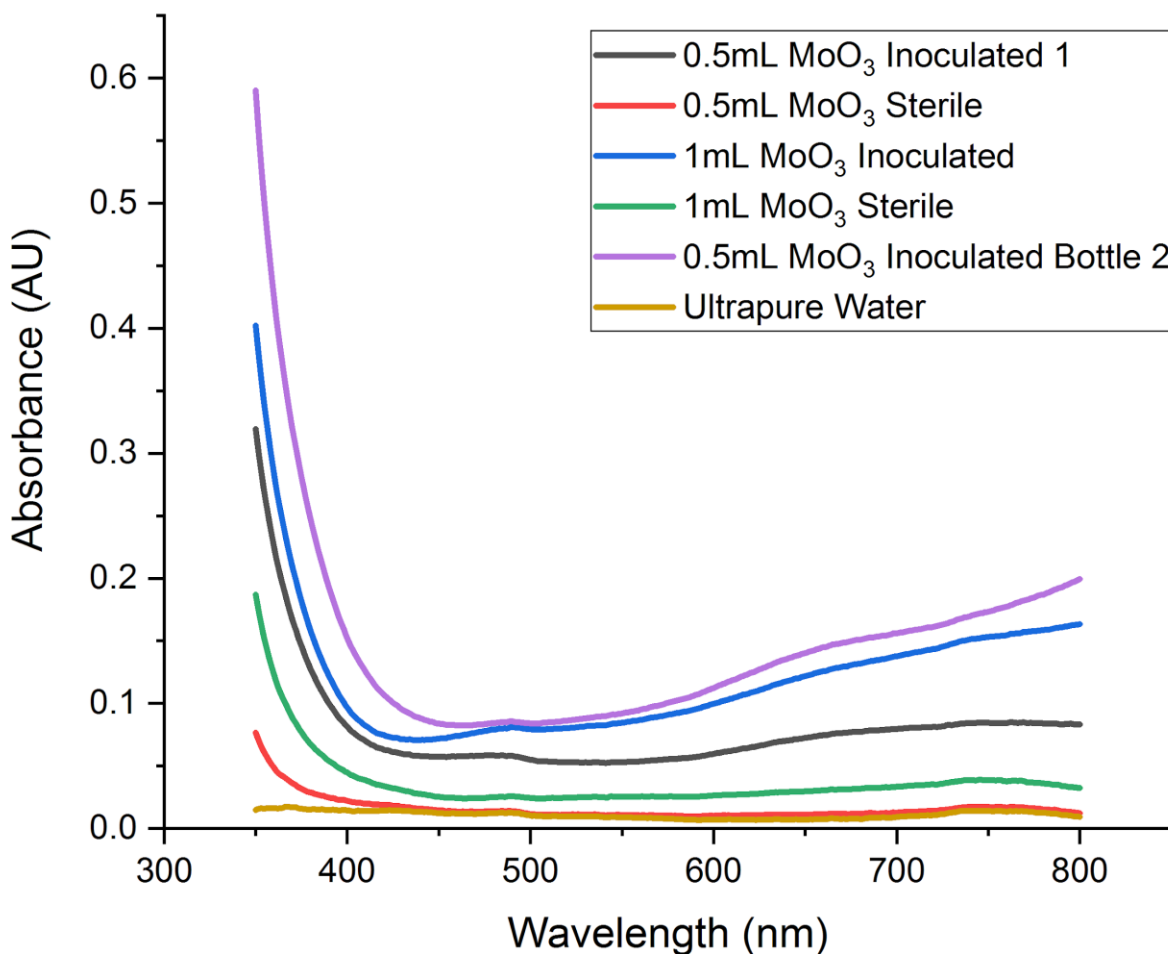


Figure 37: Absorbance spectroscopy for various molybdenum batches.

Above is the absorbance data for the controlled-molybdenum batches. The samples exhibited a strong absorbance peak at low wavelengths (approximately 400 nm) as well as an increasing absorbance at higher wavelengths with a minimum absorbance at around 450 nm. This is consistent with what has been observed in the literature [107]. The sterile batches also exhibited low-frequency absorbance, albeit not as strongly as in the inoculated batches.

In this experiment, as compared with the experiment in 4.2, there is not a strong relationship between the amount of thiosulfate present and the degree of absorbance in the inoculated batches. This may be an indication that a pH-based disruption in bacterial metabolism that prevented the bacteria from fully metabolizing the thiosulfate present into hydrogen sulfide.

4.4 Conclusions

In this section, I have presented a method for synthesizing MoS₂ nanoparticles using *Shewanella oneidensis* MR-1. This is the first known reported study of *Shewanella* as a pathway to synthesizing MoS₂. Furthermore, it is the first study of using a single bacterium to reduce Mo(VI) to two different oxidation states by changing a cultivation variable. SEM/EDS analysis, as well as XRD and Raman analysis of dried samples from cultivation, suggest that the synthesis requires multiple steps. *Shewanella* utilizes thiosulfate as an electron acceptor and reduces it, producing hydrogen sulfide gas. Meanwhile, *Shewanella* also reduces solid-phase MoO₃, leading to the evolution of dissolved tetravalent Mo⁴⁺ in solution. Finally, *Shewanella* biofilms provide a nucleation site that facilitates the precipitation of MoS₂. Because this synthesis requires dissimilatory metal reduction, it proceeds more slowly than the PbS and CdS synthesis reactions described in earlier sections, which were simply sulfide precipitation reactions. Notably, SEM images revealed much more pronounced nanowires that appeared in the experiments described in earlier chapters. This result is consistent with active dissimilatory metal reduction of a solid-phase metallic compound by *Shewanella* [5]. In addition to the apparent formation of MoS₂ at *Shewanella* biofilm sites, an orange color appeared in the inoculated batches, which may be MoS₂ at lower concentrations or may be other materials formed through *Shewanella* metabolic activity, such as other soluble molybdenum complexes.

The MoS₂ nanoparticles generated using this method appear to be polydisperse with a size range of approximately 50-200 nm. The nanoparticles are crystalline and appear to consist of polycrystalline aggregates in some cases. Analysis has yet to reveal the exact crystalline structure present, but XRD results suggest the possibility that both rhombohedral and hexagonal crystal phases are present.

The first experiment, described above, revealed the biosynthesis of MoS₂ at a pH of 6.8, which is consistent with best practices for *Shewanella* cultivation. In a second experiment, the pH

of the cultivation medium drifted at 4.5 and the materials produced were significantly different from those in the earlier batch. The cultivation medium in this experiment turned deep blue in *Shewanella*-inoculated bottles and exhibited an absorption peak consistent with prior studies of biogenerated Mo(V). The results suggest that *Shewanella* is capable of synthesizing Mo(V) in addition to Mo(IV) and MoS₂. The fact that Mo(V) appeared in a hostile low-pH medium suggests that Mo(V) may be formed by *Shewanella* as a precursor to Mo(VI), and was not fully reduced due to failure of the biofilm in the low-pH environment. Another possibility is that proteins secreted by *Shewanella* have the ability to reduce Mo(VI) to Mo(V) even when metabolic activity ceases, but Mo(IV) can only be formed when dissimilatory metal reduction is possible. Further controlled trials are needed to evaluate these possibilities.

5. SURFACES AND ELECTROCHEMISTRY

5.1 Characterization of *Shewanella* Interactions with Surfaces

Much of this work has been devoted to the exploration of *Shewanella oneidensis* MR-1's capacity to generate semiconductor nanoparticles. However, as alluded to in section 1.2.3, more potential device applications emerge when we consider the use of living *Shewanella* biofilms to create living sensors. In this section, I will present work exploring the observed interaction between *Shewanella* biofilms and various substrate materials.

5.1.1 Silicon

Given the consistency of its physical properties and its ubiquity in electronics, silicon is a valuable material for potential biosensors [108]. Prior work has established that *Shewanella* can form electronic interfaces with metallic and semiconducting materials such as gold and HOPG [7], but as far as we are aware, bacterial nanowire interfaces with silicon have not yet been reported or studied. In this section we present evidence of such an interface.

As described in earlier sections, samples harvested from the experiments described in chapters 2 through 4 were prepared for SEM imaging by dropping live culture media onto a clean silicon slab, followed by a dehydration and drying protocol. When viewed using SEM and EDS, the molybdenum, lead, and cadmium-enhanced media also appeared to exhibit nanowire

Portions of this chapter previously appeared as J. Rees, S. Sawyer and Y. Gorby, "Behavior of *Shewanella Oneidensis* MR-1 in a Sulfur and Zinc-Rich Medium and its Applications of Biosensing and Biomaterials," in *2018 Albany Nanotechnology Symp. (ANTS)*, Albany, NY, Nov. 14-15, 2018, to be published.

Portions of this chapter previously appeared as J. Rees, S. Sawyer and Y. Gorby, "Behavior of *Shewanella Oneidensis* MR-1 in a Sulfur and Zinc-Rich Medium and its Applications for Biosensing and Biomaterials," in *AVS Pacific Rim Symp. on Surfaces, Coatings and Interfaces*, Waikoloa, HI, Dec. 2-5, 2018, to be published.

connections between bacterial biofilms and the silicon substrate to varying degrees. These were most pronounced in the molybdenum-enhanced media but were also observed in the cadmium and lead experiments to a lesser extent.

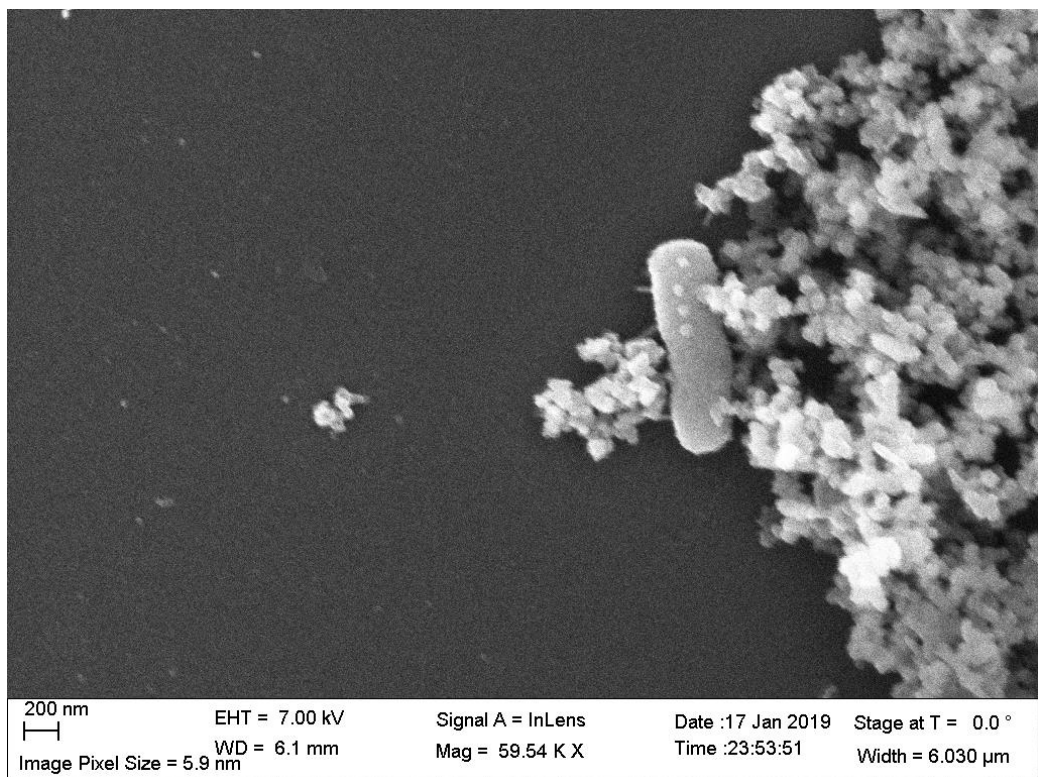


Figure 38: *Shewanella* nanowire formation in the presence of cadmium.

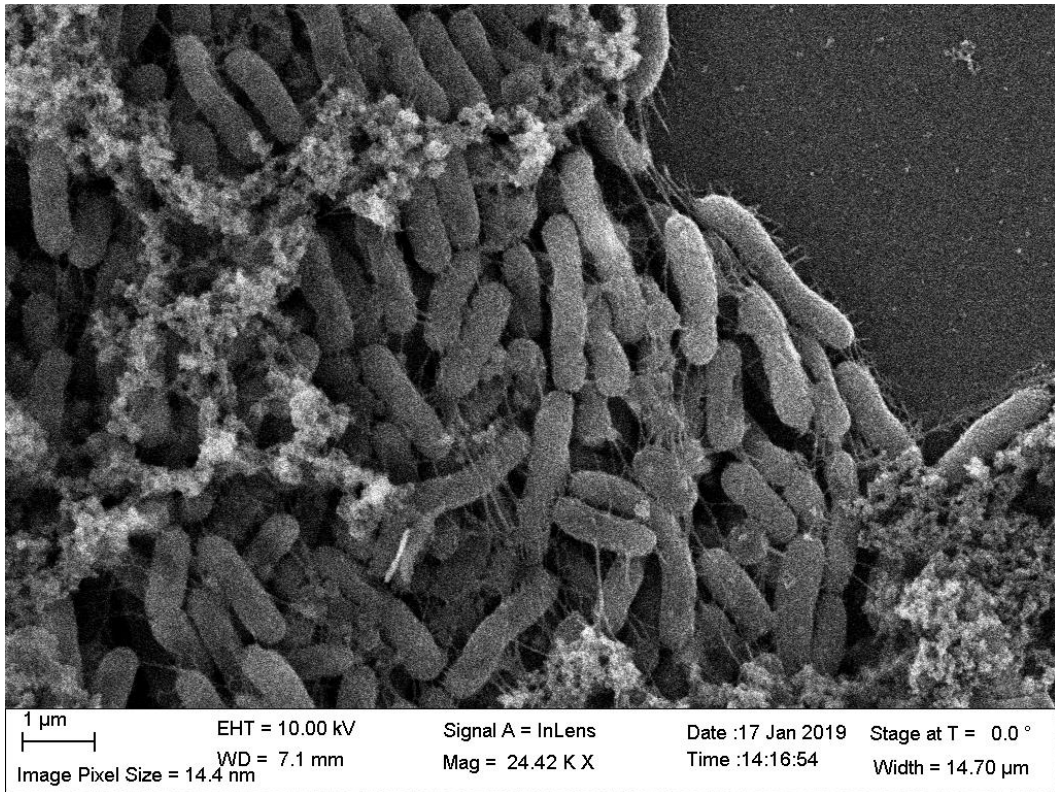


Figure 39: *Shewanella* nanowire formation in the presence of molybdenum.

5.1.2 Reduced Graphene Oxide

Graphene is an allotrope of carbon consisting of a series of carbon atoms arranged in a hexagonal lattice and tending to form monolayers due to the weak interlayer bonds. It is a semimetal, meaning that it exhibits an overlap between its conduction and valence bands and does not have distinct conducting and non-conducting states as would a semiconductor with a defined band gap [109]. Graphene also undergoes surface functionalization - its surface will form bonds with a range of molecules [110]. For biosensor applications, this means that graphene is an excellent electrode material to facilitate electron transfer to and from, and thus the sensing of, enzymes and other biomolecules [111].

Because many of graphene's useful properties are related to its surface dynamics, graphene electrode and biosensor designs often attempt to achieve porous graphene surfaces. Such surfaces, when the correct topography and pore size are achieved, have the potential to greatly increase the area of interface between an electrode and an adhered living biofilm,

proportionally increased the amount of current transfer than can occur between the system. A significant amount of current research is devoted to optimizing such surfaces in graphene electrodes as well as electrodes made from other materials [112].

The experiment performed in this section were performed using microporous graphene papers that were produced by reducing graphene oxide using a photoflash system. These papers were square, had a thickness of 10-20 microns, and had a diameter of approximately 1 cm. SEM inspection confirmed that areas of the microporous graphene possessed micron-scale pores that arose due to the photoflash process [113].

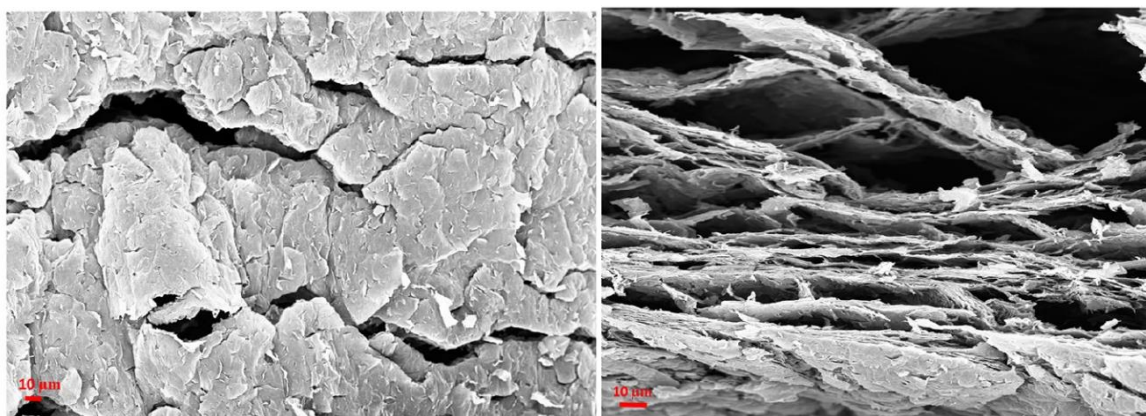


Figure 40: SEM micrograph of reduced graphene oxide. [113]

Graphene papers prepared as described above were immersed in sterile standard *Shewanella oneidensis* MR-1 medium batches prepared without potassium phosphate monobasic. The medium was inoculated with live *Shewanella* bacteria and incubated for five days at 30°C while being agitated at 100 rpm. At the end of five days, the graphene paper was removed and put through the dehydration and HMDS drying protocol described elsewhere in this work. The sample was then imaged using the Supra 55 FESEM.

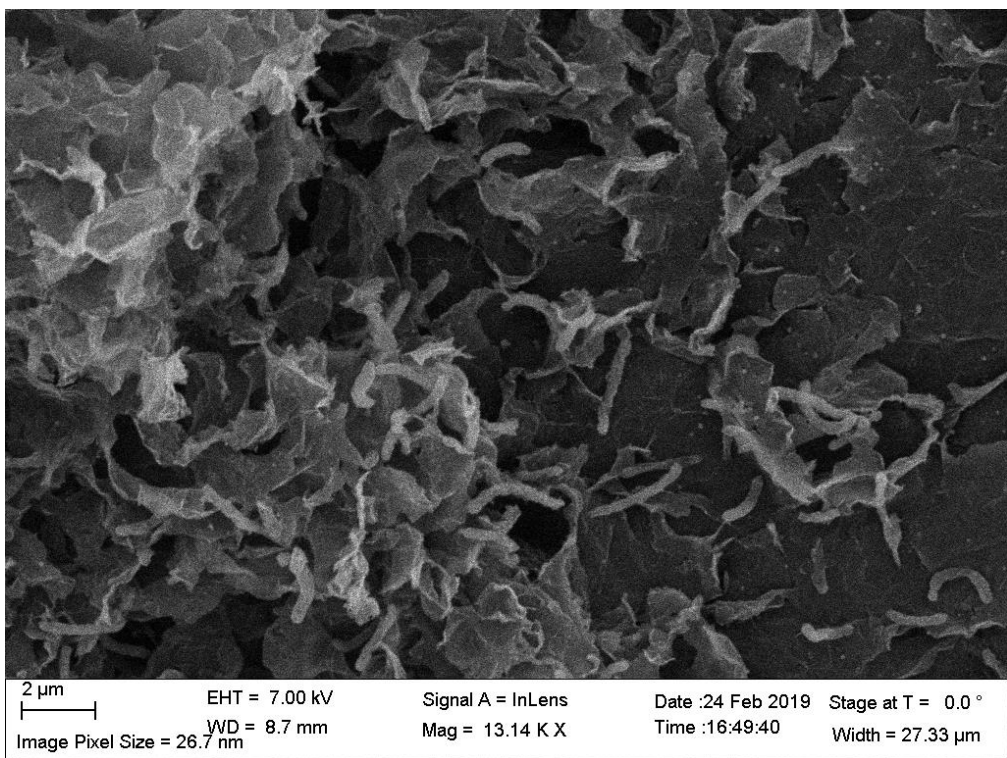


Figure 41: *Shewanella* growing in the micropores of reduced graphene oxide.

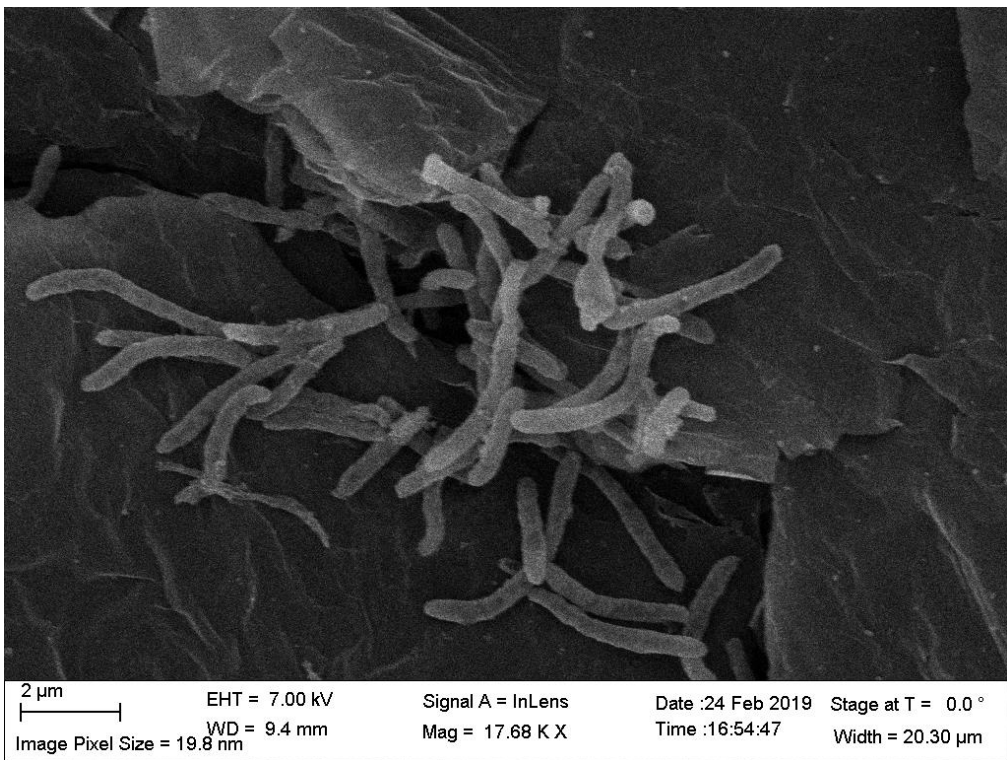


Figure 42: A cluster of *Shewanella* bacteria growing on reduced graphene oxide.

SEM images of the graphene papers revealed a microporous surface with bacteria adhered to the inside of the pores, both individually and as aggregates. Images did not reveal visible nanowire growth.

5.1.3 Microporous Alumina

When a surface in a bacterial culture medium contains micropores on the length scale of a few microns, as did the graphene described in the previous section, these pores provide a site for bacterial growth that can potentially increase the bacteria-electrode interface surface area. If the pore size becomes smaller, bacteria will no longer be able to inhabit the pores. Nonetheless, other effects of interest for electrochemical synthesis and nanoparticle generation begin to appear at these small pore sizes. Microporous surfaces, whose pore diameters are generally below 100 nm, have been studied as potential templates for a range of nanomaterials. For instance, prior work has indicated that the wetting of anodic aluminum oxide, which has nanopores of controllable size,, can be an effective means of precipitating polymeric or crystalline nanomaterials [114][115].

In the following experiments I examined the evolution of bacterial biofilms and nanomaterials on the surface of a Sigma Aldrich SmartPor anodic alumina oxide membrane, which initial SEM confirmed to have a microporous surface on a scale much less than 1 micron.

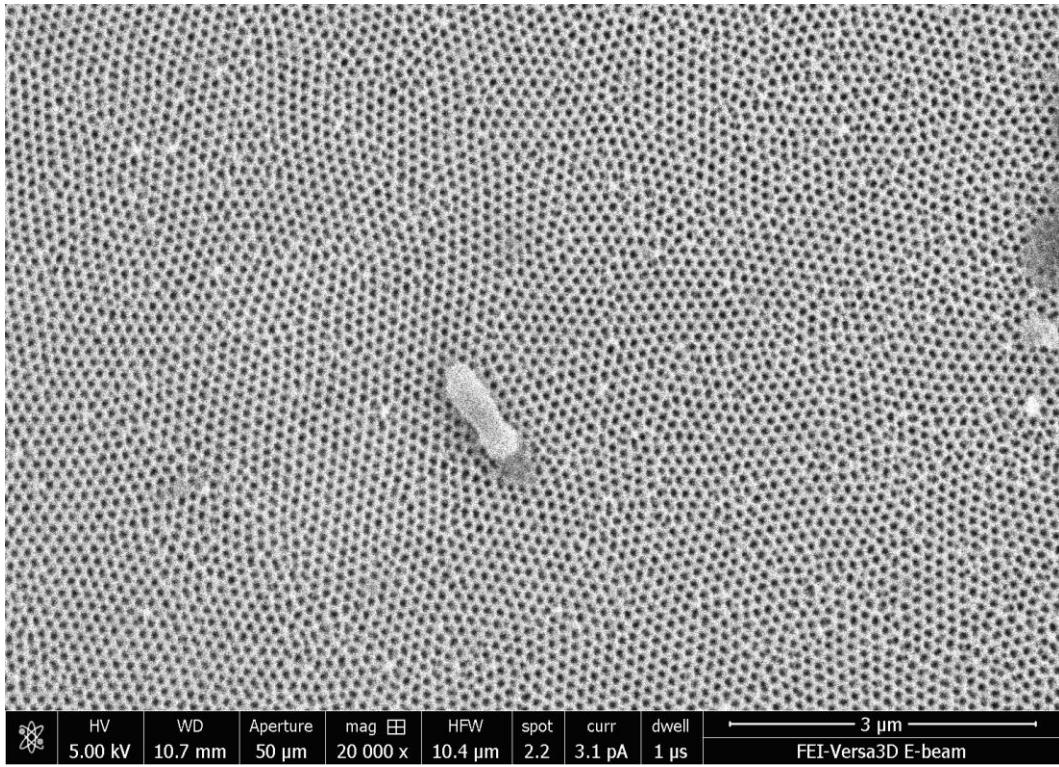


Figure 43: Bare microporous alumina, with a bacterium for scale (center).

5.1.3.1 Incubation with Zinc and Phosphate

After initial SEM, *Shewanella* was cultivated in a jar with a Gamry Ag/AgCl reference electrode, titanium counter electrode and steel working electrode with Sigma Aldrich SmartPor (microporous alumina) attached with copper tape. The medium contained 10x buffer concentration to prevent pH drift, 10 mM sodium thiosulfate, and 10mM zinc sulfate. During incubation, the working electrode was biased to -0.5V relative to the reference electrode and the jar was allowed to remain at room temperature without agitation.

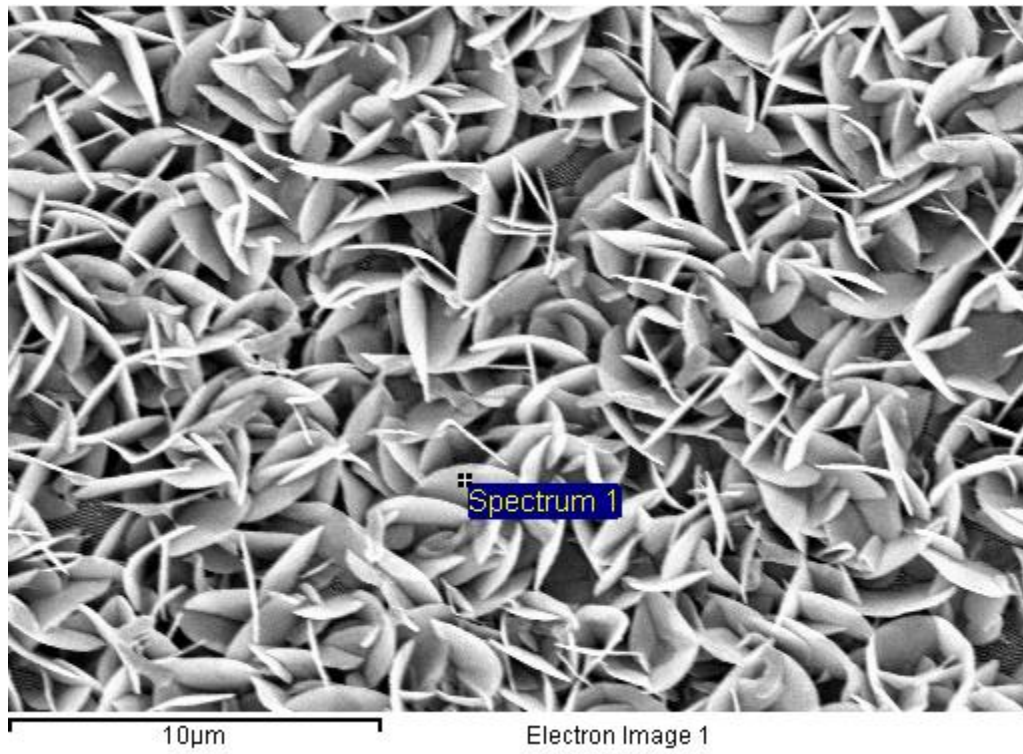


Figure 44: Surface of SmartPor working electrode after crystal growth.

SEM revealed that after cultivation, SmartPor was coated in crystal growth, with bacteria visible among the crystals in some locations. EDS analysis revealed that the crystals consisted of zinc phosphate (13.40% zinc, 9.93% phosphorous, 13.76% aluminum, and 62.90% oxygen by atomic percentage.) Meanwhile, a parallel experiment EDS analysis of a sterile medium with the same composition revealed 14.97% zinc, 15.28% sulfur, 0.98% phosphorous, and 47.70% oxygen by atomic percentage in the recovered biominerals, suggesting the presence zinc sulfate but not zinc phosphate.

5.1.3.2 Incubation Without Zinc and Phosphate

In this experiment, a slab of SmartPor was placed in a standard phosphate-free *Shewanella* growth medium that contained 10 mM sodium thiosulfate and no zinc sulfate. The batch was inoculated and incubated at 30°C and 100 rpm for 4 days, then dehydrated and dried using the ethanol/HMDS procedure and sputter coated. EDS analysis performed on this sample

revealed that a range of different structures had developed on the SmartPor surface. These included small crystals that were both morphologically and compositionally different from the crystals that formed in the presence of the zinc and phosphorous compounds in the previous experiment. It also included biofilm growth, which in some cases appeared to cover the surface of the SmartPor in a mat of carbon-based material. Features are color coded in Figure 46; the blue circle indicates a coating of microcrystals on the alumina, the yellow indicates fibrous organic material, presumed to be extracellular polysaccharides, the green circle indicates the bare surface of the microporous alumina and the red circle indicates a *Shewanella* bacterium. EDS analysis at the site shown in Figure 47 indicated 64.51% oxygen, 0.93% sodium, 30.59% oxygen, and 1.99% sulfur by atomic percentage.

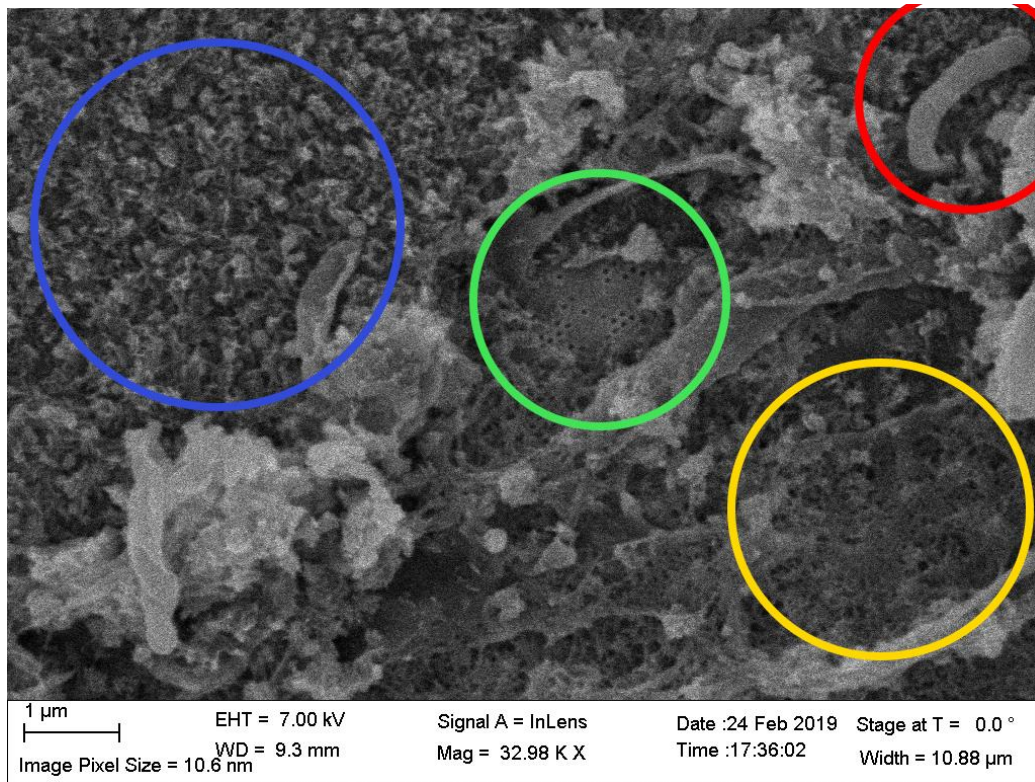


Figure 45: *Shewanella* growing on microporous alumina.

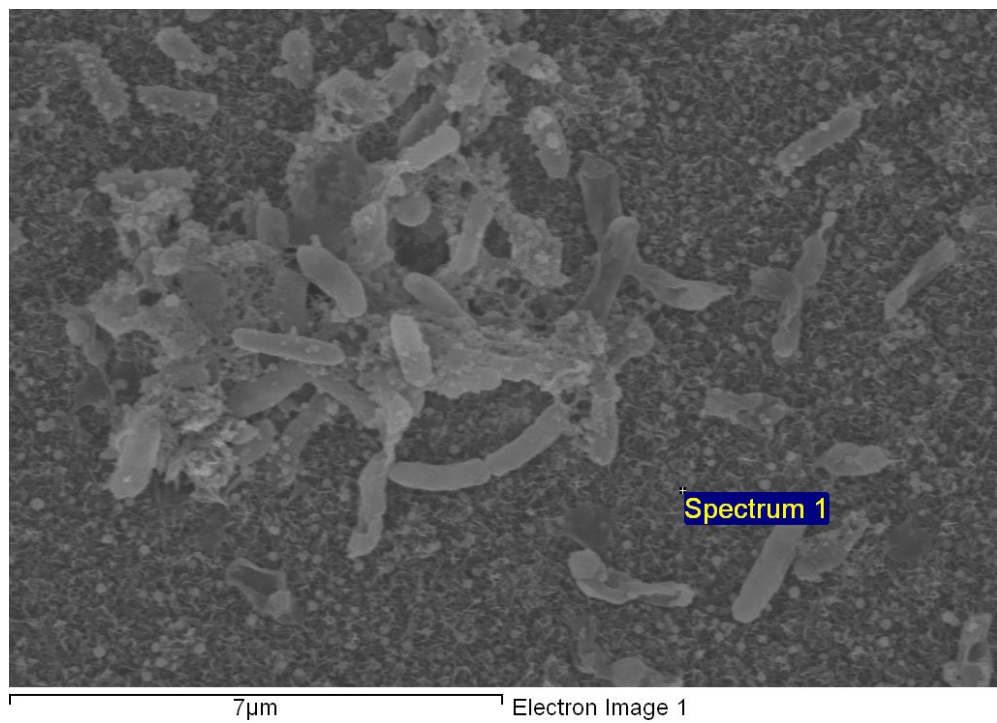


Figure 46: Point EDS analysis of surface nanocrystals.

5.2 Electrochemical Characterization of Aqueous *Shewanella* Systems

5.2.1 Measurement of Current During Cultivation

During the experiment described in section 5.1.3.1, the potentiostat registered a DC current that fluctuated on the time scale of approximately 24h. A lack of control over ambient conditions in this experiment prevents absolute determination of the cause of this fluctuation; however, there are a few possible causes for the phenomenon. One possibility is that diurnal fluctuations in temperature affected the rate of bacterial metabolism and caused a corresponding increase in current. A second possibility is that, since the cultivation jar incubated in a room with exterior windows, the daily fluctuations in ambient light, and especially UV light, caused a response in the bacteria and the generation of photocurrent in any semiconductor nanoparticles present on the electrode. A third and final possibility is that the current fluctuations are evidence of a bacterial circadian rhythm, as has been reported in some species of cyanobacteria. [116]

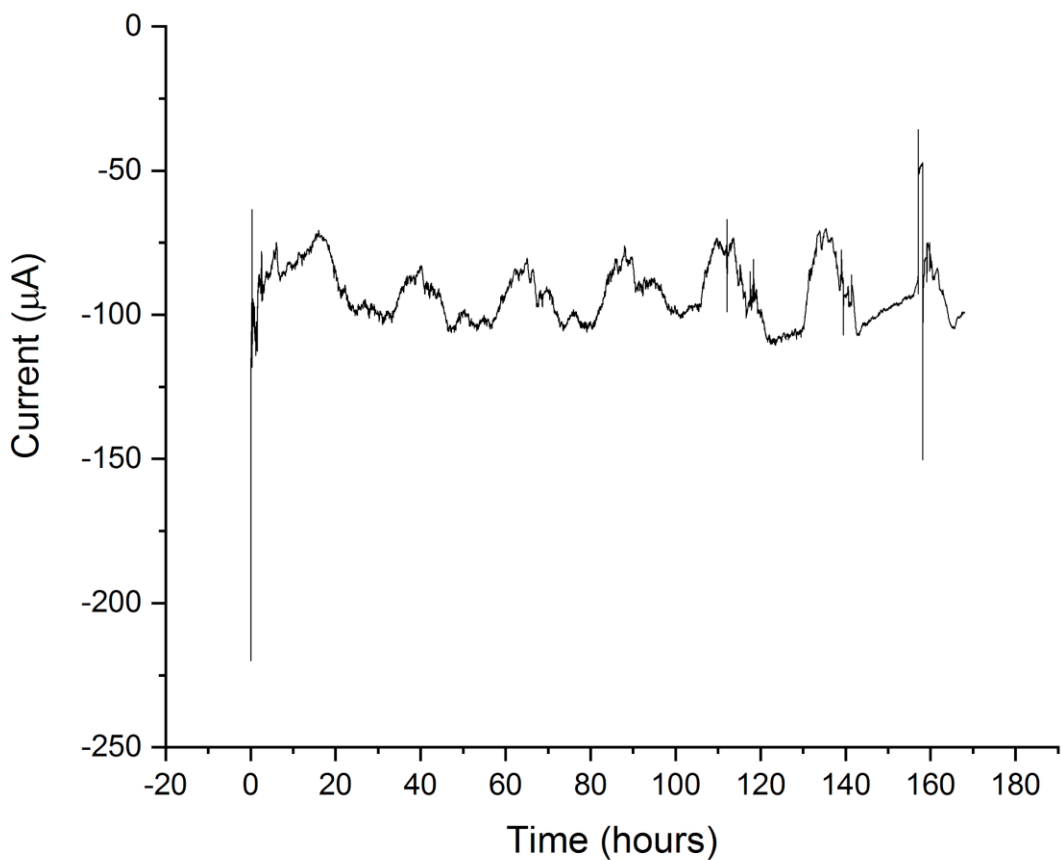


Figure 47: Current fluctuation during *Shewanella* incubation.

5.2.2 Three-Electrode Zinc System with Two Jars

Shewanella oneidensis MR-1 was cultivated in a jar containing a working, reference and counter electrode. Modified standard MR-1 medium with 5 mM sodium thiosulfate, no phosphate, and 15mM PIPES buffer instead of 3mM to help prevent pH drift. 30mL of *Shewanella* inoculum was added to one jar while the other was kept sterile. The jars were incubated at 30°C and agitated at 50 rpm 3 days, then 5mM zinc sulfate was added to both. Incubation and agitation continued for 3 more days. Jars were then characterized using cyclic voltammetry.



Figure 48: Visual difference between inoculated (right) and sterile (left) jar batches.

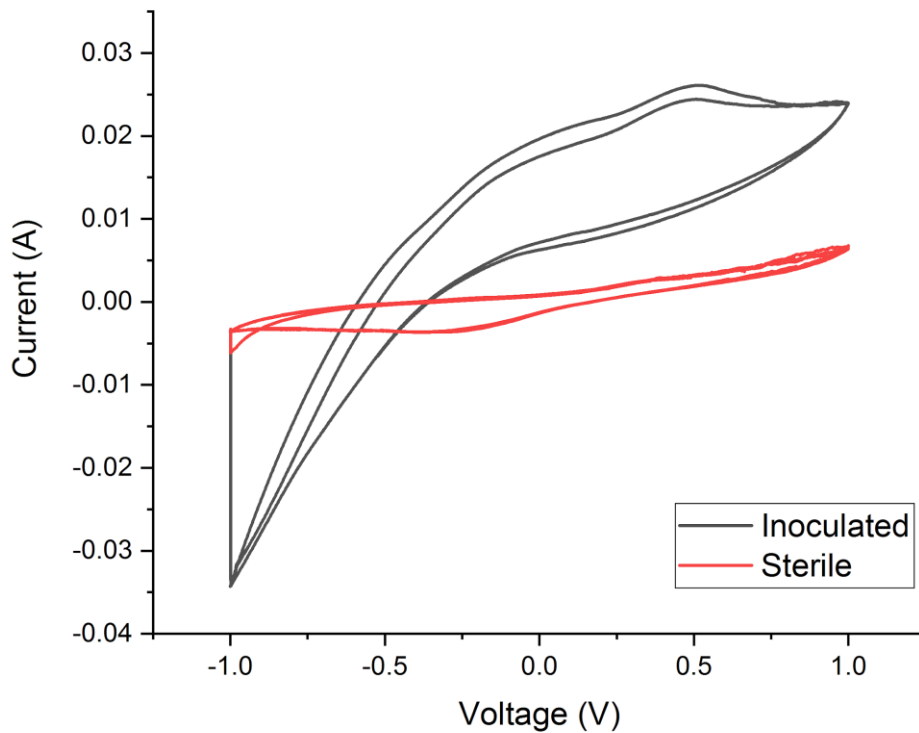
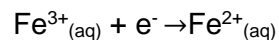


Figure 49: Cyclic voltammetry scan of the jars at 10mV/sec.

At a scan rate of 10mV/sec, a redox peak can be seen at approximately +500mV, consistent in its location with the $\text{Fe}^{3+}/\text{Fe}^{2+}$ redox reaction [1]:



The steeper slope of the inoculated batch compared to the sterile batch curve also suggests decreased solution resistance, possibly due to the dissolution of iron species into solution by *Shewanella* acting on the electrode.

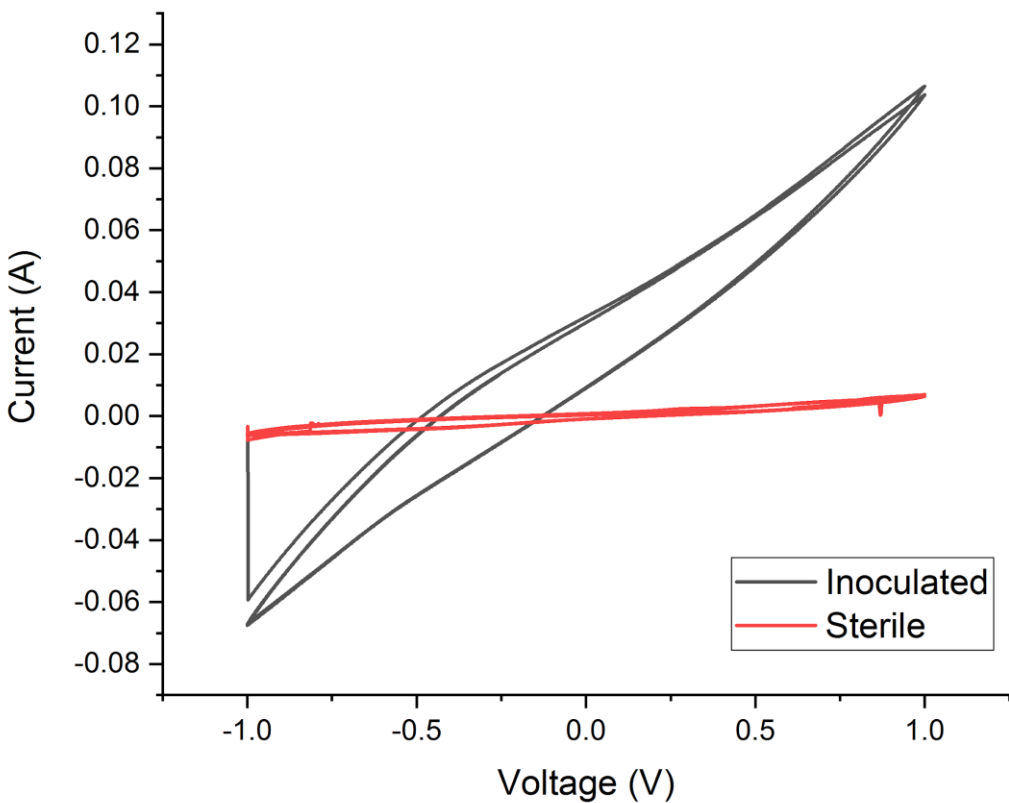


Figure 50: Cyclic voltammetry scan of the jars at 50mV/sec.

At a higher scan rate, the redox peak in the inoculated curve disappears. This is likely an indication that the electrochemical process causing the curve is either irreversible or diffusion-limited such that it cannot reverse on the time scale of a 50mV/sec scan period.

5.2.3 Three-Electrode Zinc System with Three Jars

Next, the experiment from the previous section was repeated using three jars: one inoculated with 20mM zinc sulfate, one inoculated with 10mM zinc sulfate, and one left sterile with 10mM zinc sulfate. In contrast with the electrodes used in the two-jar experiment, the electrodes in this experiment had no copper tape or SmartPor on their surface and were mechanically polished before the experiment to remove all corrosion from air exposure and prior use. This was done to reduce the number of materials present at the working electrode interface and therefore reduce the number of variables with a possible influence on the cyclic voltammetry curve. These

jars were incubated at 30°C and agitated at 50 rpm for 22 days, then a Gamry Ag/AgCl working electrode was inserted and cyclic voltammetry was performed on all jars.

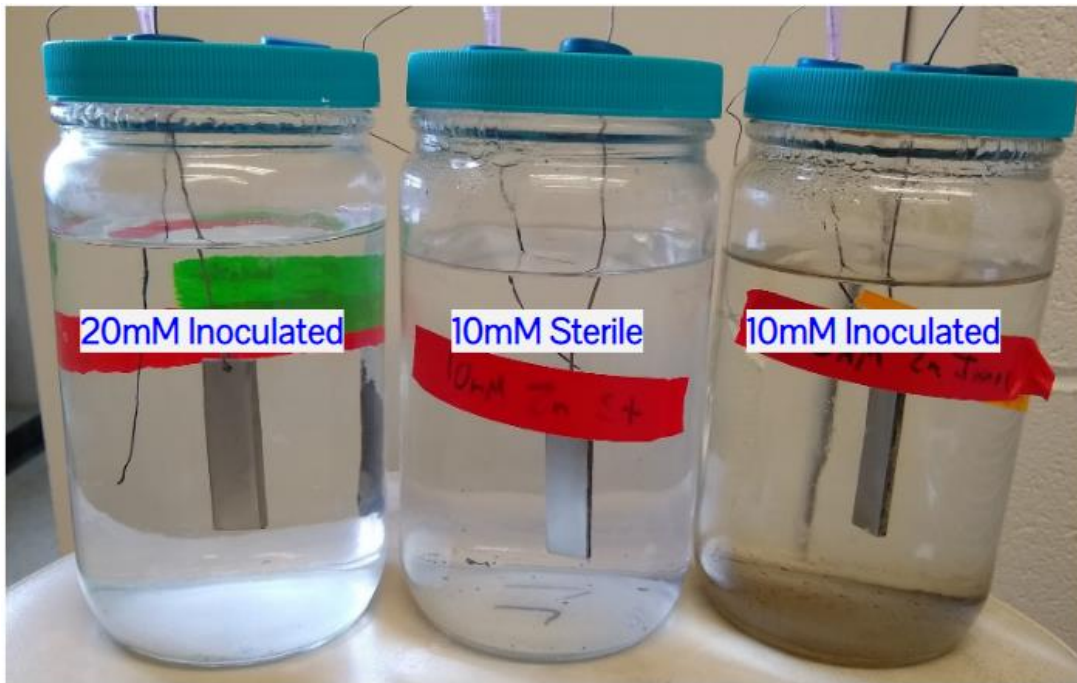


Figure 51: Incubation jars for the *Shewanella* three-jar incubation experiment.

As indicated in the figure above, the 10mM inoculated jar developed brown precipitates visually consistent with iron oxide while the other two jars did not. Cyclic voltammetric measurements performed on the 10mM thiosulfate inoculated jar revealed a redox peak at approximately +110 mV that was not visible in the other two jars and that disappeared at higher scan rates (in the chart above, scan rate used was 50mV/sec) This peak is consistent in its location with some prior measurements of the redox peaks of *Shewanella* cytochromes [117]. One possible interpretation of this peak is that it indicates that the activity of *Shewanella* is greater in this jar as compared with the other two jars, leading to both the appearance of a cytochrome-related redox peak and visual evidence of the by-products of *Shewanella* metabolic activity - in this case, iron corrosion by-products. The curve of the 10 mM inoculated jar was also significantly steeper than that of the other two jars, suggesting decreased solution resistance. In all jars, a peak at about -0.76V was visible, which is consistent with the zinc reduction-oxidation reaction

[1]:

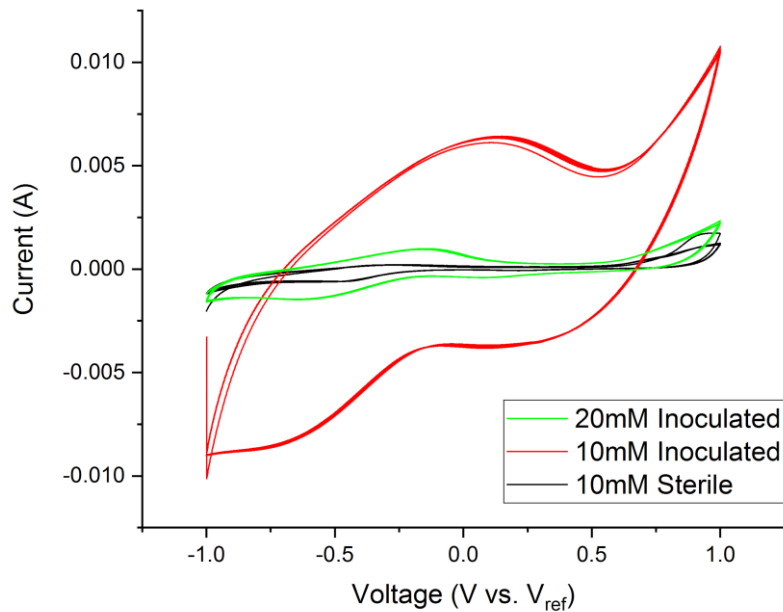
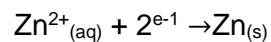


Figure 52: Comparison of the CV curves of the three jars at 50mV/sec scan rate.

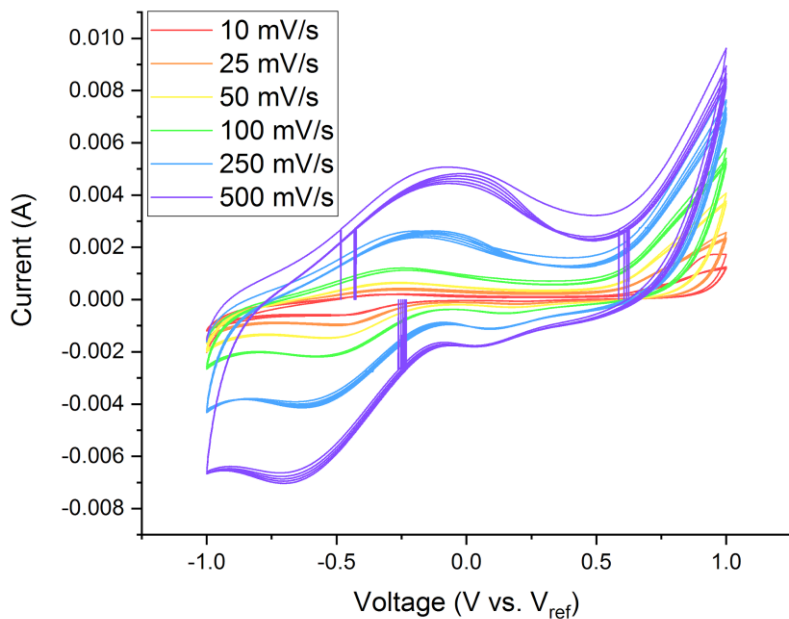


Figure 53: Cyclic voltammetry graph of the 10mM thiosulfate sterile jar.

When the 10 mM thiosulfate jar was scanned at a series of increasing scan rates, the +110mV peak peak appeared to drift and then vanish, suggesting that the peak is diffusion-limited in a manner similar to the peak detected in section 5.2.2.

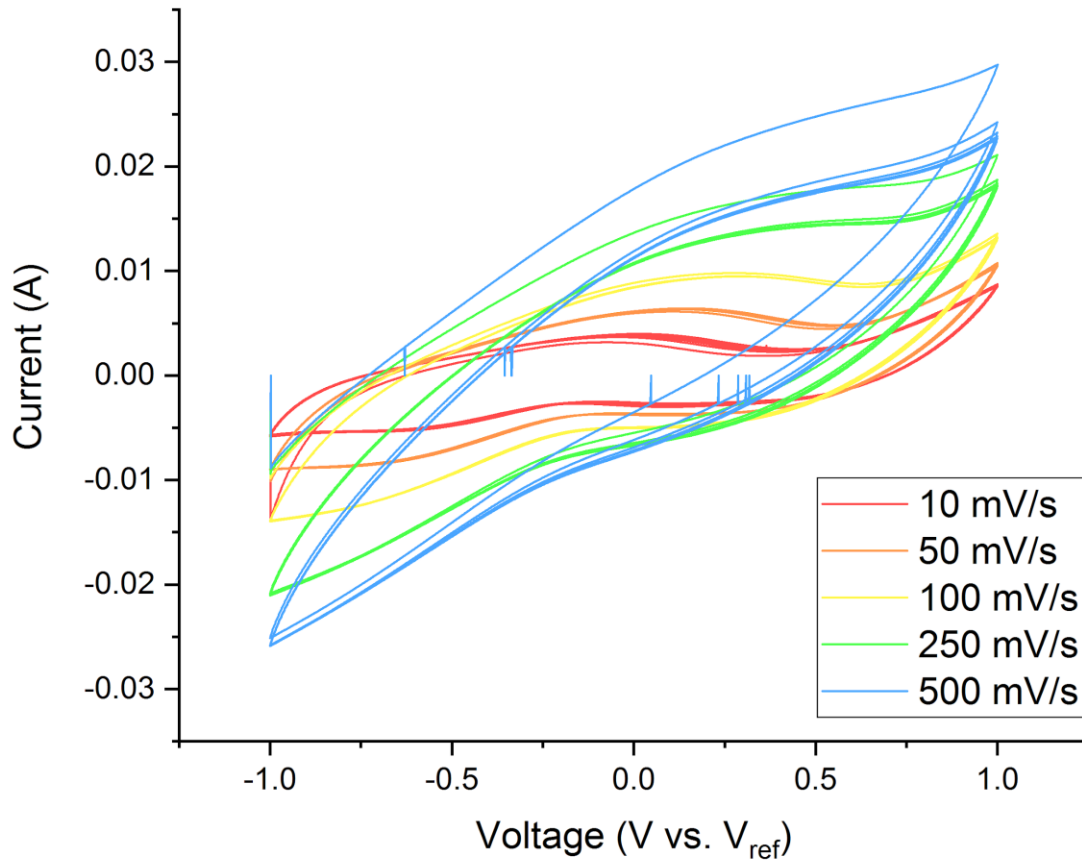


Figure 54: Cyclic voltammetry graph of the 10 mM thiosulfate inoculated jar..

A longitudinal study was also performed on the 10mM inoculated batch, with CV measurements take before and after the addition of inoculum, as well as after incubation. As indicated in the figure below, the CV curve was virtually unchanged by the addition of inoculum. However, in the post-incubation CV measurement, a substantial flattening of the -0.76V peak could be seen. This raises the possibility that the activity of *Shewanella* in the medium had decreased the amount of soluble zinc present.

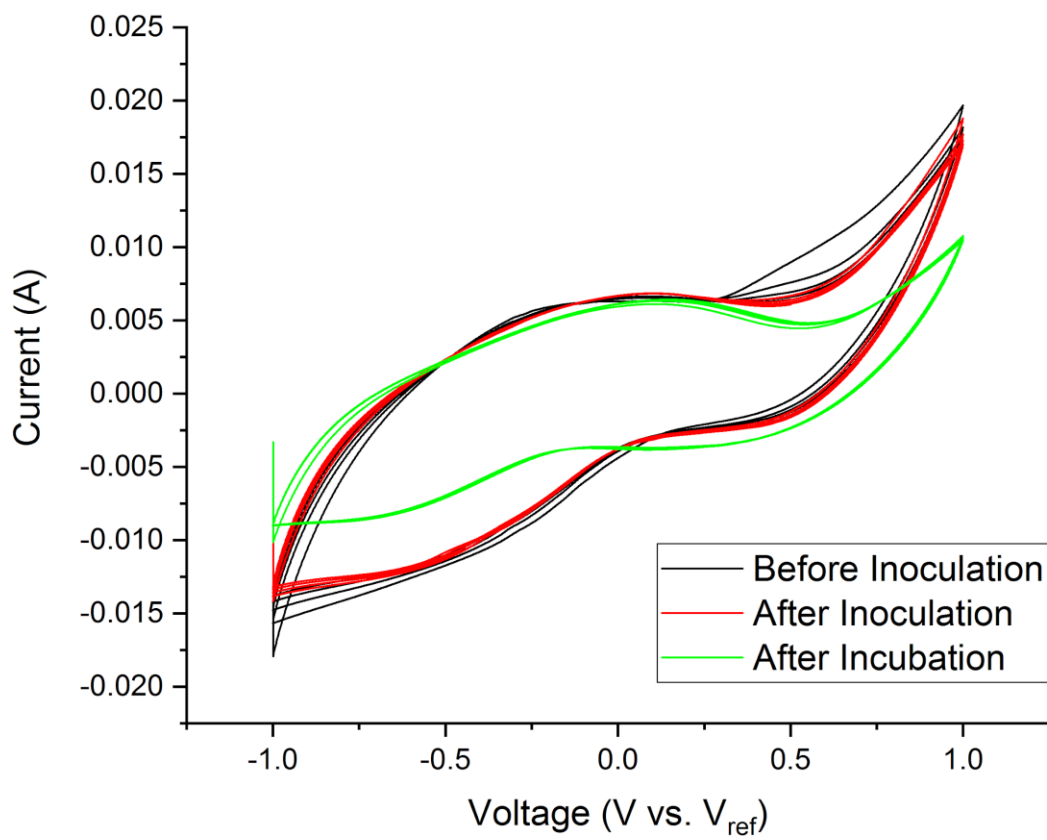


Figure 55: Longitudinal study of the 10mM thiosulfate inoculated jar at 50mV/s scan.

5.3 Conclusions

In this chapter I have reported several experimental observations that contribute to existing knowledge *Shewanella oneidensis* MR-1 growth on substrates. First, that *Shewanella* is capable of adhering to a silicon slab using bacterial nanowires. Second, that Microporous alumina (SmartPor) provides both a scaffolding for *Shewanella* growth and an excellent nucleation site for crystals in a *Shewanella* medium, with the crystals reflecting the chemistry of the medium. Third, that reduced graphene oxide created using photoflash exhibits pores on the length scale of several microns, and *Shewanella* can colonize these pores.

In addition, I report several results from electrochemical characterization. Results from the electrochemical analysis of the zinc-enhanced three-electrode system are still preliminary, but features of the curves appear to correspond to temperature or light, microbial activity or corrosion, and aqueous chemistry. The cyclic voltammetry curves that result from the measurement of aqueous systems with living *Shewanella* colonies growing on electrodes exhibit several distinct reduction-oxidation peaks at locations that are suggestive of redox reactions for electron acceptor materials that were available to the bacteria in the medium, including iron and zinc. Furthermore, these redox peaks showed diffusion-limited behavior, suggesting that they involved solid-phase materials adhered to the electrode.

6. CONCLUSIONS AND FUTURE WORK

6.1 Summary

In this work I have presented several novel controlled studies of semiconductor nanoparticle synthesis using *Shewanella oneidensis* MR-1. First, I presented a successful method of using *Shewanella* to synthesize lead sulfide nanoparticles. The proposed method for the synthesis is hydrogen sulfide formation due to the metabolism of thiosulfate bacteria, followed by a precipitation reaction in which lead ions combined with hydrogen sulfide and nucleated on the biofilm surface. This is the first known reported study of the properties of PbS nanoparticles generated in this manner.

Secondly, I have demonstrated the successfully synthesized CdS nanoparticles using *Shewanella* in the first known controlled study in which cultivation variables were manipulated and the physical properties of the generated nanoparticles were studied. The proposed mechanism was similar to that proposed for the lead sulfide synthesis: bacterial reduction of thiosulfate, precipitation, and nucleation on the biofilm. Additional studies with varied inoculum states suggest that CdS cannot form in this liquid medium without live *Shewanella* present. SEM analysis has also revealed novel hollow microstructures consisting of cadmium, oxygen and carbon with bacteria growing inside and evidence of a chemical micro-environment different from the environment outside of the spheres.

Chapter 4 presented a method for synthesizing molybdenum disulfide nanoparticles using *Shewanella oneidensis* MR-1 - the first known use of using *Shewanella* to do so. Furthermore, it is the first study of using a single bacterium to reduce Mo(VI) to two different oxidation states by changing a cultivation variable. The proposed mechanism for MoS₂ synthesis is that *Shewanella* metabolically reduces thiosulfate ions to hydrogen sulfide and Mo(VI) ions to Mo(IV), then catalyzes a precipitation reaction on the biofilm surface.

SEM images for this experiment revealed much more pronounced nanowires than appeared in the cadmium and lead experiments. This result is consistent with active dissimilatory metal reduction of a solid-phase metallic compound by *Shewanella* [5]. In addition to the apparent formation of MoS₂ at *Shewanella* biofilm sites, an orange color appeared in the inoculated batches, which may be MoS₂ at lower concentrations or may be other materials formed through *Shewanella* metabolic activity, such as other soluble molybdenum complexes.

The MoS₂ nanoparticles generated using this method appear to be polydisperse with a size range of approximately 50-200 nm. The nanoparticles are crystalline and appear to consist of polycrystalline aggregates in some cases. Analysis has yet to reveal the exact crystalline structure present, but XRD results suggest the possibility that both rhombohedral and hexagonal crystal phases are present.

The first experiment, described above, revealed the biosynthesis of MoS₂ at a pH of 6.8, which is consistent with best practices for *Shewanella* cultivation. In a second experiment, the pH of the cultivation medium drifted at 4.5 and the materials produced were significantly different from those in the earlier batch. The cultivation medium in this experiment turned deep blue in *Shewanella*-inoculated bottles and exhibited an absorption peak consistent with prior studies of bacterially-synthesized Mo(V). The results suggest that *Shewanella* is capable of synthesizing Mo(V) in addition to Mo(IV) and MoS₂. The fact that Mo(V) appeared in a hostile low-pH medium suggests that Mo(V) may be formed by *Shewanella* as a precursor to Mo(VI), and was not fully reduced to failure of the biofilm in the low-pH environment. Another possibility is that proteins secreted by *Shewanella* have the ability to reduce Mo(VI) to Mo(V) even when metabolic activity ceases, but Mo(IV) can only be formed when dissimilatory metal reduction is possible. Further controlled trials are needed to evaluate these possibilities.

In chapter 5 I reported several experimental observations that contribute to existing knowledge *Shewanella oneidensis* MR-1 growth on substrates. *Shewanella* was observed colonizing reduced graphene oxide pores and forming nanowire connections with silicon. When

microporous alumina (SmartPor) was immersed in a growth medium with *Shewanella*, it supported both *Shewanella* growth and the growth of crystals whose composition reflected *Shewanella*'s impact on the chemistry of the medium. Electrochemical characterization of three-electrode systems with *Shewanella* growing in an aqueous medium was also undertaken. Features of the cyclic voltammetry curves for these systems corresponded to features of the growth media, including changes in temperature or light, microbial activity or corrosion, and several aspects of the jars' aqueous chemistry.

6.2 Lessons and Future Work

Table 7: Limitations in current work and lessons for future work.

Limitation	Lesson
Batch cultivation produces variable results	Perform continuous cultivation using a chemostat
Electrochemical experiments produced variable results	More careful control of cultivation variables is needed
TEM diffraction analysis did not lead to conclusions about MoS ₂ crystal structure	Careful calibration procedures, sonication of nanoparticulate samples
XRD peaks indicated the presence of undesired salts	More thorough sonication, sonication at higher RPM, possible chemical treatment

The table above presents lessons that arose from undertaking the work. Uniting these lessons is a common theme: biological synthesis is both highly variable by its intrinsic nature and highly responsive to environmental stimuli. This high responsiveness is one of the virtues of biosensing as a potential method of achieving high-sensitivity sensors beyond the capability of non-biological designs. However, it also means that the production of reliable biominerals using bacteria will require the use of highly controlled experimental conditions, and a major area of future work is that of establishing more reliable controlled incubation. An effective tool for controlled cultivation, to be used more extensively in future work, is a chemostat bioreactor. Chemostats allow the precise control of such variables as dissolved oxygen, pH, and nutrient concentration throughout incubation, and also allow the extraction of biological material without terminating cultivation. The heterogeneity of the materials generated through biological processes also presents an engineering challenge, evident in the results of this work that must be overcome

in the future. Nanoparticles are generated alongside a variety of salts and organic materials that must be extracted before the pure nanomaterials are available for use separately from the system.

Other methods could greatly extend the scope of the current work. One such method is electrochemical impedance spectroscopy (EIS), which employs identical or similar equipment to cyclic voltammetry but revolves around the application AC voltage, rather than DC, to a three-electrode electrochemical system. Much like an electrical circuit, an electrochemical system will exhibit frequency-dependent behavior arising from non-resistive impedances, especially capacitive ones. By applying a range of AC frequencies to the system and measuring how its response varies, it is possible to gain insights into the system that are difficult to obtain using cyclic voltammetry alone, such as electrode capacitance and details of diffusion behavior. [118] Through careful CV and EIS, study of biofilms and bacterial nanowires *in situ*, it may be possible to increase knowledge of which current responses correspond to which environmental conditions.

As described in the background section, the combination of electronically-active bacteria and electronically-active nanoparticles provides ample opportunities to create prototype devices, and near future work will explore this in greater depth. This includes spin-coating biosynthesized nanoparticles onto surfaces with nanofabricated contacts in order to create prototype photodetector devices. It also involves the creation of biosensor devices consisting of an inoculated electrode in an aqueous medium. Effectively testing such devices will require the creation of an environment in which temperature, and light, are all controlled.

The success of the three batch experiments presented in this work, along with the numerous other successful batch experiments reported in literature, attest to the sheer breadth of nanoparticulate materials that bacteria may be able to synthesize. Substantial future work should be devoted to attempting to synthesize new materials, altering the electron acceptor materials provided, the bacteria used, and other aspects of the culture medium and incubation process.

Finally, future work should investigate the behavior of biofilms in larger, more complex systems. Once bacterial biosensors are successfully deployed in a lab environment, they should

be tested in real aquatic systems, or alternative biosensor systems should be developed that utilize and encourage the growth the microbial ecologies in these waterways. Future research should also investigate the potential of bacterial nanoparticle formation in wastewater systems, which may include sewage systems, polluted mine sites, industrial waste disposal sites, or a wide range of other areas of waste treatment.

REFERENCES

- [1] P. Rieger, “Electrode potentials,” in *Electrochemistry*, 2nd ed. London, UK: Chapman & Hall, 1993.
- [2] G. Karp, *Cell and Molecular Biology*, 7th ed., Hoboken, NJ, USA: John Wiley & Sons, 2013.
- [3] G. J. Tortora, B. R. Funke, and C. L. Case, *Microbiology: An Introduction*, 11th ed. New York, NY, USA: Pearson, 2012.
- [4] S. Pirbadian *et al.*, “Bacterial nanowires of *Shewanella oneidensis* MR-1 are outer membrane and periplasmic extensions of the extracellular electron transport components,” *Proc. Natl. Acad. Sci. U.S.A.*, vol. 111, no. 35, pp. 12883–12888, Jul. 2014.
- [5] Y. A. Gorby *et al.*, “Electrically conductive bacterial nanowires produced by *Shewanella oneidensis* strain MR-1 and other microorganisms,” *Proc. Natl. Acad. Sci. U.S.A.*, vol. 103, no. 30, pp. 11358–11363, Jun. 2006.
- [6] S. Pirbadian and M. Y. El-Naggar, “Multistep hopping and extracellular charge transfer in microbial redox chains,” *Phys. Chem. Chem. Phys.*, vol. 14, no. 40, pp. 13802–13808, Jun. 2012.
- [7] K. M. Leung *et al.*, “*Shewanella oneidensis* MR-1 bacterial nanowires exhibit p-type, tunable electronic behavior,” *Nano Lett.*, vol. 13, no. 6, pp. 2407–2411, May 2013.
- [8] L. A. Zacharoff and M. Y. El-Naggar, “Redox conduction in biofilms: From respiration to living electronics,” *Curr. Opin. Electrochem.*, vol. 4, no. 1, pp. 182–189, Aug. 2017.
- [9] D. Thouless, “Electrons in disordered systems and the theory of localization,” *Phys. Rep.*, vol. 13, no. 3, pp. 93–142, Oct. 1974.
- [10] Y. Xiong *et al.*, “High-affinity binding and direct electron transfer to solid metals by the *Shewanella oneidensis* MR-1 outer membrane c-type cytochrome omcA,” *J. Am. Chem. Soc.*, vol. 128, no. 43, pp. 13978–13979, Oct. 2006.
- [11] M. Sun *et al.*, “A gold-sputtered carbon paper as an anode for improved electricity generation from a microbial fuel cell inoculated with *Shewanella oneidensis* MR-1,” *Biosens. Bioelectron.*, vol. 26, no. 2, pp. 338–343, Oct. 2010.
- [12] D. E. Ross *et al.*, “Towards electrosynthesis in *Shewanella*: Energetics of reversing the Mtr pathway for reductive metabolism,” *PLoS One*, vol. 6, no. 2, pp. 1–9, Feb. 2011.

- [13] S. Mann, "Inorganic structures of life," in *Biomineralization: Principles and Concepts in Bioinorganic Materials Chemistry*, New York, NY, USA: Oxford University Press, 2001.
- [14] O. J. Hao *et al.*, "Sulfate-reducing bacteria," *Crit. Rev. Environ. Sci. Technol.*, vol. 26, no. 2, pp. 155–187, Jan. 2009.
- [15] H. Venzlaff *et al.*, "Accelerated cathodic reaction in microbial corrosion of iron due to direct electron uptake by sulfate-reducing bacteria," *Corros. Sci.*, vol. 66, pp. 88–96, Jan. 2013.
- [16] K. Jalali and S. A. Baldwin, "The role of sulphate reducing bacteria in copper removal from aqueous sulphate solutions," *Water Res.*, vol. 34, no. 3, pp. 797–806, Feb. 2000.
- [17] I. Beech and C. Cheung, "Interactions of exopolymers produced by sulphate-reducing bacteria with metal ions," *Int. Biodeter. Biodegr.*, vol. 35, no. 1-3, pp. 59–72, Jan. 1995.
- [18] T. Klaus *et al.*, "Silver-based crystalline nanoparticles, microbially fabricated," *Proc. Natl. Acad. Sci. U.S.A.*, vol. 96, no. 24, pp. 13611–13614, Nov. 1999.
- [19] A. Mathuriya *et al.*, "Magnetotactic bacteria: Performances and challenges," *Geomicrobiol. J.*, vol. 32, no. 9, pp. 780–788, Jul. 2015.
- [20] R. Y. Sweeney *et al.*, "Bacterial biosynthesis of cadmium sulfide nanocrystals," *Chem. Biol.*, vol. 11, no. 11, pp. 1553–1559, Nov. 2004.
- [21] Y. Feng *et al.*, "Biosorption and bioreduction of trivalent aurum by photosynthetic bacteria *Rhodobacter capsulatus*," *Curr. Microbiol.*, vol. 55, no. 5, pp. 402–408, Aug. 2007.
- [22] D. R. Lovley, "Dissimilatory metal reduction," *Annu. Rev. Microbiol.*, vol. 47, no. 1, pp. 263–290, Oct. 1993.
- [23] K. Richter, M. Schicklberger, and J. Gescher, "Dissimilatory reduction of extracellular electron acceptors in anaerobic respiration," *Appl. Environ. Microbiol.*, vol. 78, no. 4, pp. 913–921, Dec. 2011.
- [24] T. J. DiChristina and E. F. DeLong, "Design and application of rRNA-targeted oligonucleotide probes for the dissimilatory iron- and manganese-reducing bacterium *Shewanella putrefaciens*," *Appl. Environ. Microbiol.*, vol. 59, no. 12, pp. 4152–4160, Dec. 1993.
- [25] H. Bao *et al.*, "Extracellular microbial synthesis of biocompatible CdTe quantum dots," *Acta Biomater.*, vol. 6, no. 9, pp. 3534–3541, Mar. 2010.

- [26] H. Fujii *et al.*, “Synthesis of TiO₂/CdS nanocomposite via TiO₂ coating on CdS nanoparticles by compartmentalized hydrolysis of Ti alkoxide,” *J. Mater. Sci.*, vol. 36, no. 2, pp. 527–532, Jan. 2001.
- [27] Z. Zhang *et al.*, “Redox reaction induced Ostwald ripening for size- and shape-focusing of palladium nanocrystals,” *Chem. Sci.*, vol. 6, no. 9, pp. 5197–5203, May 2015.
- [28] A. M. Fayaz *et al.*, “Fungal based synthesis of silver nanoparticles—An effect of temperature on the size of particles,” *Colloids Surf. B Biointerfaces*, vol. 74, no. 1, pp. 123–126, May 2009.
- [29] A. Yamagishi *et al.*, “Control of magnetite nanocrystal morphology in magnetotactic bacteria by regulation of *mms7* gene expression,” *Sci. Rep.*, vol. 6, no. 1, pp. 1–11, Jul. 2016.
- [30] T. C. Eisele and K. L. Gabby, “Review of reductive leaching of iron by anaerobic bacteria,” *Min. Proc. Ext. Met. Rev.*, vol. 35, no. 2, pp. 75–105, Jan. 2012.
- [31] Y. J. Tang *et al.*, “Evaluation of the effects of various culture conditions on Cr(VI) reduction by *Shewanella oneidensis* MR-1 in a novel high-throughput mini-bioreactor,” *Biotechnol. Bioeng.*, vol. 95, no. 1, pp. 176–184, Mar. 2006.
- [32] H. Friman *et al.*, “Effect of external voltage on *Pseudomonas putida* F1 in a bio electrochemical cell using toluene as sole carbon and energy source,” *Microbiology*, vol. 158, pp. 414–423, Jul. 2011.
- [33] T. Perez-Gonzalez *et al.*, “Magnetite biomineralization induced by *Shewanella oneidensis*,” *Geochim. Cosmochim. Acta*, vol. 74, no. 3, pp. 967–979, Oct. 2009.
- [34] T. C. Eisele and K. L. Gabby, “Review of reductive leaching of iron by anaerobic bacteria,” *Min. Proc. Ext. Met. Rev.*, vol. 35, no. 2, pp. 75–105, Jul. 2012.
- [35] C. Rao, A. Müller, and A. Cheetham, *The Chemistry of Nanomaterials: Synthesis, Properties and Applications in 2 Volumes*, vol. 1, Weinheim, Germany: Wiley-VCH, 2004.
- [36] S. Sze and K. Ng, *Physics of Semiconductor Devices*, 3rd ed., Hoboken, NJ, USA: John Wiley & Sons, 2006.
- [37] A. Sahu *et al.*, “Electronic impurity doping in CdSe nanocrystals,” *Nano Lett.*, vol. 12, no. 5, pp. 2587–2594, Apr. 2012.
- [38] N. T. T. Nguyen and S. D. Sarma, “Impurity effects on semiconductor quantum bits in coupled quantum dots,” *Phys. Rev. B*, vol. 83, no. 23, pp. 1–23, Jun. 2011.

- [39] W. E. Buhro and V. L. Colvin, "Semiconductor nanocrystals: Shape matters," *Nat. Mater.*, vol. 2, pp. 138-139, Mar. 2003.
- [40] I. R. Mcfarlane, J. R. Lazzari-Dean, and M. Y. El-Naggar, "Field effect transistors based on semiconductive microbially synthesized chalcogenide nanofibers," *Acta Biomater.*, vol. 13, pp. 364–373, Feb. 2015.
- [41] V. Amendola *et al.*, "Surface plasmon resonance in gold nanoparticles: A review," *J. Phys. Condens. Matter*, vol. 29, no. 20, pp. 1-48, Apr. 2017.
- [42] J. J. Mock *et al.*, "Shape effects in plasmon resonance of individual colloidal silver nanoparticles," *J. Chem. Phys.*, vol. 116, no. 15, pp. 6755–6759, Apr. 2002.
- [43] P. D. Cunningham *et al.*, "Assessment of anisotropic semiconductor nanorod and nanoplatelet heterostructures with polarized emission for liquid crystal display technology," *ACS Nano*, vol. 10, no. 6, pp. 5769–5781, May 2016.
- [44] A. B. Cunningham and J. E. Lennox, "Early views of the nature of biofilms," in *Biofilms: The Hypertextbook*, Bozeman, MT: Montana State University, 2011.
<https://www.cs.montana.edu/webworks/projects/stevesbook/contents/chapters/chapter001/section002/blue/page001.html>. (accessed Oct. 8, 2018).
- [45] "Biofilm basics: Section 4," *Montana State University Center for Biofilm Engineering*.
http://www.biofilm.montana.edu/biofilm-basics/key_characteristics_of_biofilms.html. (accessed November 14, 2018).
- [46] S. Shirodkar *et al.*, "The octahaem SirA catalyses dissimilatory sulfite reduction in *Shewanella oneidensis* MR-1," *Environ. Microbiol.*, vol. 13, no. 1, pp. 108–115, Jan. 2011.
- [47] O. Bretschger *et al.*, "Current production and metal oxide reduction by *Shewanella oneidensis* MR-1 wild type and mutants," *Appl. Environ. Microbiol.*, vol. 74, no. 2, pp. 553–553, Jul. 2007.
- [48] C. Rameteke, T. Chakrabarti, and R. Pandey, "Biological entities in stabilization of nanomaterials." AZOnano.com. <https://www.azonano.com/article.aspx?ArticleID=2546> (Accessed Feb. 27, 2019).
- [49] L. Wang *et al.*, "Biofabrication of morphology improved cadmium sulfide nanoparticles using *Shewanella oneidensis* bacterial cells and ionic liquid: For toxicity against brain cancer cell lines," *J. Photochem. Photobiol. B*, vol. 178, pp. 424–427, Jan. 2018.
- [50] W. Wang, I. Germanenko, and M. S. El-Shall, "Room-temperature synthesis and characterization of nanocrystalline CdS, ZnS, and Cd_xZn_{1-x}S," *Chem. Mater.*, vol. 14, no. 7, pp. 3028–3033, May 2002.

- [51] H.-J. Bai and Z.-M. Zhang, "Microbial synthesis of semiconductor lead sulfide nanoparticles using immobilized *Rhodobacter sphaeroides*," *Mater. Lett.*, vol. 63, no. 9-10, pp. 764–766, Apr. 2009.
- [52] S. Sadovnikov and A. Gusev, "Chemical deposition of nanocrystalline lead sulfide powders with controllable particle size," *J. Alloys Compnd.*, vol. 586, pp. 105–112, Feb. 2014.
- [53] I. R. Mcfarlane, J. R. Lazzari-Dean, and M. Y. El-Naggar, "Field effect transistors based on semiconductive microbially synthesized chalcogenide nanofibers," *Acta Biomater.*, vol. 13, pp. 364–373, Feb. 2015.
- [54] B. R. Johnson, M. J. Schweiger, and S. K. Sundaram, "Chalcogenide nanowires by evaporation-condensation," *J. Non-Cryst. Solids*, vol. 351.16, pp. 1410–1416, Feb. 2005.
- [55] H. Ayano *et al.*, "Isolation of a selenite-reducing and cadmium-resistant bacterium *Pseudomonas* sp. strain RB for microbial synthesis of CdSe nanoparticles," *Journal Biosci. Bioeng.*, vol. 117, no. 5, pp. 576–581, May 2014.
- [56] J. T. Siy, E. M. Brauser, and M. H. Bartl, "Low-temperature synthesis of CdSe nanocrystal quantum dots," *Chem. Commun.*, vol. 47, no. 1, pp. 364–366, Sep. 2010.
- [57] W. D. Burgos *et al.*, "Characterization of uraninite nanoparticles produced by *Shewanella oneidensis* MR-1," *Geochim. Cosmochim. Acta*, vol. 72, no. 20, pp. 4901–4915, Oct. 2008.
- [58] D. Hudry *et al.*, "Controlled synthesis of thorium and uranium oxide nanocrystals," *Chem.: Eur. J.*, vol. 19, no. 17, pp. 5297–5305, Apr. 2013.
- [59] K. Prasad and A. K. Jha, "ZnO Nanoparticles: Synthesis and adsorption study," *Nat. Sci.*, vol. 01, no. 02, pp. 129–135, Jul. 2009.
- [60] C. Li *et al.*, "Synthesis of zinc oxide nanocrystals by thermal decomposition of Zn-oleate in organic medium," *Sci. China Ser. E*, vol. 51, no. 12, pp. 2075–2079, Dec. 2008.
- [61] Y. V. Nanchariah and P. N. Lens, "Selenium biomineralization for biotechnological applications," *Trends Biotechnol.*, vol. 33, no. 6, pp. 323–330, Jun. 2015.
- [62] Y. Yuan *et al.*, "Electrocatalytic activity of anodic biofilm responses to pH changes in microbial fuel cells," *Bioresour. Technol.*, vol. 102, no. 13, pp. 6887–6891, Jul. 2011.
- [63] A. Kumlanghan *et al.*, "Microbial fuel cell-based biosensor for fast analysis of biodegradable organic matter," *Biosens. Bioelectron.*, vol. 22, no. 12, pp. 2939–2944, Jun. 2007.
- [64] A. Larrosa-Guerrero *et al.*, "Effect of temperature on the performance of microbial fuel cells," *Fuel*, vol. 89, no. 12, pp. 3985–3994, Dec. 2010.

- [65] S. N. Inamdar, P. P. Ingole, and S. K. Haram, “Determination of band structure parameters and the quasi-particle gap of CdSe quantum dots by cyclic voltammetry,” *ChemPhysChem*, vol. 9, no. 17, pp. 2574–2579, Nov. 2008.
- [66] J. Goldstein *et al.*, *Scanning Electron Microscopy and X-ray Microanalysis: A Text for Biologists, Materials Scientists, and Geologists*, 3rd ed., Berlin, Germany: Springer Science+Business Media, 2007.
- [67] B. Hafner, “Energy dispersive spectroscopy on the SEM: A primer,” *Characterization Facility, University of Minnesota—Twin Cities*.
http://www.charfac.umn.edu/instruments/eds_on_sem_primer.pdf. (Accessed Feb. 18, 2019).
- [68] D. B. Williams and C. B. Carter, *Transmission Electron Microscopy: A Textbook for Materials Science*, vol. 1, 2nd ed., Berlin, Germany: Springer Science+Business Media, 2009.
- [69] B. D. Cullity, S.R. Stock, *Elements of X-ray Diffraction*, 3rd ed., New York, NY, USA: Prentice-Hall, 2001.
- [70] N. Elgrishi *et al.*, “A practical beginner’s guide to cyclic voltammetry,” *J. Chem. Educ.*, vol. 95, no. 2, pp. 197-206, Nov. 2017.
- [71] A. Quiroga, “Cyclic voltammetry,” *LibreTexts*,
https://chem.libretexts.org/Core/Analytical_Chemistry/Instrumental_Analysis/Cyclic_Voltammetry (accessed Dec. 12, 2019).
- [72] “Analytical electrochemistry: The basic concepts,” *Analytical Sciences Digital Library*,
https://www.asdlib.org/onlineArticles/ecourseware/Kelly_Potentiometry/PDF-10-CV-ImpParam.pdf. (accessed Feb. 13, 2019).
- [73] J. Clark, “The Beer-Lambert law,” *Chemistry*,
[https://chem.libretexts.org/Bookshelves/Physical_and_Theoretical_Chemistry_Textbook_Maps/Supplemental_Modules_\(Physical_and_Theoretical_Chemistry\)/Spectroscopy/Electronic_Spectroscopy/Electronic_Spectroscopy_Basics/The_Beer-Lambert_Law](https://chem.libretexts.org/Bookshelves/Physical_and_Theoretical_Chemistry_Textbook_Maps/Supplemental_Modules_(Physical_and_Theoretical_Chemistry)/Spectroscopy/Electronic_Spectroscopy/Electronic_Spectroscopy_Basics/The_Beer-Lambert_Law). (accessed Mar. 13, 2019)
- [74] E. Smith and G. Dent, *Modern Raman Spectroscopy: A Practical Approach*, 2nd ed., Chichester, UK: Wiley, 2019.
- [75] S. Sahoo *et al.*, “Temperature-dependent Raman studies and thermal conductivity of few-layer MoS₂,” *J. Phys. Chem. C*, vol. 117, no. 17, pp. 9042–9047, Apr. 2013.
- [76] J. E. Spanier *et al.*, “Size-dependent properties of CeO₂ nanoparticles as studied by Raman scattering,” *Phys. Rev. B*, vol. 64, no. 24, pp. 1-8, Dec. 2001.
- [77] “Lead (II) sulfide (PbS) semiconductors,” *AZO Materials*,
<https://www.azom.com/article.aspx?ArticleID=8440>. (accessed Feb. 6, 2019)

- [78] I. Ravich, *Semiconducting Lead Chalcogenides*, vol. 5, New York, NY, USA: Springer Science & Business Media, 1970.
- [79] Y. Yang *et al.*, “Controlled ambipolar doping and gate voltage dependent carrier diffusion length in lead sulfide nanowires,” *Nano Lett.*, vol. 12, no. 11, pp. 5890–5896, Oct. 2012.
- [80] H. Lee *et al.*, “PbS and CdS quantum dot-sensitized solid-state solar cells: Old concepts, new results,” *Adv. Funct. Mater.*, vol. 19, no. 17, pp. 2735–2742, Sep. 2009.
- [81] M. Govarthanan *et al.*, “Significance of autochthonous *Bacillus* sp. KK1 on biomineralization of lead in mine tailings,” *Chemosphere*, vol. 90, no. 8, pp. 2267–2272, Feb. 2013.
- [82] W. Wang *et al.*, “A novel and simple one-step solid-state reaction for the synthesis of PbS nanoparticles in the presence of a suitable surfactant,” *Mater. Res. Bull.*, vol. 36, no. 11, pp. 1977–1984, Sep. 2001.
- [83] “Lead sulfide,” *ESPI Metals*, <http://www.espimetals.com/index.php/msds/208-Lead%20Sulfide>. (accessed Feb. 6, 2019).
- [84] “Lead in drinking water,” *Guidelines for Drinking-Water Quality*. Geneva: World Health Organization, 2006.
- [85] L. S. Chongad *et al.*, “Synthesis of lead sulfide nanoparticles by chemical precipitation method,” *J. Phys. Conf. Ser.*, vol. 755, pp. 1-4, 2016.
- [86] C. G. Ong, R. A. Dahlgren, and K. K. Tanji, “X-ray diffraction pattern reduction and computer-rendered line peak spectra for mineral analysis,” *Comput. Geosci.*, vol. 18, no. 5, pp. 517–529, Jun. 1992.
- [87] “Cadmium sulfide (CdS) semiconductors,” *AZO Materials*, <https://www.azom.com/article.aspx?ArticleID=8407>. (accessed Feb. 13, 2019)
- [88] M. Wright and A. Uddin, “Organic—inorganic hybrid solar cells: A comparative review,” *Sol. Energy Mater. Sol. Cells*, vol. 107, pp. 87–111, Dec. 2012.
- [89] C. Voss, S. Subramanian, and C.-H. Chang, “Cadmium sulfide thin-film transistors fabricated by low-temperature chemical-bath deposition,” *J. Appl. Phys.*, vol. 96, no. 10, pp. 5819–5823, Nov. 2004.
- [90] “Cadmium toxicity: Where is cadmium found?”, *Agency for Toxic Substances & Disease Registry*, <https://www.atsdr.cdc.gov/csem/csem.asp?csem=6&po=5>. (Accessed Feb. 27, 2019).

- [91] “Cadmium in drinking water,” *Guidelines for Drinking-Water Quality*. Geneva, Switzerland: World Health Organization, 2006.
- [92] L. Hong *et al.*, “Millifluidic synthesis of cadmium sulfide nanoparticles and their application in bioimaging,” *RSC Advances*, vol. 7, no. 62, pp. 36819–36832, Jul. 2017.
- [93] H. Bai *et al.*, “Biological synthesis of size-controlled cadmium sulfide nanoparticles using immobilized *Rhodobacter sphaeroides*,” *Nanoscale Res. Lett.*, vol. 4, no. 7, pp. 717–723, Apr. 2009.
- [94] M. Pattabi and J. Uchil, “Synthesis of cadmium sulphide nanoparticles,” *Sol. Energy Mater. Sol. Cells*, vol. 63, no. 4, pp. 309–314, Aug. 2000.
- [95] W. Winer, “Molybdenum disulfide as a lubricant: A review of the fundamental knowledge,” *Wear*, vol. 10, no. 6, pp. 422–452, Feb. 1967.
- [96] F. Wypych and R. Schöllhorn, “1T-MoS₂, a new metallic modification of molybdenum disulfide,” *J. Chem. Soc., Chem. Commun.*, no. 19, pp. 1386–1388, May 1992.
- [97] P. Fleischauer *et al.*, “Electronic structure and lubrication properties of MoS₂: A quantitative molecular orbital approach,” *Langmuir*, vol. 5, pp. 1009–1015, Jul. 1989.
- [98] Z. He and W. Que, “Molybdenum disulfide nanomaterials: Structures, properties, synthesis and recent progress on hydrogen evolution reaction,” *Appl. Mater. Today*, vol. 3, pp. 23–56, Jun. 2016.
- [99] D. Sarkar *et al.*, “MoS₂ field-effect transistor for next-generation label-free biosensors,” *ACS Nano*, vol. 8, no. 4, pp. 3992–4003, Mar. 2014.
- [100] J. Park *et al.*, “Comparison of hydrogen sulfide gas and sulfur powder for synthesis of molybdenum disulfide nanosheets,” *Curr. Appl. Phys.*, vol. 16, no. 7, pp. 691–695, Jul. 2016.
- [101] M. D. Tucker, L. L. Barton, and B. M. Thomson, “Reduction and immobilization of molybdenum by *Desulfovibrio desulfuricans*,” *J. Environ. Qual.*, vol. 26, no. 4, p. 1146–1152, Jul. 1997.
- [102] M. Y. Shukor and M. A. Syed, “Microbiological reduction of hexavalent molybdenum to molybdenum blue,” in *Current Research, Technology and Education Topics in Applied Microbiology and Microbial Biotechnology*, Badajoz, Spain: Formatex Research Center, 2010.
- [103] P. K. Panigrahi and A. Pathak, “Aqueous medium synthesis route for randomly stacked molybdenum disulfide,” *J. Nanoparticles*, vol. 2013, pp. 1–10, Apr. 2013.

- [104] R. K. Mishra *et al.*, “Binder-free, scalable hierarchical MoS₂ as electrode materials in symmetric supercapacitors for energy harvesting applications,” *Mater. Lett.*, vol. 236, pp. 167–170, Feb. 2019.
- [105] M. Manuja, V. S. Krishnan, and G. Jose, “Molybdenum disulphide nanoparticles synthesis using a low temperature hydrothermal method and characterization,” *IOP Conf. Ser. Mat. Sci. Eng.*, vol. 360, p. 1-5, Sep. 2018.
- [106] “Molybdenum disulfide MoS₂” *Nitronix Nanotechnology Corporation*. <http://www.nitronix.com/mos2-2/> (Accessed Mar. 26, 2019).
- [107] M. Y. Shukor *et al.*, “Hexavalent molybdenum reduction to molybdenum blue by *S. Marcescens* Strain Dr. Y6,” *Appl. Biochem. Biotechnol.*, vol. 149, no. 1, pp. 33–43, Feb. 2008.
- [108] S. Dhanekar and S. Jain, “Porous silicon biosensor: Current status,” *Biosens. Bioelectron.*, vol. 41, pp. 54–64, Mar. 2013.
- [109] D. R. Cooper *et al.*, “Experimental review of graphene,” *ISRN Condens. Matter Phys.*, vol. 2012, pp. 1–56, Nov. 2011.
- [110] T. Kuila *et al.*, “Chemical functionalization of graphene and its applications,” *Prog. Mater. Sci.*, vol. 57, no. 7, pp. 1061–1105, Sep. 2012.
- [111] Y. Shao *et al.*, “Graphene based electrochemical sensors and biosensors: A review,” *Electroanalysis*, vol. 22, no. 10, pp. 1027–1036, Dec. 2009.
- [112] Z. He *et al.*, “Architecture engineering of hierarchically porous chitosan/vacuum-stripped graphene scaffold as bioanode for high performance microbial fuel cell,” *Nano Lett.*, vol. 12, no. 9, pp. 4738–4741, Aug. 2012.
- [113] R. Mukherjee *et al.*, “Photothermally reduced graphene as high-power anodes for lithium-ion batteries,” *ACS Nano*, vol. 6, no. 9, pp. 7867–7878, Aug. 2012.
- [114] C.-W. Lee *et al.*, “Effect of nonsolvent on the formation of polymer nanomaterials in the nanopores of anodic aluminum oxide templates,” *Macromol. Rapid Commun.*, vol. 33, no. 16, pp. 1381–1387, May 2012.
- [115] A. K. Srivastava *et al.*, “Templated assembly of magnetic cobalt nanowire arrays,” *Metall. Mater. Trans. A*, vol. 38, no. 4, pp. 717–724, Apr. 2007.
- [116] T. Kondo *et al.*, “Circadian rhythms in prokaryotes: Luciferase as a reporter of circadian gene expression in cyanobacteria,” *Proc. Natl. Acad. Sci. U.S.A.*, vol. 90, no. 12, pp. 5672–5676, Jun. 1993.

- [117] A. A. Carmona-Martinez *et al.*, “Cyclic voltammetric analysis of the electron transfer of *Shewanella oneidensis* MR-1 and nanofilament and cytochrome knock-out mutants,” *Bioelectrochemistry*, vol. 81, no. 2, pp. 74–80, Jun. 2011.
- [118] F. Lisdat and D. Schäfer, “The use of electrochemical impedance spectroscopy for biosensing,” *SpringerLink*, Aug-2008. <https://link.springer.com/article/10.1007/s00216-008-1970-7>. (Accessed Oct. 18, 2018).

APPENDIX

A.1 Standard Medium for Cultivation of *S. oneidensis* MR-1

Chemical Description	Chemical Formula	Molar Mass	g/L	Conc. in Final Solution
PIPES Buffer	C ₈ H ₁₈ N ₂ O ₆ S ₂	302.36 g/mol	0.91	3 mM
Ammonium Chloride	NH ₄ Cl	53.49 g/mol	0.53 5	10 mM
Potassium Chloride	KCl	74.55 g/mol	0.1	1.34 mM
Monopotassium Phosphate	KH ₂ PO ₄	136.086 g/mol	0.6	4.4 mM
Potassium Sulfate	K ₂ SO ₄	174.259 g/mol	0.23 4	1.34 mM
Lactic Acid	CH ₃ CH(OH)C O ₂ H	90.09 g/mol	3.73	20 mM
Chemical Description	Recipe	Volume Added		
Mineral Solution, 100X	(see A.2)	10 mL		
Vitamin Solution, 100x	(see A.3)	10 mL		
Amino Acid Solution, 100x	(see A.4)	10 mL		

Set pH to 7.0 after all components have been added using NaOH or HCl.

A.2 Mineral Solution, 100x stock

Chemical Description	Chemical Formula	Molar Mass (g/mol)	g/L	Conc. in Final Solution
Nitriloacetic acid (a) (<i>dissolved with NaOH to pH 8</i>)	$\text{N}(\text{CH}_2\text{CO}_2\text{H})_3$	191.14	1.5	78.49 μM
Magnesium sulfate heptahydrate	$\text{MgSO}_4 \cdot 7\text{H}_2\text{O}$	246.48	3	121.71 μM
Manganese sulfate monohydrate	$\text{MnSO}_4 \cdot \text{H}_2\text{O}$	169.02	0.5	29.58 μM
Sodium Chloride	NaCl	58.443	1	171.12 μM
Ferrous Sulfate Heptahydrate	$\text{FeSO}_4 \cdot 7\text{H}_2\text{O}$	277.91	0.1	3.6 μM
Calcium Chloride Dihydrate	$\text{CaCl}_2 \cdot 2\text{H}_2\text{O}$	146.99	0.1	6.8 μM
Cobalt Chloride Hexahydrate	$\text{CoCl}_2 \cdot 6\text{H}_2\text{O}$	237.93	0.1	4.2 μM
Zinc Chloride	ZnCl_2	136.28	0.13	9.54 μM
Cupric Sulfate Pentahydrate	$\text{CuSO}_4 \cdot 5\text{H}_2\text{O}$	249.68	0.01	0.4 μM
Aluminum potassium disulfate dodecahydrate	$\text{KAl}(\text{SO}_4)_2 \cdot 12\text{H}_2\text{O}$	474.38	0.01	0.21 μM
Boric acid	BH_3O_3	61.83	0.01	1.62 μM
Sodium molybdate dihydrate	$\text{Na}_2\text{MoO}_4 \cdot 2\text{H}_2\text{O}$	241.95	0.02 5	1.03 μM
Nickel chloride hexahydrate	$\text{NiCl}_2 \cdot 6\text{H}_2\text{O}$	237.6	0.02 4	1.01 μM
Sodium tungstate	Na_2WO_4	329.86	0.02 5	0.76 μM

Set pH to 7.0 after all components have been added using NaOH or HCl.

A.3 Vitamin Solution, 100x stock

Chemical Description	Chemical Formula	Molar Mass (g/mol)	g/L	Conc. in Final Solution
D-biotin	C ₁₀ H ₁₆ N ₂ O ₃ S	244.3	0.002	81.87 nM
Folic acid	C ₁₉ H ₁₉ N ₇ O ₆	441.1	0.002	45.34 nM
Pyroxidine HCl	C ₈ H ₁₂ CINO ₃	205.6	0.01	486.38 nM
Riboflavin	C ₁₇ H ₂₀ N ₄ O ₆	376.4	0.005	132.84 nM
Thiamine HCl 1.0 H2O	C ₁₈ H ₁₈ Cl ₂ N ₄ OS	355.3	0.005	140.73 nM
Nicotinic Acid	C ₆ H ₅ NO ₂	123.1	0.005	406.17 nM
D-pantothenic acid hemicalcium salt	C ₉ H ₁₆ NO ₅ ·0.5Ca	238.3	0.005	209.82 nM
B12	C ₆₃ H ₈₈ CoN ₁₄ O ₁₄ P	1355.4	0.0001	0.74 nM
P-aminobenzoic acid	C ₇ H ₇ NO ₂	137.13	0.005	364.62 nM
Thioctic acid	C ₈ H ₁₄ O ₂ S ₂	206.3	0.005	242.37 nM

Set pH to 7.0 after all components have been added using NaOH or HCl.

A.4 Amino Acid Solution, 100x stock

Chemical Description	Chemical Formula	Molar Mass (g/mol)	g/L	Conc. in Final Solution
L-glutamic acid	C ₅ H ₉ O ₄ N	147.130	2	2 mg/mL
L-arginine	C ₆ H ₁₄ N ₄ O ₂	174.204	2	2 mg/mL
DL-Serine	C ₃ H ₇ NO ₃	105.093	2	2 mg/mL

Set pH to 7.0 after all components have been added using NaOH or HCl.